**University of Alberta**


**Library Release Form**



**Name of Author**: Henning Kuehl

**Title of Thesis**: Least-squares wave-equation migration/inversion

**Degree**: Doctor of Philosophy

**Year this Degree Granted**: 2002

Henning Kuehl
Hauptstrasse 29
31275 Lehrte
Germany


**Date**: _____

**University of Alberta**

LEAST-SQUARES WAVE-EQUATION MIGRATION/INVERSION

by

**Henning Kuehl**

A thesis submitted to the Faculty of Graduate Studies and Research in partial fulfillment
of the requirements for the degree of **Doctor of Philosophy**.

in

Geophysics

Department of Physics

Edmonton, Alberta
Fall 2002

**University of Alberta**

**Faculty of Graduate Studies and Research**

The undersigned certify that they have read, and recommend to the Faculty of Graduate Studies and Research for acceptance, a thesis entitled **Least-squares wave-equation migration/inversion** submitted by Henning Kuehl in partial fulfillment of the requirements for the degree of **Doctor of Philosophy** in *Geophysics*.

_____

Dr. M. D. Sacchi (Supervisor)

_____

Dr. L. Le

_____

Dr. M. Razavy

_____

Dr. D. R. Schmitt

_____

Dr. L. R. Lines (External Examiner)

_____

Dr. F. Marsiglio (Chair)

**Date**: _____

# Abstract

This thesis presents an acoustic migration/inversion algorithm that inverts seismic reflection data for the angle dependent subsurface reflectivity by means of least-squares minimization. The method is based on the primary seismic data representation (single scattering approximation) and utilizes one-way wavefield propagators ('wave-equation operators') to compute the Green's functions of the problem. The Green's functions link the measured reflection seismic data to the image points in the earth's interior where an angle dependent imaging condition probes the image point's angular spectrum in depth.

The proposed least-squares wave-equation migration minimizes a weighted seismic data misfit function complemented with a model space regularization term. The regularization penalizes discontinuities and rapid amplitude changes in the reflection angle dependent common image gathers - the model space of the inverse problem. 'Roughness' with respect to angle dependence is attributed to seismic data errors (e.g., incomplete and irregular wavefield sampling) which adversely affect the amplitude fidelity of the common image gathers. The least-squares algorithm fits the seismic data taking their variance into account, and, at the same time, imposes some degree of smoothness on the solution. The model space regularization increases amplitude robustness considerably. It mitigates kinematic imaging artifacts and noise while preserving the data consistent smooth angle dependence of the seismic amplitudes.

In least-squares migration the seismic modelling operator and the migration operator - the adjoint of modelling - are applied iteratively to minimize the regularized objective function. Whilst least-squares migration/inversion is computationally expensive synthetic data tests show that usually a few iterations suffice for its benefits to take effect. An example from the Gulf of Mexico illustrates the application of least-squares wave-equation migration/inversion to a real-world dataset. The efficient implementation of the algorithm is a challenge and had to be confined to two spatial dimensions (i.e., 2-D earth). Fortunately, distributed computing accelerates the computational turnaround of least-squares migration/inversion greatly. Therefore, given the rapidly evolving computer technology, it is conceivable that 3-D least-squares migration/inversion will become amenable to a practical implementation in the near future.

# Acknowledgements

First of all, I would like to thank my supervisor Dr. Mauricio Sacchi for his guidance and tremendous patience. Both his mentorship and friendship made my four years at the University of Alberta exciting and enjoyable.

I extend my gratitude to the members of my examining committee for their valuable suggestions and for agreeing to read my thesis.

Many fruitful discussions with my fellow students at the University of Alberta helped me a great deal during the course of my study. I would also like to acknowledge the staff of the Physics Department for doing a stupendous job.

I owe a debt to all of my friends for their kindness, support and encouragement. Special thanks go to Karsten Michael for many enjoyable hours of running and swimming.

I would specifically like to thank Lara for always being there and for putting up with me.

Finally, I would like to thank my family, especially my mother, for their support and patience and for always having confidence in me.

# Contents

# List of Figures

# List of Tables

# Introduction

Seismic imaging of geological subsurface structures and the inversion for seismic reflectivity are powerful tools for the detection, interpretation and the appraisal of hydrocarbon reservoirs. The seismic reflection method can be understood as a multi-source and multi-receiver scattering experiment. Seismic sources and receivers are placed at the earth's surface. The sources emit seismic energy into the subsurface at varying locations and the receivers record the earth's response as a function of time and position relative to the source. The goal of seismic imaging/inversion is to invert the recorded response (wavefield seismograms) for the subsurface properties. To this end a stepwise, linearized imaging/inversion strategy based on the primary (i.e., single scattering) wavefield representation has been adopted in this thesis. One distinguishes between imaging and inversion, although, this distinction is not sharply defined and quite often subject to debate (Wapenaar, 1996). Roughly, imaging aims at producing a map or an image of the position and distribution of the reflecting boundaries and objects by back-propagating the surface wavefield. In addition to that, inversion attempts to invert for the magnitude variations of the angle dependent subsurface reflectivity. The inverted reflectivity is related to the medium's detail structure and contains information about the local rock and pore-space properties. In exploration seismology, imaging is usually termed (depth or time) migration. Migration is less demanding than inversion in terms of wavefield amplitude preservation, the phase (i.e., travel-time) is the primary concern. In inversion one demands both correct phase and correct amplitude information. Hence, the proper dynamic treatment of the recorded wavefield becomes an issue. Since, in a practical sense, migration can be regarded as a less ambitious form of inversion, the umbrella term migration/inversion is frequently used to emphasize this close relationship.

The primary data representation invokes a number of simplifications to make the

1
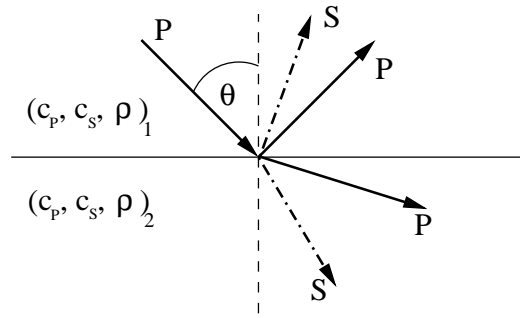
Figure 1: Seismic energy partitioning for a compressional wave (P wave) impinging on a plane interface in an elastic continuum at an angle $\theta$. Both reflected and transmitted compressional (P) and shear (S) waves result. The discontinuity separates regions of different compressional- and shear wave velocity and density, $c_p$, $c_s$ and $\rho$, respectively.

generally non-linear inverse problem tractable. The inversion is tackled by a stepwise, linearized approach and is based on certain assumptions regarding the physical processes responsible for the seismic data. Essentially, the inversion process consists of three stages: surface related pre-processing (e.g., surface related multiple suppression) , angle dependent reflectivity migration/inversion and target related post-processing (medium parameter inversion) (Berkhout and Wapenaar, 1990).

Most notably, the primary data representation handles only single scattering data. Multiply scattered data are treated as noise, and multiple suppression is a key ingredient in the first processing stage.

The second stage involves wavefield back-propagation and reflectivity estimation. A macro- or background velocity model for wavefield back-propagation is inferred from the travel-time related attributes of the surface wavefield with the help of velocity analysis or tomographic techniques. Based on the independently obtained macro-velocities the surface wavefield is back-propagated (migrated) into the subsurface where the reflection angle dependent target reflectivity is estimated. The procedural separation between the determination of the long wavelength properties (macro-velocities) and the estimation of the short wavelength attributes (reflectivity) is a typical characteristic of the stepwise, linearized inversion approach.

The third stage attempts to infer detailed medium parameter information from the inverted reflectivity. It is important to realize that, in exploration seismology, one deals

2

mostly with fairly regular interfaces that separate geological units of different physical properties. Hence, the scattering process is usually treated, somewhat undiscriminatingly, as specular reflection scattering. The earth is generally described as an elastic continuum with many discontinuous interfaces. Figure 1 illustrates elastic specular reflection and transmission scattering for the simple two layer case. In this situation, the well-known Zoeppritz equations (Aki and Richards, 1980) govern the wave energy partitioning at the interface as a function of medium parameters (i.e., compressional- and shear wave velocity and density), and angle of incidence. Elastic mode conversions between compressional (P) and shear (S) waves occur as the waves undergo scattering. Supposing migration/inversion can provide a reliable estimate of the angle dependent reflection coefficient (ideally, for all involved wavefield modes), Zoeppritz's equations allow then to invert for the medium parameters above and below the interface. This is not an easy task, since non-linearity, non-uniqueness etc. complicate the inverse problem. Finally, the inverted medium parameters can be interpreted in terms of rock and pore-space properties.

The outlined processing flow has many shortcomings that can hamper a successful and unambiguous inversion. For instance, the single scattering assumption means that wave modes are allowed to change their type only once during propagation. Transmission losses are neglected entirely. That is, single scattering also implies that the medium contrasts have to be somewhat weak. Furthermore, where the local interface curvature is significant compared to the dominant wavefield wavelength, the description of scattering in terms of a specular reflection process breaks down; a more general theory than Zoeppritz's equations that relates the scattering angle spectrum with the medium properties is then required. In practice, however, inversion based on the described strategy has oftentimes been successful within its limitations. Rather than an inversion for absolute values, seismic imaging/inversion is a science of anomalies (Castagna, 1993). The inversion for relative parameter variations and deviations from certain expected average values has proven to be a realistic goal. The detected anomalies hold many clues and are a valuable aid for the structural, stratigraphic and lithologic interpretation of the subsurface.

Figure 2 details the inversion process in a schematic flowchart (Berkhout and Wape-

```
┌─────────────────────────────────────────────┐
│        Multi–component seismic shot records  │
└─────────────────────────────────────────────┘
                      │
┌─────────────────────────────────────────────┐
│           Decomposition in P and S waves     │
└─────────────────────────────────────────────┘
                      │
┌─────────────────────────────────────────────┐
│              Surface multiple suppression    │
└─────────────────────────────────────────────┘
        │                            │
┌───────────────────────┐  ┌───────────────────────┐
│ Estimation of P macro │  │ Estimation of S macro │
│    velocity field     │  │    velocity field     │
└───────────────────────┘  └───────────────────────┘
        │                            │
┌───────────────────────┐  ┌───────────────────────┐
│ Migration/inversion   │  │ Migration/inversion   │
│    of PP response     │  │    of PS response     │
└───────────────────────┘  └───────────────────────┘
        │                            │
      ┌───────────────────────────────────┐
      │ Elastic inversion for P and S     │
      │       velocity and density        │
      └───────────────────────────────────┘
                      │
      ┌───────────────────────────────────┐
      │ Lithologic inversion for rock and │
      │          pore parameters          │
      └───────────────────────────────────┘
```
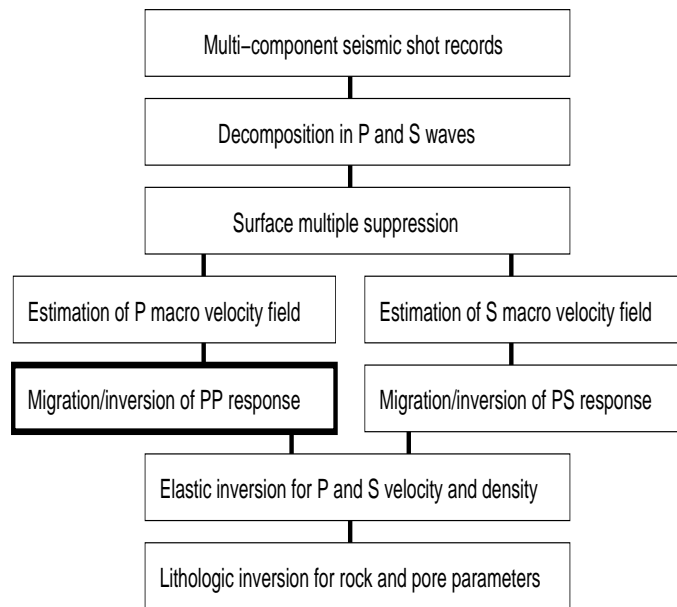
Figure 2: Flowchart illustrating linearized seismic inversion in steps (modified after Berkhout and Wapenaar (1990)). The highlighted sub-process, PP least-squares migration/inversion for reflectivity inversion, is the main topic of this thesis. Each box in this flowchart is a topic of ongoing research in its own right.

naar, 1990). The flowchart is specific for seismic data acquired on land. In the marine cases, where sources and receivers are separated from the elastic earth by a water layer, obvious modifications apply.

The main topic of the thesis is the highlighted box in Figure 2, the migration/inversion of compressional waves for angle dependent subsurface reflectivity (P to P reflections). More specifically, a novel least-squares wave-equation migration/inversion is introduced that yields regularized common image gathers (CIGs). The approach is novel in that it combines the concept of numerical least-squares optimization, wave-equation migration in complex media and angle dependent imaging. The least-squares migrated CIGs, the solution of the inversion, contain amplitude information closely related to the bandlimited reflectivity. They are of potentially higher quality and fidelity than conventionally obtained CIGs. Since only compressional waves are considered, the theory for migration/inversion is developed within the less involved acoustic approximation of continuum mechanics.

In migration/inversion one attempts to invert the seismic data by constructing an approximate inverse to the forward integral operator that relates the subsurface model perturbations (the reflectivity) to the observed seismograms (e.g., Clayton and Stolt (1981), Bleistein et al. (2001)). Under the single scattering approximation, the integral operator can be approximately inverted via a linear integral operator. This integral operator is composed of Green's functions that account for the wave propagation in the background medium (i.e., the macro-velocity field). Migration/inversion algorithms using ray-theoretical Green's functions are based on the solutions of the eikonal and transport equation, the high frequency approximation of the wave-equation. Alternatively, one-way wavefield propagators can be employed to calculate the Green's function of the problem (e.g., Gazdag and Sguazzero (1984), Stoffa et al. (1990) , Ristow and Rühl (1994)). These operators, frequently called wave-equation operators, have the advantage of inherently accounting for multi-pathing (Gray and May, 1994). Evidence is mounting that wavefield propagators perform significantly better than techniques based on the high frequency approximation.

One way to invert seismic data entails the approximate inversion of the forward modelling operator by analytical means. A second technique involves a numerical approach where the solution is retrieved by solving a linear discrete inverse problem. In that case, one seeks a model that fits the seismic (primary) data and, moreover, exhibits certain features and characteristics imposed by a model regularization. This approach to migration/inversion is called least-squares migration. Early developments of least-squares migration can be found in LeBras and Clayton (1988) and Lambaré et al. (1992). More recent papers by Nemeth et al. (1999) and Duquet et al. (2000) focus on the advantages of least-squares Kirchhoff migration/inversion (i.e., imaging based on ray theory) when uneven subsurface illumination and imaging artifacts due to irregularly and coarsely sampled seismic wavefields are the issue. Duquet et al. (2000) also demonstrate how to further improve the mitigation of sampling artifacts in common offset Kirchhoff migration by applying an smoothing constraint on the offset CIGs. As opposed to the course taken in this work, all of the cited least-squares migration algorithms are based on ray-theoretical Green's functions.

Kuehl and Sacchi (2001b) show that, in principle, the concept of least-squares migra-

tion can also be applied to split-step DSR (double-square-root) wavefield propagators (Claerbout, 1985; Popovici, 1996). With the introduction of a data covariance matrix (Tarantola, 1987) least-squares migration can account for missing data and unbalanced subsurface illumination due to variations in the common-midpoint (CMP) fold. Unfortunately, the standard recursive DSR implementation does not offer an efficient computation of offset CIGs as common offset Kirchhoff migration does. A non-recursive implementation of DSR migration, on the other hand, allows for the computation of separable offset DSR operators (Popovici, 1995; Kuehl and Sacchi, 2001a), but precludes the use of modifications, such as the split-step correction, that generalize the DSR operator for laterally varying media. That is to say, an alternative to common/separable offset wave-equation migration needs to be found for regularized least-squares wave-equation migration to be of practical use.

Recently, increasing attention has been given to wave-equation imaging principles that yield angle domain CIGs in complex media. These CIGs carry valuable angle dependent amplitude information (e.g., Stolt and Weglein (1985), de Bruin et al. (1990), Xu et al. (1998), Prucha et al. (1999), Wapenaar et al. (1999), Mosher and Foster (2000), Sava et al. (2001)). The employed ray parameter CIGs consist of a set of depth images as a function of offset ray parameter extracted from the back-propagated seismic wavefield. These CIGs are similar to migrated $\tau - p$ (i.e., slant stacked) midpoint-offset gathers (Ottolini and Claerbout, 1984; Mosher et al., 1996; Mosher et al., 1997). However, in generalized DSR migration combined with ray parameter domain imaging the order of slant stacking and wavefield propagation is reversed thereby relaxing the restriction to laterally invariant media. The midpoint-offset wavefield gathers are recursively back-propagated and the wavefield is decomposed at each depth level. Lastly, the wave-equation imaging condition (evaluation of the propagated wavefield at time zero) is applied to the slant stacked local wavefield. The amplitude variations with ray parameter (AVP) are closely related to the amplitude variations with angle (AVA) of the bandlimited reflectivity. Knowing the dip directions and the dip angles of the (locally) plane reflectors the CIGs can be converted to AVA plots.

In order to cast generalized DSR migration for AVP/AVA inversion into the least-squares framework, one needs to define a modelling/migration adjoint operator pair.

The migration and modelling operators are then iteratively applied to minimize the weighted least-squares data misfit using a conjugate gradient (CG) optimization algorithm. The proposed least-squares DSR migration is constrained with a ray parameter dependent smoothing regularization that increases the robustness of the inversion (Kuehl and Sacchi, 2002). The constraint penalizes discontinuities and rapid amplitude changes that most likely stem from numerical imaging artifacts and acquisition footprint, not AVA effects.

The thesis is organized as follows: Chapter 1 discusses the forward seismic modelling problem in great detail. In the second chapter, inversion concepts based on the previously outlined primary data representation are devised. As already mentioned, there exist essentially two avenues that can be followed to achieve this: by approximations to the inverse problem solution, or by numerical optimization schemes, both of which are conveniently derived within the framework of least-squares optimization. The third chapter exemplifies and tests the theory derived in the previous chapters with numerous synthetic data examples ranging from simple to complex. In Chapter 4 least-squares migration for AVP/AVA is applied to a real-world marine dataset from the Gulf of Mexico. Real data issues like macro-velocity model building and multiple suppression are addressed. The last chapter digresses briefly into computational issues of (least-squares) migration. Efficiency considerations are an integral part of any discussion on seismic inversion, since a fast computational turnaround is imperative. Chapter 5 introduces the real-valued Hartley transform as an alternative to the complex-valued Fourier transform to optimize the modelling and migration operators (Kuehl and Sacchi, 1999; Kuehl et al., 2001). That chapter also touches on the topic of distributed computing. Finally, a concluding discussion summarizes the main points of the thesis and attempts to shed some light on the road ahead.

# Chapter 1

# Seismic data modelling

The first step to the formulation of any inverse problem is the forward or modelling problem. It is emphasized what may be obvious: If a forward/modelling operator fails to describe the relevant physics of a process one is seeking to invert, the inverse operator will give erroneous results. Any mathematical operator, of necessity, becomes an idealization of the true nature of physics, capturing some features and excluding others. However, if care is taken that the physics of a sub-process is sufficiently honoured, a successful inversion for the parameters influencing this process is oftentimes possible.

This thesis is concerned with the imaging/inversion of the earth's subsurface properties using reflected seismic waves. Seismic imaging/inversion has two goals. First, the seismic surface data are back-propagated (inversely extrapolated) into the earth to image and position geological structures ('depth migration'). Second, if care is taken that amplitude effects are accounted for during back-propagation ('true-amplitude migration') the data can be locally inverted for the amplitude variation with angle of the reflection coefficients. The second goal is more demanding but, if successful, allows for the inversion of physical parameters defining the geological units separated by the reflecting interfaces.

The inverse problem becomes tractable by simplifying the forward modelling relationship. More precisely, the employed imaging/inversion techniques are based on a linearized, acoustic primary representation of the seismic surface data. Such techniques do not account for multiply reflected waves (multiple scattering). This imposes a smallness constraint on the coefficients defining the reflecting boundaries. Where significant multiple seismic energy is present in the data, multiple suppression techniques prior to imag-

ing/inversion have to be applied. In any case, the 'robustness' of the imaging/inversion algorithms with respect to all simplifications needs to be assessed carefully. It therefore is important to discuss the seismic data modelling operators in some detail.

Besides the limitations mentioned above, the simplified seismic data representation has other shortcomings (Gray, 1997). First, the modelling operators are derived for a fluid-like medium. In reality, seismic waves propagate in an elastic earth. That is, longitudinal (compressional) and transversal (shear) waves exist and mode conversion occur at interfaces. In spite of the restriction to compressional waves, seismic imaging based on the acoustic wave-equation has in many cases been successful. This is explained by the fact that seismic sources generate mostly compressional waves. Furthermore, most seismic surveys record only the pressure or the vertical particle velocity component and thus register predominantly compressional waves. The latter statement implies that the seismic waves travel in a near vertical direction at the receiver location. The normally low near surface velocities help for this assumption to be fulfilled. When elastic wave propagation effects are significant the formalism needs to be extended to elastic media (e.g., Wapenaar et al. (1987)). This extension is based on the premise that the recorded seismic data can be decomposed into compressional and shear wave responses before applying the imaging/inversion operators (Wapenaar et al., 1990). Second, the described method ignores anisotropy, which is known to affect seismic waves dynamically and kinematically (Vestrum et al., 1999). While it is possible to generalize the described operators to accommodate the kinematic effects of anisotropy (Kitchenside, 1991; Le Rousseau, 1997) such an extension is beyond the scope of this thesis. Third, the operators fail to correct for wavefield attenuation. Attenuation through lossy material can be modelled by an exponential loss of amplitude along the propagation path (viscoelastic media). However, it is difficult to estimate the amount of loss to be corrected. Fourth, the effects of fine structure in the medium properties on wavefield propagation are neglected owing to an implicit smoothness assumption underlying the derivation of the propagators.

Based on all of the above, Gray (1997) asserts that one can raise valid objections against the entire subject of 'true-amplitude' seismic imaging/inversion. Claerbout (1992) summarizes the same scepticism, stating "The phrase 'true-amplitude migration' has questionable meaning". However, seismic imaging has proven many times to be a ro-

bust tool for structural imaging of subsurface properties. To an extent this is also true for the inversion for amplitude information, since, according to Gray (1997), 'true-amplitude migration' for AVA inversion can be seen as a more rigorous, wave-equation based extension of amplitude variation with offset (AVO) analysis. It is widely accepted that AVO analysis has contributed to exploration success in the past (Gray, 1997). Despite this economical success, the ability of the employed operators to produce AVA information must be considered a bonus to the more robust structural imaging capabilities. The correct treatment of angle dependent amplitudes is bound to fail if one or more of the assumptions implicit in the above simplifications is severely violated.

## 1.1 Basic equations

The basic equations for wave propagation in continuous media are briefly reviewed for the sake of completeness (e.g., Wapenaar and Berkhout (1989)).

### 1.1.1 Equation of motion and constitutive relation

For lossless, inhomogeneous solids the linearized equation of motion (Newton's law) in cartesian coordinates reads:

$$\rho\frac{\partial^2 u_i}{\partial t^2} = \sum_{j=1}^{3} \frac{\partial \tau_{ij}}{\partial x_j}, \qquad (1.1.1)$$

where $x_{j=1,2,3}$ stand for $x,y$ and $z$, respectively, and $i = 1, 2, 3$. The vector $\mathbf{u}$ is the particle displacement as a function of the vector $\mathbf{x} = (x, y, z)$ and time $t$. Furthermore, $\tau_{ij}$ represents the nine components of the symmetric stress tensor, also as a function of space and time. The scalar $\rho = \rho(\mathbf{x})$ is the space dependent mass density in the equilibrium state. For an isotropic material the linearized stress-displacement equation (Hooke's law) is:

$$\tau_{ij} = \tau_{ji} = \lambda\delta_{ij}\nabla \cdot \mathbf{u} + \mu\left(\frac{\partial u_i}{\partial x_j} + \frac{\partial u_j}{\partial x_i}\right) = \lambda\delta_{ij}\nabla \cdot \mathbf{u} + 2\mu\epsilon_{ij}, \qquad (1.1.2)$$

where $\delta_{ij}$ is the Kronecker delta and $\lambda = \lambda(\mathbf{x})$ and $\mu = \mu(\mathbf{x})$ are the space dependent Lamé parameters. The $\epsilon_{ij}$ are the nine components of the symmetric strain tensor. Lamé's parameters are related to the bulk compression modulus $K = K(\mathbf{x})$ and the shear modulus $G = G(\mathbf{x})$ by $K = \lambda + \frac{2}{3}\mu$ and $G = \mu$, respectively. The bulk modulus of incompressibility describes the material resistance to a change in volume when subject to a load. It is

| Material | K (GPa) | G (GPa) | $\nu$ | $\rho(\text{g/cm}^3)$ |
|----------|---------|---------|-------|------------------------|
| Water | 2.1 | 0 | 0.5 | 1.0 |
| Sandstone | 17 | 6 | 0.34 | 1.9 |
| Olivine | 129 | 82 | 0.24 | 3.2 |

Table 1.1: Elastic parameters for some common earth materials (after Lay and Wallace (1995)).

defined by the ratio of an applied hydrostatic pressure to the induced fractional change in volume. The shear modulus, or rigidity is a measure of a material's resistance to shear stress. Yet another frequently used modulus is Poisson's ratio $\nu$. It describes the ratio of radial to axial strain when a uniaxial stress is applied (e.g., $\tau_{11} \neq 0, \tau_{22} = \tau_{33} = 0$). Poisson's ratio's relation to Lamé's parameters is:

$$\nu = \frac{-\epsilon_{22}}{\epsilon_{11}} = \frac{\lambda}{2(\lambda + \mu)}. \tag{1.1.3}$$

The maximum value is $\nu = 0.5$. This is true for a fluid, when $\mu = 0$. Most earth materials have a Poisson ratio between 0.22 and 0.35 (Lay and Wallace, 1995). Table 1.1 lists typical values of the bulk modulus, the shear modulus, Poisson's ratio and density for a few common earth materials.

### 1.1.2 Acoustic approximation

The equations (1.1.1) and (1.1.2) are simplified for fluid-like media. The off-diagonal stress tensor components $\tau_{ij}$, where $i \neq j$ (shear stresses), are zero; hence, $K = \lambda$ and $G = \mu = 0$. Pressure is defined by $p_{ii} = -\tau_{ii}$ and can be written as $p = p_{11} = p_{22} = p_{33}$ according to Pascal's law. The equation of motion (1.1.1) simplifies to:

$$\rho \frac{\partial^2 \mathbf{u}}{\partial t^2} = -\nabla p, \tag{1.1.4}$$

and the stress-displacement equation (1.1.2) becomes:

$$p = -K \nabla \cdot \mathbf{u}. \tag{1.1.5}$$

Next, source terms are added to the equations (1.1.4) and (1.1.5):

$$\rho \frac{\partial^2 \mathbf{u}}{\partial t^2} + \nabla p = \mathbf{f}, \tag{1.1.6}$$

and

$$\frac{1}{K}p + \nabla \cdot \mathbf{u} = i_v, \tag{1.1.7}$$

where $\mathbf{f}$ is the body force density and $i_v$ represents a volume density of volume injection (for example an airgun). Notice that equation (1.1.7) is the equation of continuity. The equations (1.1.6) and (1.1.7) are combined to the second order variable-density wave-equation for the pressure $p$:

$$\rho\nabla \cdot \frac{1}{\rho}\nabla p - \frac{\rho}{K}\frac{\partial^2 p}{\partial t^2} = \rho\nabla \cdot \frac{1}{\rho}\mathbf{f} - \rho\frac{\partial^2 i_v}{\partial t^2}. \tag{1.1.8}$$

The phase velocity is defined by:

$$c^2 = c^2(\mathbf{x}) = \frac{K(\mathbf{x})}{\rho(\mathbf{x})}. \tag{1.1.9}$$

As it stands, equation (1.1.8) describes the wave motion for compressional waves in an arbitrary fluid-like medium.

## 1.2 Forward wavefield extrapolation

The well developed theory of wavefield propagation (e.g., Aki and Richards (1980), Wapenaar et al. (1987)) that aims to solve the coupled system (1.1.6) and (1.1.7) constitutes an ideal framework for the derivation and understanding of seismic primary data imaging/inversion techniques.

### 1.2.1 Two-way wavefield representation

In surface seismic applications, the depth dimension is the wave propagation direction of preference. The axes perpendicular to the direction of preference are referred to as lateral coordinates. Consider a subsurface model that is subdivided into many thin slabs of thickness $dz \equiv \Delta z = z_i - z_{i-1}$ (Figure 1.1), where either symbol, $dz$ or $\Delta z$, will be used depending on whether a discrete or continuous notation is more convenient. It is stressed that the computational slab boundaries do not necessarily coincide with physical/geological layer boundaries. The layered model is understood as a computational grid, and the medium parameters $K$ and $\rho$ are allowed to vary smoothly in the lateral direction within each finite slab. The goal is to recursively extrapolate/propagate the
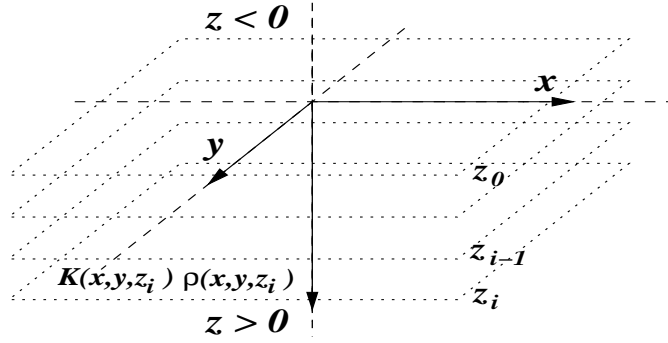
Figure 1.1: The coordinate system for seismic wave propagation. The $z$ axis is the direction of preference in seismic applications where sources and receivers are placed at the surface. The plane at $z_0 = 0$ serves as a reference datum and does not necessarily coincide with the actual surface. The medium parameters are allowed to vary vertically and laterally. For computational purposes the depth axis is discretized into thin slabs of thickness $\Delta z = z_i - z_{i-1}$. The parameter variations have compact support confined to the half-space $z > 0$.

wavefield from one depth level to the other. To this end the coupled equations (1.1.4) and (1.1.5) are expressed in the temporal frequency domain:

$$-i\omega\rho\mathbf{V} + \nabla P = \mathbf{F}, \tag{1.2.1}$$

and

$$\frac{-i\omega}{K}P + \nabla \cdot \mathbf{V} = -i\omega I_v, \tag{1.2.2}$$

where $\mathbf{V} = (V_x, V_y, V_z)^T$ and $\mathbf{F} = (F_x, F_y, F_z)^T$ are the monochromatic particle velocity and body force density vectors, respectively, and $P$ are $I_v$ are the monochromatic pressure and volume injection density, respectively. The time dependence is given by $e^{i\omega t}$ where $\omega$ is the angular frequency. The normal particle velocity and the pressure are continuous across interfaces separating regions of different medium properties (Wapenaar, 1998). Hence, it is useful to write the equations (1.2.1) and (1.2.2) in terms of the vertical velocity $V_z$ and pressure $P$. The $z$ derivatives are isolated from the lateral derivatives and $V_x$ and $V_y$ are eliminated from the equations (1.2.1) and (1.2.2):

$$\frac{\partial P}{\partial z} = -i\omega\rho V_z + F_z, \tag{1.2.3}$$

and

$$\frac{\partial V_z}{\partial z} = \frac{-i\omega}{K}P + \frac{\partial}{\partial x}\left(\frac{1}{i\omega\rho}\frac{\partial P}{\partial x}\right) + \frac{\partial}{\partial y}\left(\frac{1}{i\omega\rho}\frac{\partial P}{\partial y}\right)$$
$$+ i\omega I_v - \frac{\partial}{\partial x}\left(\frac{F_x}{i\omega\rho}\right) - \frac{\partial}{\partial y}\left(\frac{F_y}{i\omega\rho}\right). \tag{1.2.4}$$

The notation is simplified with the assignment of the operator $\mathcal{H}_2$:

$$\mathcal{H}_2 = \left(\frac{\omega}{c}\right)^2 + \rho\frac{\partial}{\partial x}\left(\frac{1}{\rho}\frac{\partial}{\partial x}\right) + \rho\frac{\partial}{\partial y}\left(\frac{1}{\rho}\frac{\partial}{\partial y}\right), \tag{1.2.5}$$

the wave vector:

$$\mathbf{Q} = (P, V_z)^T, \tag{1.2.6}$$

and the source vector:

$$\mathbf{D} = \left(F_z, i\omega I_v - \frac{\partial}{\partial x}\left(\frac{F_x}{i\omega\rho}\right) - \frac{\partial}{\partial y}\left(\frac{F_y}{i\omega\rho}\right)\right)^T. \tag{1.2.7}$$

The equations (1.2.3) and (1.2.4) read in matrix notation:

$$\frac{\partial \mathbf{Q}}{\partial z} = \underset{\sim}{\mathbf{A}}\,\mathbf{Q} + \mathbf{D}, \tag{1.2.8}$$

with

$$\underset{\sim}{\mathbf{A}} = \begin{pmatrix} 0 & -i\omega\rho \\ \frac{1}{i\omega\rho}\mathcal{H}_2 & 0 \end{pmatrix}. \tag{1.2.9}$$

The equation (1.2.8) is the two-way representation of wavefield propagation. The term two-way representation is due to the property of equation (1.2.8) to inherently account for downgoing and upgoing waves. Alternatively, in the next section the one-way representation is treated that explicitly distinguishes between the downgoing and upgoing wavefield states. The solution to the source free part of (1.2.8), in recursive propagator notation, is:

$$\mathbf{Q}(z_i) = \underset{\sim}{\mathbf{Y}}(z_i, z_{i-1})\mathbf{Q}(z_{i-1}), \tag{1.2.10}$$

with

$$\underset{\sim}{\mathbf{Y}}(z_i, z_{i-1}) = \exp\{\underset{\sim}{\mathbf{A}}_i(z_i - z_{i-1})\}, \tag{1.2.11}$$

or:

$$\begin{aligned}\mathbf{Q}(z) &= \exp\{\underset{\sim}{\mathbf{A}}_i(z - z_{i-1})\}\prod_{j=1}^{i-1}\exp\{\underset{\sim}{\mathbf{A}}_j(z_j - z_{j-1})\}\mathbf{Q}(z_0) \\ &= \underset{\sim}{\mathbf{Y}}(z, z_0)\mathbf{Q}(z_0),\end{aligned} \tag{1.2.12}$$

where $\exp\{\cdot\}$ is understood as a series expansion (Ursin, 1983). Moreover, the propagator satisfies the initial condition:

$$\underline{\mathbf{Y}}(z_0, z_0) = \underline{\mathbf{I}}. \tag{1.2.13}$$

The product representation in equation (1.2.12) is ordered in depth. The solution including the source term reads (Aki and Richards, 1980):

$$\mathbf{Q}(z) = \underline{\mathbf{Y}}(z, z_0)\mathbf{Q}(z_0) + \int_{z_0}^{z} \underline{\mathbf{Y}}(z, z')\mathbf{D}(z')dz'. \tag{1.2.14}$$

It is understood that the symbolic propagators depend implicitly on the lateral coordinates and derivatives. Wapenaar et al. (1987) discuss the numerical implementation of the above equations for the case of laterally varying media. Their numerical examples underline the validity of the solution in horizontally layered media with smoothly varying velocities and densities in the lateral direction. Theoretically, one could use the two-way representation for both modelling and imaging. For imaging, this representation is less useful, since imaging algorithms are usually based on the primary data representation. That is, multiply reflected wavefield energy is not considered. In order to correctly back-propagate (inverse extrapolate) multiple reflection data, a detailed prior knowledge of the subsurface velocity field is necessary. This prior knowledge is generally not available. In fact, having this information would make imaging/inversion essentially unnecessary. Hence, more robust - but also less accurate - one-way propagators that do not generate reflected waves are utilized in most imaging/inversion applications. This reasoning reflects the ubiquitous dilemma of seismic imaging/inversion. For completeness, it is mentioned that Kosloff and Baysal (1983) and Baysal et al. (1984) point out properties of the two-way representation that are interesting for imaging/inversion. By suppressing reflected energy in the two-way representation these properties may be exploited resulting in algorithms that are valid in smoothly varying media (in all directions) and which are accurate up to high tilt angles of propagation.

### 1.2.2 One-way wavefield representation

The purpose of the one-way wavefield representation is to decompose the total acoustic wavefield described by the equations (1.1.4) and (1.1.5) into two separate components, one for downgoing waves and one for upgoing waves (Claerbout, 1971). Where there are

medium parameter changes, one wave type scatters into the other. This decomposition allows for the interpretation of the evolving wavefield in terms of propagation (phase-shift) and scattering (interaction between the downgoing and upgoing states). To this end the square-root operator $\mathcal{H}_1$ is formally defined by:

$$\mathcal{H}_1 = \sqrt{\left(\frac{\omega}{c}\right)^2 + \frac{\partial^2}{\partial x^2} + \frac{\partial^2}{\partial y^2}} = \sqrt{\left(\frac{\omega}{c}\right)^2 + \nabla_l^2}, \qquad (1.2.15)$$

such that

$$\mathcal{H}_1 \mathcal{H}_1 = \mathcal{H}_2. \qquad (1.2.16)$$

That is, lateral derivatives of the density field and the commutator $[(\omega/c)^2, \nabla_l^2]$ are assumed to be negligible. Neglecting the lateral density variations gives $\mathcal{H}_2$ the form of the Helmholtz operator. [1] The two-way operator $\underset{\sim}{\mathbf{A}}$ is decomposed according to $\underset{\sim}{\mathbf{A}} = \underset{\sim}{\mathbf{L}} \underset{\sim}{\mathbf{\Lambda}} \underset{\sim}{\mathbf{L}}^{-1}$ (Wapenaar, 1998), with

$$\underset{\sim}{\mathbf{L}} = \frac{1}{\sqrt{2}} \begin{pmatrix} (\omega\rho)^{\frac{1}{2}} \mathcal{H}_1^{-\frac{1}{2}} & (\omega\rho)^{\frac{1}{2}} \mathcal{H}_1^{-\frac{1}{2}} \\ (\omega\rho)^{-\frac{1}{2}} \mathcal{H}_1^{\frac{1}{2}} & -(\omega\rho)^{-\frac{1}{2}} \mathcal{H}_1^{\frac{1}{2}} \end{pmatrix} = \frac{1}{\sqrt{2}} \begin{pmatrix} \mathcal{L}_1 & \mathcal{L}_1 \\ \mathcal{L}_2 & -\mathcal{L}_2 \end{pmatrix}, \qquad (1.2.17)$$

$$\underset{\sim}{\mathbf{\Lambda}} = \begin{pmatrix} -i\mathcal{H}_1 & 0 \\ 0 & i\mathcal{H}_1 \end{pmatrix}, \qquad (1.2.18)$$

and

$$\underset{\sim}{\mathbf{L}}^{-1} = \frac{1}{\sqrt{2}} \begin{pmatrix} \mathcal{H}_1^{\frac{1}{2}}(\omega\rho)^{-\frac{1}{2}} & \mathcal{H}_1^{-\frac{1}{2}}(\omega\rho)^{\frac{1}{2}} \\ \mathcal{H}_1^{\frac{1}{2}}(\omega\rho)^{-\frac{1}{2}} & -\mathcal{H}_1^{-\frac{1}{2}}(\omega\rho)^{\frac{1}{2}} \end{pmatrix} = \frac{1}{\sqrt{2}} \begin{pmatrix} \mathcal{L}_1^{-1} & \mathcal{L}_2^{-1} \\ \mathcal{L}_1^{-1} & -\mathcal{L}_2^{-1} \end{pmatrix}. \qquad (1.2.19)$$

The diagonal elements in $\underset{\sim}{\mathbf{\Lambda}}$ are the eigenvalues of $\underset{\sim}{\mathbf{A}}$ and the columns of $\underset{\sim}{\mathbf{L}}$ are the corresponding eigenvectors. The columns of the composition matrix $\underset{\sim}{\mathbf{L}}$ are normalized with respect to the vertical energy flux (Wapenaar, 1998). The operator $\underset{\sim}{\mathbf{L}}^{-1}$ decomposes the wave vector $\mathbf{Q}$ into downgoing and upgoing wavefield components or states $P^+$ and $P^-$, respectively. In the same way the source vector $\mathbf{D}$ is transformed into the one way representation of the source distributions $S^+$ and $S^-$. In matrix notation, composition and decomposition are:

$$\mathbf{Q} = \underset{\sim}{\mathbf{L}} \mathbf{P}, \qquad \mathbf{D} = \underset{\sim}{\mathbf{L}} \mathbf{S}, \qquad (1.2.20)$$

---

[1]Wapenaar and Grimbergen (1996) define a modified velocity $c'$, such that $\left(\frac{\omega}{c'}\right)^2 = \left(\frac{\omega}{c}\right)^2 - \frac{3\nabla_l\rho \cdot \nabla_l\rho}{4\rho^2} + \frac{\nabla_l^2\rho}{2\rho}$. This definition retains the form of $\mathcal{H}_2$ as a Helmholtz operator and thus allows for the incorporation of lateral density variations in one-way propagation. This possibility has not been considered here because reliable density information is generally not available in exploration seismic. More importantly, the transmitted wavefield, the modelled wavefield component in one-way modelling/imaging, is relatively insensitive to the density variations (Wu, 1996).

and

$$\mathbf{P} = \underset{\sim}{\mathbf{L}}^{-1}\mathbf{Q}, \qquad \mathbf{S} = \underset{\sim}{\mathbf{L}}^{-1}\mathbf{D}, \tag{1.2.21}$$

where $\mathbf{P} = (P^+, P^-)^T$ and $\mathbf{S} = (S^+, S^-)^T$. Upon inserting (1.2.20) into (1.2.8) the differential equation for $\mathbf{P}$ follows:

$$\frac{\partial \mathbf{P}}{\partial z} = \underset{\sim}{\mathbf{B}}\mathbf{P} + \mathbf{S}, \tag{1.2.22}$$

where

$$\underset{\sim}{\mathbf{B}} = \underset{\sim}{\mathbf{\Lambda}} - \underset{\sim}{\mathbf{L}}^{-1}\frac{\partial \underset{\sim}{\mathbf{L}}}{\partial z} = \underset{\sim}{\mathbf{\Lambda}} + \underset{\sim}{\mathbf{\Theta}}. \tag{1.2.23}$$

Componentwise, this reads:

$$\frac{\partial}{\partial z}\begin{pmatrix} P^+ \\ P^- \end{pmatrix} = \left[\begin{pmatrix} -i\mathcal{H}_1 & 0 \\ 0 & +i\mathcal{H}_1 \end{pmatrix} + \begin{pmatrix} \mathcal{T}^+ & \mathcal{R}^- \\ \mathcal{R}^+ & \mathcal{T}^- \end{pmatrix}\right]\begin{pmatrix} P^+ \\ P^- \end{pmatrix} + \begin{pmatrix} S^+ \\ S^- \end{pmatrix}, \tag{1.2.24}$$

where

$$\mathcal{T}^+ = \mathcal{T}^- = -\frac{1}{2}\left(\mathcal{L}_1^{-1}\partial_z\mathcal{L}_1 + \mathcal{L}_2^{-1}\partial_z\mathcal{L}_2\right), \tag{1.2.25}$$

and

$$\mathcal{R}^+ = \mathcal{R}^- = -\frac{1}{2}\left(\mathcal{L}_1^{-1}\partial_z\mathcal{L}_1 - \mathcal{L}_2^{-1}\partial_z\mathcal{L}_2\right). \tag{1.2.26}$$

The first matrix on the right hand side of the equation (1.2.24) is the propagation matrix. The second matrix is responsible for the interactions between the downgoing and upgoing wavefield states (scattering). According to the structure of equation (1.2.24) the scattering matrix is comprised of forward (transmission) scattering operators along the diagonal and backward (reflection) scattering operators along the anti-diagonal.

For completeness, the relation between the one-way and the two-way representation in terms of two-way propagation is briefly discussed. Using the eigenvalue decomposition the propagator for the two-way representation in equation (1.2.10) is replaced by three sub-processes (Wapenaar et al., 1987):

$$\underset{\sim}{\mathbf{Y}}(z_i, z_{i-1}) = \underset{\sim}{\mathbf{L}}(z_i)\underset{\sim}{\mathbf{W}}(z_i, z_{i-1})\underset{\sim}{\mathbf{L}}^{-1}(z_{i-1}), \tag{1.2.27}$$

with

$$\underset{\sim}{\mathbf{W}}(z_i, z_{i-1}) = \exp\{\underset{\sim}{\mathbf{\Lambda}}_i(z_i - z_{i-1})\}. \tag{1.2.28}$$

A flowchart in Figure 1.2 illustrates the relation between the two representations. While both approaches are mathematically equivalent, the two-way representation in equation
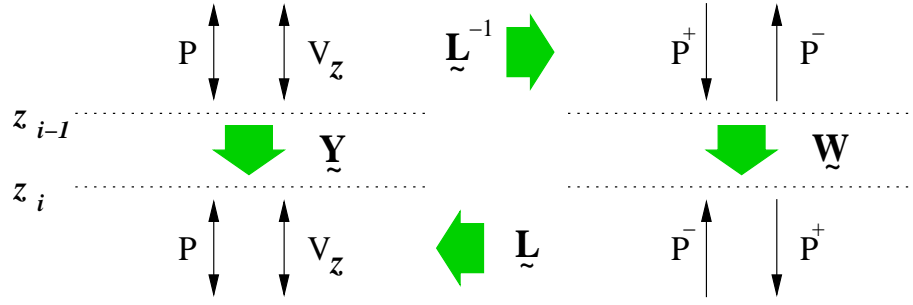
Figure 1.2: Flowchart demonstrating the relation between the two-way and the one-way representation of wavefield propagation (after Wapenaar et al. (1987)).

(1.2.10) is numerically advantageous if wavefield extrapolation based on two-way propagation is to be carried out (Wapenaar et al., 1987).

In the next section the (flux-normalized) one-way wavefield representation serves to formulate propagators that exclusively operate on either downgoing or upgoing waves. This restriction allows for the formulation of one-way propagators for imaging/inversion that do not produce reflected energy.

### 1.2.3 Recursive one-way wavefield propagator

One-way extrapolation operators provide an economical method for modelling certain types of wave motion. The basic restriction is that only the transmitted wavefield component is modelled. The ultimate goal of imaging/inversion is to image the scattering operator that gives rise to the recorded (primary) reflected wavefield.

**Laterally invariant media**

For the moment, it may be assumed that there are no lateral medium parameter variations. Hence, all wavefield quantities can be expressed in the lateral Fourier domain. It follows for the operator $\hat{\mathcal{H}}_2$:

$$\hat{\mathcal{H}}_2 = k_z^2 = \left(\frac{\omega}{c}\right)^2 - (k_x^2 + k_y^2), \tag{1.2.29}$$

where the 'hat' symbolizes quantities in the lateral wavenumber domain. The variables $k_x$ and $k_y$ are the horizontal wavenumbers and $k_z$ is the vertical wavenumber. The space dependence is given by $e^{i\mathbf{k}\cdot\mathbf{x}}$, where $\mathbf{k} = (k_x, k_y, k_z)$. For notational convenience, the

lateral wavenumber vector is defined: $\mathbf{k}_l = (k_x, k_y)$. Equation (1.2.29) is the dispersion relation of the wave equation. The operator $\hat{\mathcal{H}}_1$ is trivial:

$$\hat{\mathcal{H}}_1 = k_z = \frac{\omega}{c}\sqrt{1 - \frac{c^2|\mathbf{k}_l|^2}{\omega^2}}, \text{ for } 1 \geq \frac{c^2|\mathbf{k}_l|^2}{\omega^2}, \tag{1.2.30}$$

and

$$\hat{\mathcal{H}}_1 = k_z = i\frac{\omega}{c}\sqrt{\frac{c^2|\mathbf{k}_l|^2}{\omega^2} - 1}, \text{ for } 1 < \frac{c^2|\mathbf{k}_l|^2}{\omega^2}. \tag{1.2.31}$$

The latter equation causes exponentially decaying waves (evanescent waves) in the causal one-way solutions (see below). The case $1 = \frac{c^2|\mathbf{k}_l|^2}{\omega^2}$ corresponds to the critical angle of incidence for waves impinging on an interface with a positive velocity discontinuity, which causes a head wave to be produced. In terms of ray theory in smoothly varying velocity fields (Appendix A), this situation corresponds to the turning point where downgoing/upgoing rays reverse their direction. In the following, the head wave and turning ray phenomena are excluded from modelling and thus imaging/inversion. In the laterally homogeneous case the source free part of the equations (1.2.24) simplifies to:

$$\frac{\partial \hat{P}^{\pm}}{\partial z} = \mp ik_z\hat{P}^{\pm} + \frac{1}{2}\tilde{k}_z^{-1}\frac{d\tilde{k}_z}{dz}\hat{P}^{\mp}, \tag{1.2.32}$$

where $\tilde{k}_z = \frac{k_z}{\rho}$. The term $\frac{1}{2}\tilde{k}_z^{-1}\frac{d\tilde{k}_z}{dz}$ is the differential reflection coefficient per unit depth in a horizontally layered medium (compare to section 1.3.3). The key to formulating one-way propagators is that interactions between the downgoing and upgoing states are neglected. Consequently, the equations (1.2.32) decouple into two separate one-way wave equations:

$$\frac{\partial \hat{P}^{\pm}}{\partial z} = \mp ik_z\hat{P}^{\pm}. \tag{1.2.33}$$

The causal solutions (downward extrapolation for downgoing and upward extrapolation for upgoing states) are written in terms of discrete, recursive one-way propagators:

$$\hat{P}^+(z_i) = e^{-ik_z(z_i - z_{i-1})}\hat{P}^+(z_{i-1}) = \widehat{W}^+(z_i, z_{i-1})\hat{P}^+(z_{i-1}), \tag{1.2.34}$$

and

$$\hat{P}^-(z_{i-1}) = e^{+ik_z(z_{i-1} - z_i)}\hat{P}^-(z_i) = \widehat{W}^-(z_{i-1}, z_i)\hat{P}^-(z_i). \tag{1.2.35}$$

The propagators satisfy:

$$\widehat{W}^+(z_{i-1}, z_{i-1}) = \widehat{W}^-(z_i, z_i) = \hat{I}, \tag{1.2.36}$$

where $\hat{I}$ is the identity operator in the wavenumber domain.

**Laterally varying media**

If the scattering operator in equation (1.2.24) is neglected the source free, decoupled one-way wave equations for laterally varying media follow:

$$\frac{\partial P^{\pm}}{\partial z} = \mp i \mathcal{H}_1 P^{\pm}. \tag{1.2.37}$$

The (continuous) one-way propagators $W^{\pm}$ for laterally variant media are defined by:

$$\left( \frac{\partial}{\partial z} \mp i \mathcal{H}_1 \right) W^{\pm}(\mathbf{x}_l, z, \mathbf{x}_l', z') = 0, \tag{1.2.38}$$

complemented with the initial condition:

$$W^{\pm}(\mathbf{x}_l, z = z', \mathbf{x}_l', z') = \delta(\mathbf{x}_l - \mathbf{x}_l'), \tag{1.2.39}$$

where $\mathbf{x}_l = (x, y)$. Consider the functions $P^{\pm}(\mathbf{x}_l', z')$ that are solutions of the one-way wave equations (1.2.37). With the properties (1.2.38) and (1.2.39) one has:

$$P^{\pm}(\mathbf{x}_l, z) = \int W^{\pm}(\mathbf{x}_l, z, \mathbf{x}_l', z') P^{\pm}(\mathbf{x}_l', z') d\mathbf{x}_l', \tag{1.2.40}$$

hence the term propagator for $W^{\pm}$. Causality requires $z > z'$ for downward propagation $W^{+}$ and $z < z'$ for upward propagation $W^{-}$. From equation (1.2.39), the propagator can be solved by a Taylor series expansion with respect to $(z - z')$ (Grimbergen et al., 1998):

$$W^{\pm}(\mathbf{x}_l, z, \mathbf{x}_l', z') = \sum_{k=0}^{\infty} \frac{(z - z')^k}{k!} \frac{\partial^k W^{\pm}(\mathbf{x}_l, z, \mathbf{x}_l', z')}{\partial z^k} \bigg|_{z=z'}. \tag{1.2.41}$$

Using the properties (1.2.38) and (1.2.39) one has:

$$W^{\pm}(\mathbf{x}_l, z, \mathbf{x}_l', z') = \sum_{k=0}^{\infty} \frac{(z - z')^k}{k!} (\mp i)^k \mathcal{H}_1^k \delta(\mathbf{x}_l - \mathbf{x}_l'), \tag{1.2.42}$$

or formally:

$$W^{\pm}(\mathbf{x}_l, z, \mathbf{x}_l', z') = \exp\{\mp i \mathcal{H}_1 (z - z')\} \delta(\mathbf{x}_l - \mathbf{x}_l'). \tag{1.2.43}$$

Hence, the propagator $W^{\pm}$ acts as the kernel for the operator $\exp\{\mp i \mathcal{H}_1 (z - z')\}$ (Grimbergen et al., 1998). The Taylor expansion is valid for small extrapolation steps $z - z'$, that is, for the extrapolation across one thin slab $\Delta z = z_i - z_{i-1}$. The extension to larger

extrapolation steps is again achieved by recursive application of the exponential operator (depth ordered product representation). The causal downward propagator is:

$$W^+(\mathbf{x}_l, z, \mathbf{x}'_l, z') = \exp\{-i\mathcal{H}_1(z - z_{i-1})\} \prod_{j=1}^{i-1} \exp\{i\mathcal{H}_1(z_j - z_{j-1})\} \delta(\mathbf{x}_l - \mathbf{x}'_l), \quad (1.2.44)$$

where $z' \equiv z_0$ and $\mathcal{H}_1$ depends on depth $z$. The causal upward propagator $W^-$ is defined analogously. To warrant a compact notation in later equations one may write causal down- and upward propagation in product representation symbolically as:

$$W^\pm(\mathbf{x}_l, z, \mathbf{x}'_l, z') = \prod_{z'}^{z} \exp\{-i\mathcal{H}_1 \Delta z\} \delta(\mathbf{x}_l - \mathbf{x}'_l), \quad (1.2.45)$$

where $z > z'$ and $z < z'$ for downgoing- and upgoing waves, respectively, and $\Delta z > 0$ in both cases.

**Split-step propagator**

For computational purposes the operator $\mathcal{H}_1$ is expanded in terms of lateral slowness perturbations $\Delta s = s - s_0$ to the first order:

$$
\begin{aligned}
\mathcal{H}_1 &\approx \sqrt{(\omega s_0)^2 + \nabla_l^2} + \frac{d}{ds}\sqrt{(\omega s)^2 + \nabla_l^2}\bigg|_{s_0} \Delta s \\
&= \mathcal{H}_1^0 + \frac{\omega}{\sqrt{1 + \frac{1}{\omega^2 s_0^2}\nabla_l^2}} \Delta s,
\end{aligned}
\quad (1.2.46)
$$

where $s = 1/c$. The quantity $s_0$ equals the average lateral slowness within the slab $\Delta z$. The split-step approximation involves the negligence of the square-root in the denominator of equation (1.2.46) (Stoffa et al., 1990). This approximation yields for $\mathcal{H}_1$ simply:

$$\mathcal{H}_1 \approx \mathcal{H}_1^0 + \omega \Delta s, \quad (1.2.47)$$

and for the exponential operator in equation (1.2.45):

$$\exp\{-i\mathcal{H}_1 \Delta z\} \approx e^{-i(\mathcal{H}_1^0 + \omega \Delta s)\Delta z}, \quad (1.2.48)$$

where $\Delta z > 0$. The leading term $\mathcal{H}_1^0$ in the exponential is implemented as a phase-shift operator in the lateral Fourier domain (Gazdag, 1978). The second term is a vertical 'time-shift' that depends on the slowness perturbation $\Delta s$ and is applied in the space domain.

The relatively crude split-step approximation yields a simple and economical marching-type algorithm that shuttles between the lateral Fourier and space domain ('dual-domain implementation'). This approximation has proven to be sufficiently accurate in many situations. The hybrid split-step propagator, operating in both the space and the spatial wavenumber domain, becomes:

$$\exp\{-i\mathcal{H}_1\Delta z\} \approx e^{-i\omega\Delta s\Delta z}\mathcal{F}_{\mathbf{k}_l}^{-1}e^{-ik_z^0\Delta z}\mathcal{F}_{\mathbf{x}_l} = \mathcal{S}_{s_0}\mathcal{F}_{\mathbf{k}_l}^{-1}e^{-ik_z^0\Delta z}\mathcal{F}_{\mathbf{x}_l}, \tag{1.2.49}$$

where $\mathcal{F}_{\mathbf{x}_l}$ and $\mathcal{F}_{\mathbf{k}_l}^{-1}$ are the forward and inverse lateral Fourier transforms, respectively. The split-step operator symbol $\mathcal{S}_{s_0}$ has been introduced for later convenience. The vertical wavenumber is:

$$k_z^0 = s_0\omega\sqrt{1 - \frac{|\mathbf{k}_l|^2}{s_0^2\omega^2}}. \tag{1.2.50}$$

To investigate the accuracy of the split-step approximation consider the index $n = s_0c = \frac{c}{c_0}$ that is the ratio of the actual velocity $c$ and the reference velocity $c_0 = \frac{1}{s_0}$ within a slab $\Delta z$. The exact dispersion relation is expressed as:

$$\frac{ck_z}{\omega} = \sqrt{1 - \frac{c^2|\mathbf{k}_l|^2}{\omega^2}}, \tag{1.2.51}$$

and the split-step approximated dispersion relation becomes:

$$\frac{ck_z}{\omega} \approx n\sqrt{1 - \frac{c_0^2|\mathbf{k}_l|^2}{\omega^2}} - n + 1. \tag{1.2.52}$$

The accuracy of this approximation depends on the magnitude of $n = 1 + \delta n$. Figure 1.3 shows the split-step approximation for three different values of $\delta n$. For small contrasts the approximation is acceptable up to high tilt angles of propagation. In large contrast media the accuracy deteriorates quickly as the propagation angle increases. As opposed to finite-difference techniques that are obtained from a direct square-root expansion of the operator $\mathcal{H}_1$ (Claerbout, 1985), the split-step dispersion relation is exact when no lateral velocity variations are present.

**PSPI propagator**

Where strong lateral velocity variations are present, a more accurate extrapolation technique is necessary. There exist a number of techniques to achieve this (e.g., Ristow and
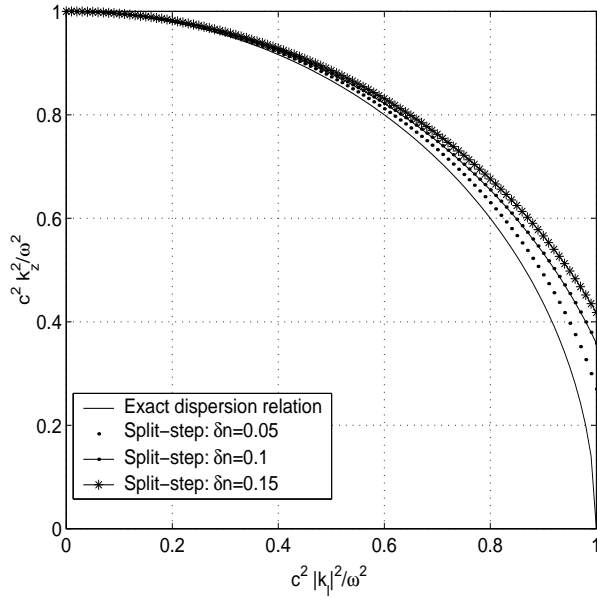
Figure 1.3: The exact dispersion relation and its split-step approximation corresponding to the equations (1.2.51) and (1.2.52), respectively. The split-step approximated dispersion relations are shown for three magnitudes of relative lateral velocity perturbation: $\delta n = 0.05, \delta n = 0.1$ and $\delta n = 0.15$.

Rühl (1994); Grimbergen et al. (1998)). One way to improve accuracy is to apply the split-step propagator in a wavefield windowing fashion. Gazdag and Sguazzero (1984) proposed the phase-shift-plus-interpolation (PSPI) technique to better account for significant lateral velocity variations. Kessinger (1992) combined the split-step approach with PSPI, hereafter referred to as the split-step PSPI technique. The extrapolation procedure consists essentially of two steps. First, the wavefield is phase-shift extrapolated across the thin slab $\Delta z$ for a number of reference slownesses $s_{ref}^n$, instead of just one average slowness $s_0$. This is followed by the split-step correction with respect to the reference slownesses $s_{ref}^n$. Second, the actual wavefield is computed by interpolating the resulting reference wavefields. Clearly, the split-step PSPI is sensitive to the reference slownesses $s_{ref}^n$ and a higher number of them results in a more accurate extrapolation. Bagaini et al. (1995) proposed an adaptive criterion for selecting the reference slownesses $s_{ref}^n = \frac{1}{c_{ref}^n}$ which has been adopted in this thesis. The wavefield copying and linear interpolation operator $\mathcal{C}_N$ and $\mathcal{E}_N$, respectively, are defined. The first operator creates $N$

identical wavefield copies, where $N$ is the number of selected reference slownesses $s_{ref}^n$ for a particular thin slab. Then, the $N$ wavefields are phase-shift extrapolated and split-step corrected with respect to the $N$ reference slownesses. The interpolation operator $\mathcal{E}_N$ combines the $N$ resulting reference wavefields $P_{ref}^{\pm,n}(\mathbf{x}_l, z)$ by a weighted summation in the space domain according to the actual velocity $c$:

$$P^{\pm}(\mathbf{x}_l, z) = \sum_{n=1}^{N} \alpha^n P_{ref}^{\pm,n}(\mathbf{x}_l, z), \tag{1.2.53}$$

where

$$\left.\begin{array}{l} \alpha^n = \dfrac{c_{ref}^{n+1} - c}{c_{ref}^{n+1} - c_{ref}^n} \\[2mm] \alpha^{n+1} = \dfrac{c - c_{ref}^n}{c_{ref}^{n+1} - c_{ref}^n} \end{array}\right\} \text{ if } c_{ref}^n \leq c \leq c_{ref}^{n+1}; \quad \left.\begin{array}{l} \alpha^n = 0 \\[2mm] \alpha^{n+1} = 0 \end{array}\right\} \text{ else,} \tag{1.2.54}$$

with $1 \leq n \leq N - 1$. The split-step PSPI propagator is symbolically summarized as:

$$\exp\{-i\mathcal{H}_1\Delta z\} \approx \mathcal{E}_N \mathcal{S}_{s_{ref}^n}^N \mathcal{F}_{\mathbf{k}_l}^{-1,N} e^{-ik_z^n\Delta z} \mathcal{C}_N \mathcal{F}_{\mathbf{x}_l}, \tag{1.2.55}$$

where

$$k_z^n = \frac{\omega}{c_{ref}^n} \sqrt{1 - \frac{(c_{ref}^n)^2 |\mathbf{k}_l|^2}{\omega^2}}, \tag{1.2.56}$$

and

$$\mathcal{S}_{s_{ref}^n}^N = e^{-i\omega\Delta s^n\Delta z}, \text{ with } \Delta s^n = s - s_{ref}^n. \tag{1.2.57}$$

The superscript N for the inverse Fourier transform $\mathcal{F}^{-1}$ and the split-step operator $\mathcal{S}$ indicates that both are to be applied N times. Depending on the lateral velocity profile within each slab either the phase-shift, the split-step, or the split-step PSPI propagator are used for wavefield extrapolation. This results in a flexible and adaptive marching-type algorithm. The wavefield propagators are calculated and applied for separate frequencies $\omega$, which makes the algorithm structure well suited for the implementation in a parallel computer architecture.

## 1.3 Linearized data modelling

In the previous section one-way wavefield propagators that extrapolate the wavefield from one depth level to the other have been introduced. In this part the forward mod-

elling formula is derived that relates the reflection operator $\mathcal{R}^+$ to the seismic surface data.

### 1.3.1 Primary data representation

The one-way Green's functions $G^{\pm}$ are defined (Wapenaar, 1996) as:

$$\left(\frac{\partial}{\partial z} \pm i\mathcal{H}_1\right) G^{\pm}(\mathbf{x}, \mathbf{x}') = \delta(\mathbf{x} - \mathbf{x}'), \tag{1.3.1}$$

where

$$G^+(\mathbf{x}, \mathbf{x}') = H(z - z')W^+(\mathbf{x}_l, z, \mathbf{x}'_l, z'), \tag{1.3.2}$$

and

$$G^-(\mathbf{x}, \mathbf{x}') = H(z' - z)W^-(\mathbf{x}_l, z, \mathbf{x}'_l, z'). \tag{1.3.3}$$

The Heaviside function $H$ generates the $\delta$-function in depth and forces the Green's functions to be causal. It is useful to introduce the reference one-way wave-equation:

$$\left(\frac{\partial}{\partial z} - \mathbf{B}_{ref}\right) \mathbf{G} = \mathbf{I}\delta(\mathbf{x} - \mathbf{x}'), \tag{1.3.4}$$

with the diagonal Green's matrix $\mathbf{G}$:

$$\mathbf{G}(\mathbf{x}, \mathbf{x}') = \begin{pmatrix} G^+(\mathbf{x}, \mathbf{x}') & 0 \\ 0 & G^-(\mathbf{x}, \mathbf{x}') \end{pmatrix}. \tag{1.3.5}$$

and the $2 \times 2$ identity matrix $\mathbf{I}$. The operator $\mathbf{B}_{ref}$ is the propagation operator $\mathbf{\Lambda}$:

$$\mathbf{B}_{ref} = \mathbf{\Lambda} = \begin{pmatrix} i\mathcal{H}_1 & 0 \\ 0 & -i\mathcal{H}_1 \end{pmatrix}. \tag{1.3.6}$$

That is, the reference solution does not include explicit scattering. The equation to be solved is:

$$\left(\frac{\partial}{\partial z} - \mathbf{B}\right) \mathbf{P} = \mathbf{S} S(\omega)\delta(\mathbf{x} - \mathbf{x}_s), \tag{1.3.7}$$

where $S(\omega)$ is the source's frequency signature and $\mathbf{x}_s$ the source location. It is useful to define the contrast operator $\mathbf{V} = \mathbf{B} - \mathbf{B}_{ref}$, so that the problem can be stated as:

$$\left(\frac{\partial}{\partial z} - \mathbf{B}_{ref}\right) \mathbf{P} = \mathbf{S} S(\omega)\delta(\mathbf{x} - \mathbf{x}_s) + \mathbf{V}\mathbf{P}, \tag{1.3.8}$$

or as an integral equation:

$$\mathbf{P}(\mathbf{x}) = \int \mathbf{G}(\mathbf{x}, \mathbf{x}')(\mathbf{S}(\mathbf{x}')S(\omega)\delta(\mathbf{x}' - \mathbf{x}_s) + \mathbf{V}(\mathbf{x}')\mathbf{P}(\mathbf{x}'))d\mathbf{x}', \tag{1.3.9}$$

or

$$\mathbf{P}(\mathbf{x}) = \mathbf{\underset{\sim}{G}}(\mathbf{x}, \mathbf{x}_s)\mathbf{S}(\mathbf{x_s})S(\omega) + \int \mathbf{\underset{\sim}{G}}(\mathbf{x}, \mathbf{x}')\mathbf{\underset{\sim}{V}}(\mathbf{x}')\mathbf{P}(\mathbf{x}')d\mathbf{x}'. \tag{1.3.10}$$

The iterative solution for this integral equation entails the Born series:

$$\mathbf{P}^n(\mathbf{x}) = \mathbf{\underset{\sim}{G}}(\mathbf{x}, \mathbf{x}_s)\mathbf{S}(\mathbf{x_s})S(\omega) + \int \mathbf{\underset{\sim}{G}}(\mathbf{x}, \mathbf{x}')\mathbf{\underset{\sim}{V}}(\mathbf{x}')\mathbf{P}^{n-1}(\mathbf{x}')d\mathbf{x}', \tag{1.3.11}$$

for $n > 0$ and $\mathbf{P}^0 = \mathbf{\underset{\sim}{G}}(\mathbf{x}, \mathbf{x}_s)\mathbf{S}(\mathbf{x_s})S(\omega)$. Choosing $n = 1$ yields the first order or linear Born approximation:

$$\mathbf{P}^1(\mathbf{x}) = \mathbf{\underset{\sim}{G}}(\mathbf{x}, \mathbf{x}_s)\mathbf{S}(\mathbf{x_s})S(\omega) + S(\omega)\int \mathbf{\underset{\sim}{G}}(\mathbf{x}, \mathbf{x}')\mathbf{\underset{\sim}{V}}(\mathbf{x}')\mathbf{\underset{\sim}{G}}(\mathbf{x}', \mathbf{x}_s)\mathbf{S}(\mathbf{x_s})d\mathbf{x}'. \tag{1.3.12}$$

The choice of the reference operator (1.3.6) leaves the contrast operator $\mathbf{\underset{\sim}{V}} = \mathbf{\underset{\sim}{\Theta}}$. Consider the primary upgoing response $P^-$ related to the source function for downgoing waves $S^+$ and disregard the direct wave. Moreover, if transmission effects are neglected above the target reflector represented by $\mathcal{R}^+(\mathbf{x}')$ (homogeneous or small contrast overburden) one obtains (Wapenaar, 1996):

$$P^-(\mathbf{x}) = S(\omega)\int W^-(\mathbf{x}, \mathbf{x}')\mathcal{R}^+(\mathbf{x}')W^+(\mathbf{x}', \mathbf{x}_s)S^+(\mathbf{x}_s)d\mathbf{x}'. \tag{1.3.13}$$

Finally, the operator $\mathcal{R}^+(\mathbf{x}'_l, z')$ is replaced by its convolution kernel $R^+(\mathbf{x}_{rl} - \mathbf{x}_{sl}, z')$ for specular reflections (see section 1.3.2), and equation (1.3.13) breaks down into three subprocesses (Wapenaar and Herrmann, 1996):

$$P^+(\mathbf{x}'_{sl}, z') = \int W^+(\mathbf{x}'_{sl}, z', \mathbf{x}_{sl}, z_0)S^+(\mathbf{x}_{sl}, z_0)d\mathbf{x}_{sl}, \tag{1.3.14}$$

$$P^-(\mathbf{x}'_{rl}, z') = \int R^+(\mathbf{x}'_{rl} - \mathbf{x}'_{sl}, z')P^+(\mathbf{x}'_{sl}, z')d\mathbf{x}'_{sl}, \tag{1.3.15}$$

and

$$P^-(\mathbf{x}_{rl}, z_0) = \int W^-(\mathbf{x}_{rl}, z_0, \mathbf{x}'_{rl}, z')P^-(\mathbf{x}'_{rl}, z')d\mathbf{x}'_{rl}, \tag{1.3.16}$$

where the source signature $S(\omega)$ has been dropped for simplicity. It is clear, however, that all subsequent equations are inherently bandlimited by $S(\omega)$. Ideally, the source signature should be deconvolved from the data. This requires the knowledge of the wavelet $S(\omega)$ which can be difficult to estimate. Deconvolution, if successful, increases the frequency bandwidth and enhances the resolution power of the seismic data. For horizontal interfaces separating regions of different medium parameters $R^+$ is a $\delta$-function in

depth. If more than one target reflector is considered, the omitted $z'$ integration in the equations (1.3.14) to (1.3.16) becomes relevant again. The reflection kernel $R^+$ links the local downgoing wavefield $P^+(\mathbf{x}'_{sl}, z')$ with the upgoing wavefield $P^-(\mathbf{x}'_{rl}, z')$ at the target reflector. In general, the convolution kernel in equation (1.3.15) is non-stationary to accommodate smooth lateral velocity variations directly above the reflecting interface. The non-stationarity is addressed in Section 1.3.4. In a strict sense, only horizontal interfaces are considered. A mathematically rigorous treatment of irregular interfaces is not straightforward. Therefore, the interfaces are assumed to be horizontal for now. Section 1.3.4 introduces an *ad hoc* reflector dip correction for specular reflections off moderately irregular interfaces based on ray theoretical considerations. The primary one-way representation with its three sub-processes is illustrated in Figure 1.4. The Section 1.3.3 discusses the effect of neglecting overburden transmission effects in more detail. Moreover, for the approximate validity of the primary representation in practical situations the following two pre-processing steps are required:

- decomposition of the physical measurements into one-way wavefields (i.e., 'deghosting'),

- elimination of multiple reflections related to the free surface.

In numerical data simulations these requirements are satisfied by absorbing boundary conditions in the computational subsurface model.

### 1.3.2 Specular reflection

To verify equation (1.3.13) for laterally invariant media, the reflection mechanism (1.3.15) is evaluated in the lateral Fourier domain. For horizontal interfaces the reflection kernel $R^+(\mathbf{x}_{rl} - \mathbf{x}_{sl}, z')$ becomes the differential operator $\frac{1}{2}\tilde{k}_{sz}^{-1}\frac{d\tilde{k}_{sz}}{dz'}\delta(z - z')$, where $k_{sz} = \tilde{k}_{sz}\rho$ is the vertical wavenumber of the impinging downgoing wavefield. Since the kernel is a multiplication operator in the Fourier domain, there is no conversion between different horizontal wavenumbers (specular reflection). The reflected upgoing wavefield as a function of the illuminating downgoing wavefield is thus:

$$\hat{P}^-(\mathbf{k}_{rl}, z') = \frac{1}{2}\tilde{k}_{sz}^{-1}\frac{d\tilde{k}_{sz}}{dz'}\hat{P}^+(\mathbf{k}_{sl}, z'), \tag{1.3.17}$$
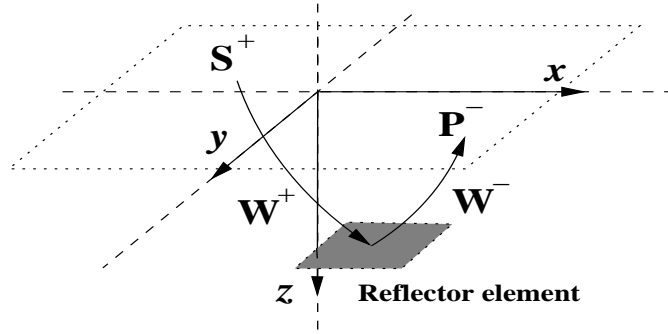
Figure 1.4: The primary one-way representation for seismic reflection data. Transmission losses due to energy partitioning at interfaces between the reference plane $z_0$ and the target reflector element are neglected. Note that the ray concept is invoked for illustration only.

where $\mathbf{k}_{rl} = \mathbf{k}_{sl}$ and $\mathbf{k}_{rz} = -\mathbf{k}_{sz}$ according to Snell's law. Moreover, in laterally invariant media phase-shift propagators link the source and receiver wavefields at $z_0$ with the local wavefields at $z'$ (Gazdag, 1978).

### 1.3.3 Acoustic reflection and transmission coefficients

In this section angle dependent (flux normalized) reflection and transmission coefficients for a plane boundary of two fluids are derived and discussed. This allows for a somewhat simplistic assessment of the errors involved in neglecting overburden transmission losses within the acoustic approximation. In reality, this assessment has limited validity. In an elastic medium, compressional waves that impinge on a medium discontinuity generate in part converted shear waves. That means compressional waves leak energy to the shear wavefield component, and compressional and shear waves can no longer be treated as being independent. When dealing with real-world data, the more realistic Zoeppritz equations for plane waves impinging on a plane boundary replace the fluid-fluid reflection and transmission coefficients (Aki and Richards, 1980). Fortunately, this does not change any of the migration/inversion concepts discussed in Chapter 2. It is clear, however, that any medium parameter inversion subsequent to acoustic migration/inversion is based on Zoeppritz's equations, not the acoustic approximation. Keeping this restriction is mind, it is justified to derive migration/inversion for compressional waves within the mathematically less involved acoustic approximation.

Situation 1:                                          Situation 2:

$P_1^+$ | $P_1^-=R^+P_1^+$     $P_1^+$          $P_1^-=T^-P_2^-$          $P_1^-=T^-P_2^-$

$P_2^+=T^+P_1^+$     $P_2^+=T^+P_1^+$     $P_2^-$     $P_2^+=R^-P_2^-$     $P_2^-$
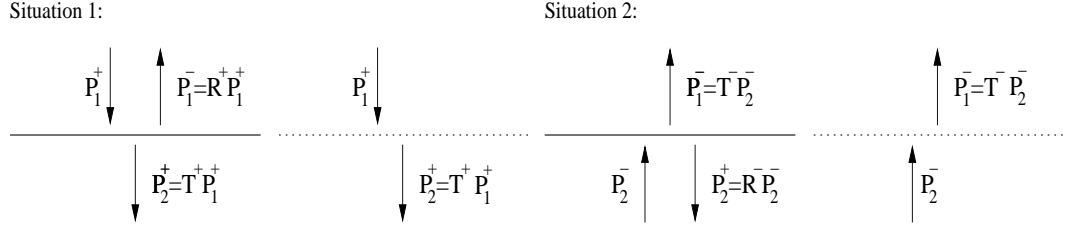
Figure 1.5: Flux normalized reflection and transmission at a medium discontinuity. Situation 1: In the left diagram incoming downgoing and reflected upgoing waves exist in the upper medium and only transmitted downgoing waves exist in the lower medium. Neglecting the reflected upgoing wave leaves only the flux normalized transmission process for downward extrapolation (right diagram). Situation 2: In the left diagram incoming upgoing and reflected downgoing waves exit in the lower medium and only transmitted upgoing waves exist in the upper medium. Again, neglecting the reflected downgoing wave leaves the flux-normalized transmission process for upward extrapolation (right diagram). The indices 1 and 2 stand for the wavefields in the upper and lower half of the medium, respectively. The transmission coefficients are identical in both cases: $T^+ = T^-$.

Consider the two situations illustrated in Figure 1.5. A plane boundary separates two homogeneous layers with velocities $c_1$ and $c_2$ and densities $\rho_1$ and $\rho_2$ for the first and second layer, respectively. Without loss of generality, the boundary is assumed to be perpendicular to the $z$ axis. In the first situation the incident downgoing wavefield $P_1^+$ and the reflected upgoing wavefield $P_1^-$ exist in the upper layer. Only the transmitted wave $P_2^+$ may exit in the lower medium. In the second situation the configuration is reversed. There are an incident upgoing wavefield and a downgoing reflection in the lower medium and a transmitted upgoing wavefield in the upper medium. The boundary conditions demand that the pressure $P$ and the normal particle velocity $V_z$ be continuous across the interface. With the equations (1.2.20) and (1.2.21) in the lateral wavenumber domain (assuming no lateral variations) the reflection coefficients $\tilde{R}^+$ and $\tilde{R}^-$ and the transmission coefficients $\tilde{T}^+$ and $\tilde{T}^-$ are (Wapenaar, 1998):

$$\tilde{R}^+ = \frac{\tilde{P}_1^-}{\tilde{P}_1^+} = \frac{\tilde{k}_{z1} - \tilde{k}_{z2}}{\tilde{k}_{z1} + \tilde{k}_{z2}}, \tag{1.3.18}$$

$$\tilde{R}^- = \frac{\tilde{P}_2^+}{\tilde{P}_2^-} = -\tilde{R}^+, \tag{1.3.19}$$

$$\tilde{T}^+ = \frac{\tilde{P}_2^+}{\tilde{P}_1^+} = \sqrt{\frac{\tilde{k}_{z,2}}{\tilde{k}_{z,1}}} \frac{2\tilde{k}_{z,1}}{\tilde{k}_{z,1} + \tilde{k}_{z,2}} = \sqrt{1 - (\tilde{R}^+)^2}, \tag{1.3.20}$$
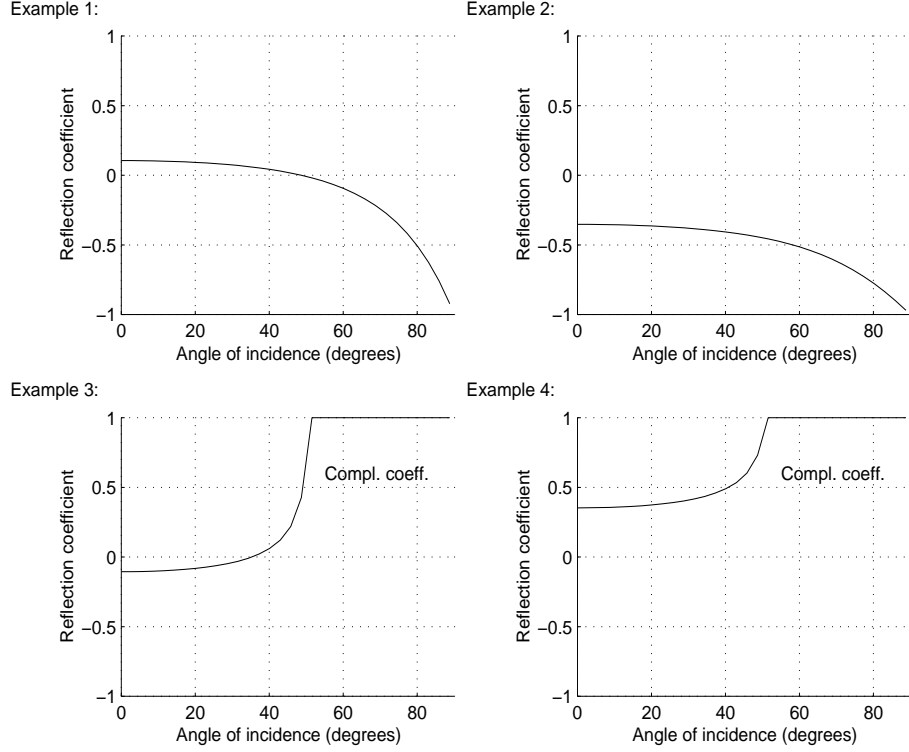
Figure 1.6: Four examples illustrating the angle dependence of the acoustic reflection coefficient $R^+$. Example 1: $c_1 = 2600\frac{m}{s}$, $c_2 = 2000\frac{m}{s}$, $\rho_1 = 1.4\frac{g}{cm^3}$ and $\rho_2 = 2.25\frac{g}{cm^3}$. Example 2: $c_1 = 2600\frac{m}{s}$, $c_2 = 2000\frac{m}{s}$, $\rho_1 = 2.25\frac{g}{cm^3}$ and $\rho_2 = 1.4\frac{g}{cm^3}$. Example 3: $c_1 = 2000\frac{m}{s}$, $c_2 = 2600\frac{m}{s}$, $\rho_1 = 2.25\frac{g}{cm^3}$ and $\rho_2 = 1.4\frac{g}{cm^3}$. Example 4: $c_1 = 2000\frac{m}{s}$, $c_2 = 2600\frac{m}{s}$, $\rho_1 = 1.4\frac{g}{cm^3}$ and $\rho_2 = 2.25\frac{g}{cm^3}$.

$$\tilde{T}^- = \frac{\tilde{P}_1^-}{\tilde{P}_2^-} = \sqrt{\frac{\tilde{k}_{z,1}}{\tilde{k}_{z,2}}} \frac{2\tilde{k}_{z,2}}{\tilde{k}_{z,1} + \tilde{k}_{z,2}} = \sqrt{1 - (\tilde{R}^+)^2}, \tag{1.3.21}$$

and

$$\tilde{T}^+ = \tilde{T}^-, \tag{1.3.22}$$

where $k_{z,1,2} = \sqrt{\frac{\omega^2}{c_{1,2}^2} - |\mathbf{k}_l|^2}$ and $\tilde{k}_{z,1,2} = \frac{k_{z,1,2}}{\rho_{1,2}}$. These relationships can be written in terms of angle of incidence $\theta$ using the plane wave parameterization with the horizontal ray parameter $p = \frac{\sin(\theta)}{c_1} = \frac{|\mathbf{k}_l|}{\omega}$ and Snell's law. The dispersion relation becomes $k_{z,1,2} = \frac{\omega}{c_{1,2}} \sqrt{1 - c_{1,2}^2 p^2}$. The reflection and transmission coefficients for situation 1 in the ray parameter/angle domain are:

$$R^+ = \frac{\rho_2 c_2 \sqrt{1 - c_1^2 p^2} - \rho_1 c_1 \sqrt{1 - c_2^2 p^2}}{\rho_2 c_2 \sqrt{1 - c_1^2 p^2} + \rho_1 c_1 \sqrt{1 - c_2^2 p^2}}, \tag{1.3.23}$$

$$T^+ = \frac{2\sqrt{\rho_2 c_2 \rho_1 c_1}\sqrt{1-c_2^2 p^2}\sqrt{1-c_1^2 p^2}}{\rho_2 c_2 \sqrt{1-c_1^2 p^2} + \rho_1 c_1 \sqrt{1-c_2^2 p^2}}. \tag{1.3.24}$$

The following observations for the angle dependent reflection coefficient $R^+$ are made:

- If $c_1 > c_2$ and $\rho_2 c_2 > \rho_1 c_1$, then the reflection coefficient will be a positive value for normal incidence. As $\theta$ increases, the reflection coefficient will decrease, reaching zero at the intramission angle $\theta_0$:

$$\frac{\rho_2}{\rho_1} = \frac{\sqrt{(c_1/c_2)^2 - \sin^2 \theta_0}}{\sqrt{1 - \sin^2 \theta_0}}. \tag{1.3.25}$$

  Beyond the intramission angle, the reflection coefficient decreases to a value of $-1$ at grazing incidence (example 1 in Figures 1.6 and 1.8).

- If $c_1 > c_2$ and $\rho_2 c_2 < \rho_1 c_1$, the reflection coefficient is always negative and equals $-1$ for grazing incidence (example 2 in Figures 1.6 and 1.8).

- If $c_2 > c_1$ the vertical wavenumber $\tilde{k}_{z2}$ becomes complex for angles greater than the critical angle $\theta_c$: $\sin(\theta_c) = c_1/c_2$. The wave amplitude is exponentially decaying in the lower medium (evanescent wave). By defining $\tilde{k}_{z2} = i\hat{k}_{z2} = i\frac{\omega}{c_2 \rho_2}\sqrt{c_2^2 p^2 - 1}$ one can write for postcritical reflections:

$$\hat{R}^+ = \frac{\tilde{k}_{z1} - i\hat{k}_{z2}}{\tilde{k}_{z1} + i\hat{k}_{z2}}. \tag{1.3.26}$$

  For postcritical reflections the magnitude is 1 (total reflection), and the induced phase shift is $\varphi = 2\tan^{-1}\left(\frac{\hat{k}_{z2}}{\tilde{k}_{z1}}\right)$ (examples 3 and 4 in Figures 1.6 and 1.8).

- For interfaces with a change in density only the reflection coefficient is angle independent: $\hat{R}^+ = R^+ = \frac{\rho_2 - \rho_1}{\rho_2 + \rho_1}$.

The flux-normalized transmission coefficients allows for a simplistic assessment of the errors involved in the negligence of transmission loss in the primary data representation (1.3.13). Consider the situation depicted in Figure 1.7. Assuming there is one extra interface between the target reflector element and the source/receiver datum one has the total transmission coefficient:

$$T^+ T^- = 1 - (R^+)^2, \tag{1.3.27}$$
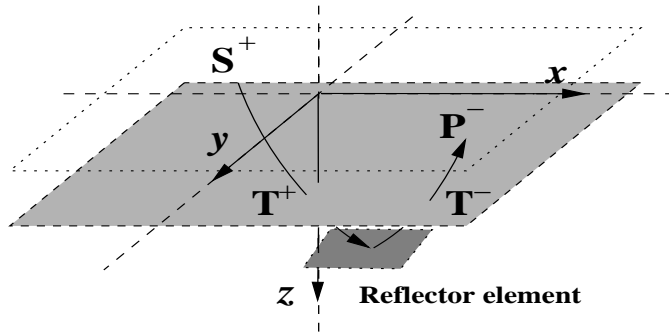
Figure 1.7: The primary one-way representation with one extra interface between the source/receiver datum and the target reflector element. The total transmission effect due to the additional interface is $T^+T^- = 1 - (R^+)^2$.

where $R^+$ is the reflection coefficient of the additional interface. Neglecting transmission loss thus causes an error $(R^+)^2$. Figure 1.8 shows the transmission coefficients and the associated error terms for the medium parameters in Figure 1.5. For small contrasts, the angle dependent transmission error is negligible. For complex media with many layers and significant scattering, the cumulative second- and higher order errors may become significant. In such a case the primary data formula (1.3.13) will produce erroneous amplitudes. Moreover, if the layering is fine, phase distortions can occur that result in dispersion effects not accounted for by equation (1.3.13) (Wapenaar and Herrmann, 1996).

### 1.3.4 DSR modelling

In this section the generalized DSR (double-square-root) modelling propagator is derived (Claerbout, 1985). The DSR propagator treats the source and receiver wavefields simultaneously and allows for a compact wavefield operator notation. The following development assumes that both sources and receivers have the same monopole characteristic. That is, their directional signatures are isotropic. Consider a multi-source and multi-receiver experiment. A number of single-source/multi-receiver experiments are carried out and combined to a single multi-source/multi-receiver dataset $\Psi$. Ideally, the entire reference plane $z_0$ is covered with source and receiver positions. In practice, of course, one has to deal with a finite survey area and finite recording aperture effects. The goal is to implement the primary modelling formula (1.3.13) for the multi-source/multi-receiver
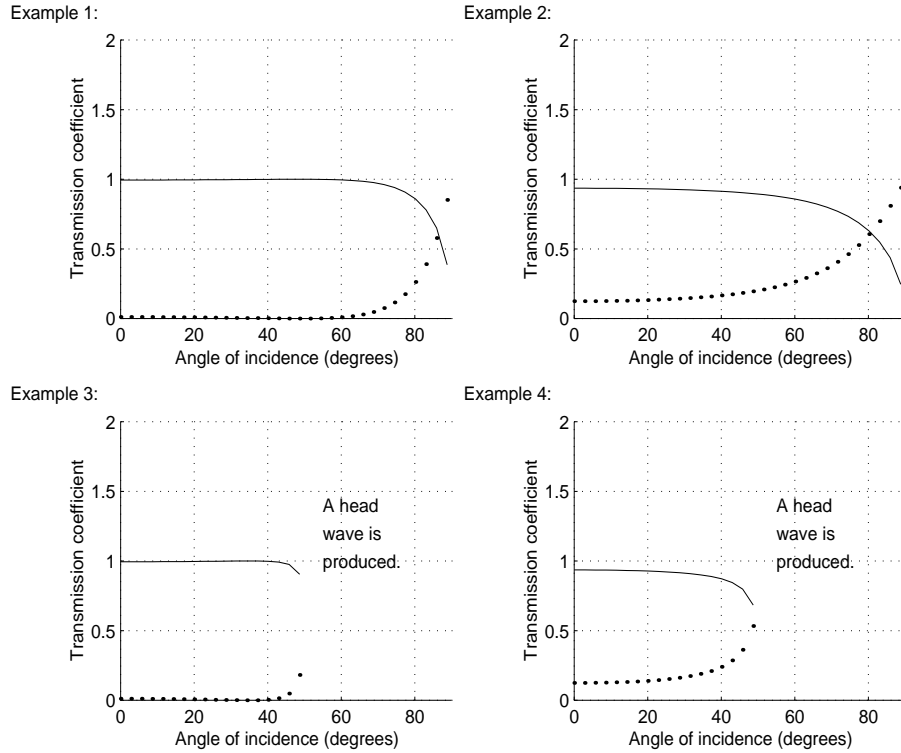
Figure 1.8: The flux normalized transmission coefficients $T^+ = T^-$ for the parameters in Figure 1.6 (solid line). The transmission error term $(R^+)^2$ is shown for comparison (dotted line). For small contrasts, the angle dependent transmission error is negligible. For complex media with significant scattering, the cumulative second- and higher order errors may become significant.

situation. The left hand side of equation (1.3.13) is understood as a function of the continuous receiver coordinate $\mathbf{x}_r = \mathbf{x}$ as well as of the continuous source coordinate $\mathbf{x}_s$. With the wavefield quantity $\Psi(\mathbf{x}_r, \mathbf{x}_s, z_0, \omega)$ representing the multi-source/multi-receiver dataset at the reference datum $z_0$ the modelling equation becomes:

$$\Psi(\mathbf{x}_r, \mathbf{x}_s, \omega) = \int W^-(\mathbf{x}_r, \mathbf{x}, \omega) \mathcal{R}(\mathbf{x}) W^+(\mathbf{x}, \mathbf{x}_s, \omega) d\mathbf{x}, \qquad (1.3.28)$$

where the $+$ sign for the reflection kernel has been dropped for notational convenience. The source term $S^+$ is assumed to be constant for all sources and, therefore, has been dropped as well. This might not be the case in practice and would have to be addressed during pre-processing. For clarity, the previously omitted frequency dependence is included as an argument. By exploiting the reciprocity relation $W^+(\mathbf{x}, \mathbf{x}_s, \omega) = W^-(\mathbf{x}_s, \mathbf{x}, \omega)$ (Wapenaar and Grimbergen, 1996) multi-source and multi-receiver mod-

| Space domain | Wavenumber domain | Ray domain |
|---|---|---|
| $\mathbf{x}_s = (x_s, y_s, z_s)$ | $\mathbf{k}_s = (k_{sx}, k_{sy}, k_{sz})$ | $\mathbf{p}_s = \frac{\mathbf{k}_s}{\omega}$ |
| $\mathbf{x}_r = (x_r, y_r, z_r)$ | $\mathbf{k}_r = (k_{rx}, k_{ry}, k_{rz})$ | $\mathbf{p}_r = \frac{\mathbf{k}_r}{\omega}$ |
| $\mathbf{x}_{sl} = (x_s, y_s)$ | $\mathbf{k}_{sl} = (k_{sx}, k_{sy})$ | $\mathbf{p}_{sl} = \frac{\mathbf{k}_{sl}}{\omega}$ |
| $\mathbf{x}_{rl} = (x_r, y_r)$ | $\mathbf{k}_{rl} = (k_{rx}, k_{ry})$ | $\mathbf{p}_{rl} = \frac{\mathbf{k}_{rl}}{\omega}$ |
| $\mathbf{m} = \frac{1}{2}(\mathbf{x}_{rl} + \mathbf{x}_{sl})$ | $\mathbf{k}_m = \mathbf{k}_{rl} + \mathbf{k}_{sl}$ | $\mathbf{p}_m = \frac{\mathbf{k}_m}{\omega}$ |
| $\mathbf{h} = \frac{1}{2}(\mathbf{x}_{rl} - \mathbf{x}_{sl})$ | $\mathbf{k}_h = \mathbf{k}_{rl} - \mathbf{k}_{sl}$ | $\mathbf{p}_h = \frac{\mathbf{k}_h}{\omega}$ |

Table 1.2: Nomenclature and relationships for the source-receiver and the midpoint-offset coordinate systems (Stolt and Benson, 1986).

elling is carried out in two stages. First, the source/receiver wavefield $\Psi_{loc}(\mathbf{x}_{rl}, \mathbf{x}_{sl}, z, \omega)$ directly above the reflecting interface is created. It exhibits the AVA related to the medium properties above and below the target reflector. The coupling mechanism between the local interface reflection coefficient and the local wavefield is explained further below. Second, the upward propagators for the sources and receivers link the local wavefield $\Psi_{loc}(\mathbf{x}_{rl}, \mathbf{x}_{sl}, z, \omega)$ to the wavefield $\Psi(\mathbf{x}_{rl}, \mathbf{x}_{sl}, z_0, \omega)$ at the reference plane $z_0$:

$$
\Psi(\mathbf{x}_{rl}, \mathbf{x}_{sl}, z_0, \omega) = \int\int W^-(\mathbf{x}_{rl}, z_0, \mathbf{x}'_{rl}, z, \omega) W^-(\mathbf{x}_{sl}, z_0, \mathbf{x}'_{sl}, z)
$$
$$
\times \ \Psi_{loc}(\mathbf{x}'_{rl}, \mathbf{x}'_{sl}, z, \omega) d\mathbf{x}'_{sl} d\mathbf{x}'_{rl}. \tag{1.3.29}
$$

Inserting the upward propagator from equation (1.2.45) for the source- and receiver propagators in equation (1.3.29) gives:

$$
\Psi(\mathbf{x}_{rl}, \mathbf{x}_{sl}, z_0, \omega) = \prod_z^{z_0} \exp\{-i(\mathcal{H}_{1\mathbf{s}}^{(S)} + \mathcal{H}_{1\mathbf{r}}^{(R)})\Delta z\} \Psi_{loc}(\mathbf{x}_{rl}, \mathbf{x}_{sl}, z, \omega), \tag{1.3.30}
$$

where $\mathcal{H}_{1\mathbf{s}}^{(S)}$ and $\mathcal{H}_{1\mathbf{r}}^{(R)}$ are the square-root operators for the sources and receivers, respectively, in source-receiver coordinates. At this point, it is convenient to introduce the midpoint-offset coordinate system. The lateral coordinates are transformed according to (Stolt and Benson, 1986):

$$
\mathbf{m} = \frac{1}{2}(\mathbf{x}_{rl} + \mathbf{x}_{sl}), \ \ \mathbf{h} = \frac{1}{2}(\mathbf{x}_{rl} - \mathbf{x}_{sl}), \ \text{ or } \ \mathbf{x}_{sl} = \mathbf{m} - \mathbf{h}, \ \ \mathbf{x}_{rl} = \mathbf{m} + \mathbf{h}, \tag{1.3.31}
$$

where $\mathbf{m}$ is the midpoint vector and $\mathbf{h}$ is the half offset vector. The half offset vector $\mathbf{h}$ is not to be confused with the full offset vector $\mathbf{x}_{rl} - \mathbf{x}_{sl}$. The descriptors 'half' and 'full' are mostly omitted in the following for the sake of brevity. Table 1.2 gives an overview over

the nomenclature and the relationships of some relevant quantities in the source-receiver and midpoint-offset coordinate systems. In midpoint-offset coordinates equation (1.3.30) reads:

$$\Psi(\mathbf{m}, \mathbf{h}, z_0, \omega) = \prod_z^{z_0} \exp\{-i(\mathcal{H}_{1\mathbf{m},\mathbf{h}}^{(S)} + \mathcal{H}_{1\mathbf{m},\mathbf{h}}^{(R)})\Delta z\}\Psi_{loc}(\mathbf{m}, \mathbf{h}, z, \omega), \qquad (1.3.32)$$

where $\mathcal{H}_{1\mathbf{m},\mathbf{h}}^{(S)}$ and $\mathcal{H}_{1\mathbf{m},\mathbf{h}}^{(R)}$ are the source and receiver square-root operators, respectively, expressed in midpoint-offset coordinates. This is the generalized form of Claerbout's (1985) DSR (double-square-root) propagator formulated within the context of wavefield modelling. Since the medium parameters are allowed to vary smoothly in the lateral direction, $\Psi_{loc}(\mathbf{m}, \mathbf{h}, z, \omega)$ is a function of the midpoint position $\mathbf{m}$. As mentioned earlier, the presented formalism is valid only for horizontal interfaces. However, for moderately irregular interfaces a local specular reflection mechanism is expected to hold (Aki and Richards, 1980). Therefore, irregular interfaces are approximated by piecewise planar and (dipping) reflector elements with angle dependent specular reflection coefficients as a function of midpoint location $\mathbf{m}$. Where the interface curvature is significant relative to the dominant wavelength of the local seismic wavefield, this subsurface parameterization breaks down in a dynamic sense. The scattering mechanism is then non-specular and the 'reflection coefficient' is merely a measure of diffraction scattering strength (Weglein and Stolt, 1999).

**Angle dependent modelling for moderately irregular interfaces**

The mechanism that couples the angle dependent reflection coefficient $R$ with the local source/receiver wavefield $\Psi_{loc}(\mathbf{m}, \mathbf{h}, z, \omega)$ is easiest analyzed in terms of the local slowness vectors (Appendix A). Consider the slowness vectors $\mathbf{p}_s$ and $\mathbf{p}_r$ for the local source and receiver wavefields, respectively (Figure 1.9 and Table 1.2). For moderately irregular interfaces the reflection mechanism is specular and source and receiver slowness vectors describe a rhombus with diagonals $\mathbf{d}_m = \mathbf{p}_r + \mathbf{p}_s$ and $\mathbf{d}_h = \mathbf{p}_r - \mathbf{p}_s$ in the reflection plane. The vector $\mathbf{d}_m$ consists of the horizontal midpoint slowness vector $\mathbf{p}_m$ and the vertical component $p_{mz}$. Similarly, the diagonal $\mathbf{d}_h$ consists of the horizontal offset slowness vector $\mathbf{p}_h$ and the vertical component $p_{hz}$. The modulus of $\mathbf{p}_h$ is the offset ray parameter: $p_h = |\mathbf{p}_h|$. The vector $\mathbf{d}_m$ is normal to the reflecting surface while the vector $\mathbf{d}_h$ is parallel
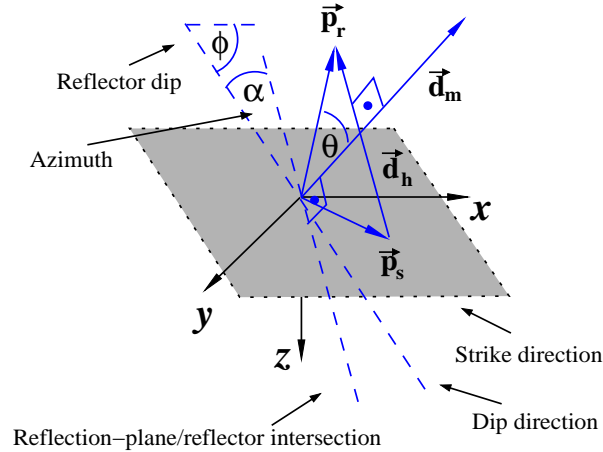
Figure 1.9: A source/receiver ray pair coincident at an interface. The locally planar interface generates a specular reflection. The source and receiver slowness vectors $\mathbf{p}_s$ and $\mathbf{p}_r$, respectively, are tangential to the rays. At the point of coincidence they describe a rhombus with diagonals $\mathbf{d}_m = \mathbf{p}_r + \mathbf{p}_s$ and $\mathbf{d}_h = \mathbf{p}_r - \mathbf{p}_s$ in the reflection plane. The vector $\mathbf{d}_h$ is parallel to the intersection of the reflection plane with the reflector. The vector $\mathbf{d}_m$ is normal vector to the reflector. $\theta$ is the angle of incidence measured against $\mathbf{d}_m$ and $\phi$ is dip angle of the reflector. The angle $\alpha$ is the azimuth defined as the angle between the reflection-plane/reflector intersection and the dip direction.

to the intersection of the reflection plane with the reflector surface. From Figure 1.9 one finds:

$$\sin\theta = \frac{|\mathbf{d}_h|}{2|\mathbf{p}_r|} = \frac{c(\mathbf{m})|\mathbf{d}_h|}{2} = \frac{c(\mathbf{m})|\mathbf{p}_h|}{2\sqrt{\cos^2\alpha\cos^2\phi + \sin^2\alpha}}, \tag{1.3.33}$$

where $\theta$ is the angle of incidence of the reflection coefficient in equation (1.3.23), $\phi$ is the reflector dip and $\alpha$ is the azimuth defined as the angle between the reflection-plane and reflector intersection with respect to the dip direction. The velocity $c(\mathbf{m})$ is the velocity directly above the reflection point at $(\mathbf{m}, z)$. Relationship (1.3.33) couples the joint source/receiver wavefield quantity $\mathbf{p}_h$ to the angle of incidence $\theta$ of the reflection coefficient in equation (1.3.23). The reflector dip $\phi$ and the azimuth $\alpha$ enter as local parameters that have to be provided. The azimuth $\alpha$ is determined from the dip direction and the horizontal offset slowness vector $\mathbf{p}_h$. The quantity $\sqrt{\cos^2\alpha\cos^2\phi + \sin^2\alpha}$ simplifies to $\cos\phi$ when the strike direction is normal to the reflection-plane. Because the reflection coefficient is frequency independent, the following procedure to set up the local (off-set Fourier transformed) wavefield $\Psi_{loc}(\mathbf{m}, \mathbf{k}_h, z, \omega)$ directly above the target reflector
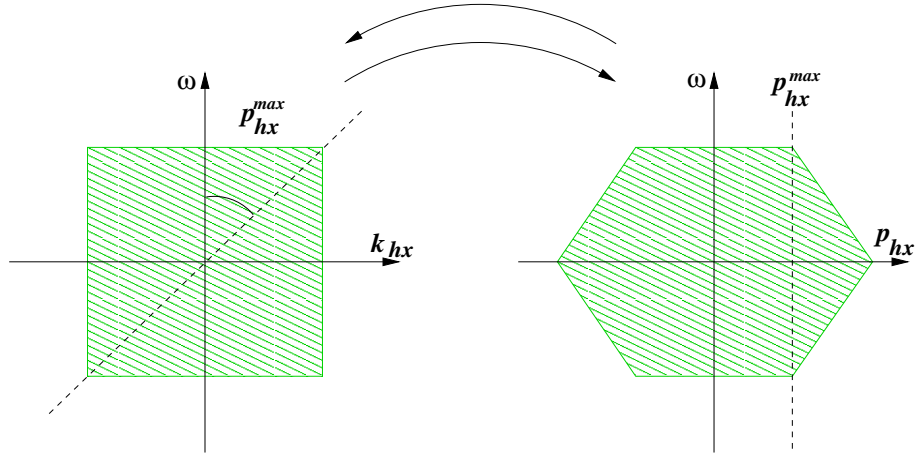
Figure 1.10: The radial trace transform (RTT) maps the $(\mathbf{k}_h, \omega)$ space into the $(\mathbf{p}_h, \omega)$ space (Appendix B). Only the planes $k_{hy} = 0$ and $p_{hy} = 0$ are shown. The RTT extracts the wavefield amplitudes along radial lines in the $(k_{hx}, \omega)$ space and maps the result into the $(p_{hx}, \omega)$ domain. In practice, the limited offset wavenumber range due to a finite recording aperture and the finite frequency band (shaded area) cause truncation effects in the $(p_{hx}, \omega)$ space. The maximum unbiased offset ray parameter is denoted by $p_{hx}^{max}$. The adjoint of RTT operator maps lines parallel to the $\omega$ axis into radial lines in the $(p_{hx}, \omega)$ domain (after Sava et al. (2001)). In three dimensions the transformation maps cones in the $(\mathbf{k}_h, \omega)$ space to cylinders in the $(\mathbf{p}_h, \omega)$ domain and vice versa.

results:

- calculate the angle dependent reflection coefficient using the medium properties above and below the interface at depth location $(\mathbf{m}, z)$,

- determine the local dip direction and dip angle $\phi$,

- convert the incidence angle $\theta$ to offset slowness using the parameter set $(\mathbf{p}_h; \phi, \alpha)$ according to equation (1.3.33) ,

- place the corresponding values for reflection coefficient in the $(\mathbf{p}_h, \omega)$ domain parallel to the $\omega$ axis,

- and, finally, transform the local reflection coefficient from the $(\mathbf{p}_h, \omega)$ domain into the local wavefield $\Psi_{loc}(\mathbf{m}, \mathbf{k}_h, z, \omega)$.

The last step is necessary to have the local wavefield in a format suitable for a recursive wavefield propagator that does not depend on the offset ray parameter. The conversion is achieved through the adjoint operator of the radial trace transform (RTT) in

the $(\mathbf{k}_h, \omega)$ domain (de Bruin et al., 1990; Prucha et al., 1999; Mosher and Foster, 2000; Sava et al., 2001). The RTT is recognized as an implementation of the better known $\tau - p$ transform (Appendix B). In modelling, the adjoint of the RTT operator is employed; for imaging/inversion, the RTT operator itself becomes important. The action of the RTT operator and its adjoint are illustrated in Figure 1.10. In the $(\mathbf{p}_h, \omega)$ domain the reflection coefficients are arranged parallel to the $\omega$ axis along concentric cylinders with radius $p_h = |\mathbf{p}_h|$. To obtain the corresponding local wavefield in the $(\mathbf{k}_h, \omega)$ domain the cylinders are mapped into cones determined by the ratio:

$$\mathbf{p}_h = \frac{\mathbf{k}_h}{\omega}. \tag{1.3.34}$$

This mapping, including the distribution of $R(\mathbf{m}, z, \theta)$ along the $\omega$ axis in the $(\mathbf{p}_h, \omega)$ domain, is formally expressed as:

$$\Psi_{loc}(\mathbf{m}, \mathbf{k}_h, z, \omega) = \mathcal{A}\mathcal{I}_\omega R(\mathbf{m}, z, \mathbf{p}_h; \phi, \alpha) = \mathcal{I}_\omega R(\mathbf{m}, z, \mathbf{p}_h; \phi, \alpha)|_{\mathbf{p}_h = \mathbf{k}_h/\omega}, \tag{1.3.35}$$

where $\mathcal{I}_\omega$ is the identity operator with respect to frequency. The operator $\mathcal{A}\mathcal{I}_\omega$ models the wavefield's amplitude variation as a function of ray parameter (AVP) rather than angle. Ray parameter and reflection angle are closely related through equation (1.3.33) and $\phi$ and $\alpha$ enter as external parameters. The mapping procedure is carried out at each midpoint location $\mathbf{m}$. A modelling algorithm based on this recipe appears rather cumbersome. Fortunately, in (least-squares) imaging/inversion this model parameterization is not carried out explicitly as to be explained in the next chapter. Finally, to have a more compact notation the generalized DSR upward propagator symbol for the joint source/receiver wavefield is introduced:

$$\mathcal{P}^{(SR)}(z_0, z) = \prod_{z}^{z_0} \exp\{-i(\mathcal{H}_{1\mathbf{m},\mathbf{h}}^{(S)} + \mathcal{H}_{1\mathbf{m},\mathbf{h}}^{(R)})\Delta z\}, \tag{1.3.36}$$

and, with the modelling operator $\mathcal{A}\mathcal{I}_\omega$, equation (1.3.32) becomes:

$$\Psi(\mathbf{m}, \mathbf{h}, z_0, \omega) = \int_{z_0}^{\infty} \mathcal{P}^{(SR)}(z_0, z)\mathcal{F}_{\mathbf{k}_h}^{-1}\mathcal{A}\mathcal{I}_\omega R(\mathbf{m}, z, \mathbf{p}_h; \phi, \alpha)dz, \tag{1.3.37}$$

where $\mathcal{F}_{\mathbf{k}_h}^{-1}$ is the inverse offset Fourier transform. The previously omitted $z$ integration has been included (multiple target reflectors), which automatically implies negligible
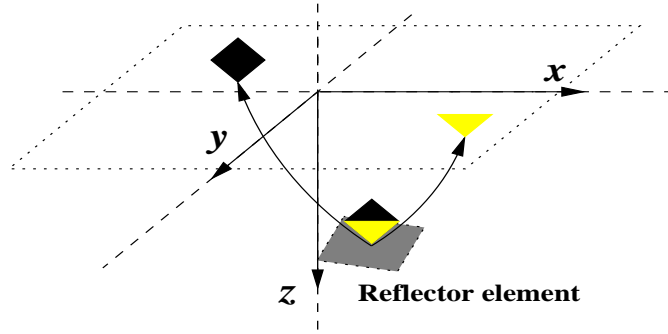
Figure 1.11: The 'survey-raising' thought experiment. Consider a source (diamond) and a receiver (triangle) located directly above the target reflector element. The amplitude variation with angle (AVA) of the wavefield directly above the reflector is proportional to angle dependent reflection coefficient $R(\mathbf{m}, z, \theta) \equiv R(\mathbf{m}, z, \mathbf{p}_h; \phi, \alpha)$. According to equation (1.3.32) the application of the 'double-square-root' propagator is equivalent to datuming the sources and receivers along their ray paths to the reference plane $z_0$.

transmission effects (low contrast media). The action of the (generalized) DSR propagator $\mathcal{P}^{(SR)}(z_0, z)$ can be regarded as datuming the local wavefield at the reflector datum $z$ to the source/receiver datum $z_0$. Figure 1.11 illustrates this with the 'survey-raising' thought experiment.

**Angle independent modelling**

Often in imaging no attention is paid to the angle behavior of the (local) wavefield. Only (angle dependent) amplitude changes due to propagation effects are considered, and the reflection coefficients are approximated by an angle independent average $R(\mathbf{m}, z)$ of $R(\mathbf{m}, z, \theta)$. If the reflection process is non-specular, $R(\mathbf{m}, z)$ is an angle independent measure of (diffraction) scattering strength. The operator $\mathcal{AI}_\omega$ in equation (1.3.35) simplifies greatly. Rather than mapping the corrected reflection coefficient into cones, the average coefficient is evenly distributed over the entire $(\mathbf{k}_h, \omega)$ space. Hence, the local wavefield is a constant function of $\mathbf{k}_h$, as opposed to slowly varying. In this case, the modelling operator $\mathcal{AI}_\omega$ is replaced by $\mathcal{I}_{\mathbf{k}_h, \omega}$. Effectively, the scattering mechanism does not exhibit angle dependence and simplifies to that of a reflector/diffractor with an angle independent radiation pattern. The local wavefield's offset dependence is then $\delta(h_x)\delta(h_y)$ at the reflector/diffractor location (Weglein and Stolt, 1999). In other words, the local wavefield

$\Psi_{loc}(\mathbf{m}, \mathbf{h} = 0, z, \omega)$ and the coefficient $R(\mathbf{m}, z)$ can be directly identified:

$$\Psi_{loc}(\mathbf{m}, \mathbf{h} = 0, z, \omega) = \mathcal{F}_{\mathbf{k}_h}^{-1} \mathcal{I}_{\mathbf{k}_h, \omega} R(\mathbf{m}, z) \equiv R(\mathbf{m}, z). \qquad (1.3.38)$$

An algorithm based on this parameterization ignores AVA effects and thus aims at structural rather than amplitude information.

**Implementation in laterally invariant media**

Consider a laterally invariant medium. All involved quantities are expressed in the midpoint-offset Fourier domain:

$$\Psi(\mathbf{k}_m, \mathbf{k}_h, z_0, \omega) = \int_{z_0}^{\infty} \hat{\mathcal{P}}^{(SR)}(z_0, z) \mathcal{A} \mathcal{I}_\omega R(\mathbf{k}_m, z, \mathbf{p}_h; \phi, \alpha) dz, \qquad (1.3.39)$$

where

$$\hat{\mathcal{P}}^{(SR)}(z_0, z) = \prod_{z}^{z_0} e^{-i k_z \Delta z}, \qquad (1.3.40)$$

with

$$k_z = k_{sz} + k_{rz} = \frac{\omega}{c} \left( \sqrt{1 - \frac{c^2 |\mathbf{k}_m + \mathbf{k}_h|^2}{4\omega^2}} + \sqrt{1 - \frac{c^2 |\mathbf{k}_m - \mathbf{k}_h|^2}{4\omega^2}} \right), \qquad (1.3.41)$$

hence the term 'double-square-root' propagator (Claerbout, 1985). For a computer implementation it is convenient to prescribe the modelling procedure in an algorithmic form. The depth integration in formula (1.3.39) is discretized according to:

$$\begin{aligned} \Psi(\mathbf{k}_m, \mathbf{k}_h, z_0, \omega) &= \Psi_{loc}(\mathbf{k}_m, \mathbf{k}_h, z_0, \omega) + \hat{\mathcal{P}}^{(SR)}(z_0, z_1) \Psi_{loc}(\mathbf{k}_m, \mathbf{k}_h, z_1, \omega) \\ &\quad + \hat{\mathcal{P}}^{(SR)}(z_0, z_2) \Psi_{loc}(\mathbf{k}_m, \mathbf{k}_h, z_2, \omega) + \dots, \end{aligned} \qquad (1.3.42)$$

where the quantity $\Psi_{loc}(\mathbf{k}_m, \mathbf{k}_h, z_{i-1}, \omega) = \mathcal{A} \mathcal{I}_\omega R(\mathbf{k}_m, z_i, \mathbf{p}_h; \phi, \alpha)$, $i = 1, 2, \dots$, is understood as the local wavefield integrated over one thin slab $\Delta z \equiv dz$. In recursive form, the reflection coefficient $R(\mathbf{k}_m, z_i, \theta) \equiv R(\mathbf{k}_m, z_i, \mathbf{p}_h; \phi, \alpha)$ at depth level $z_i$ is fed into the total wavefield previously upward propagated from the depth level below:

$$\Psi(\mathbf{k}_m, \mathbf{k}_h, z_{i-1}, \omega) = \hat{\mathcal{P}}^{(SR)}(z_{i-1}, z_i) \Psi(\mathbf{k}_m, \mathbf{k}_h, z_i, \omega) + \mathcal{A} \mathcal{I}_\omega R(\mathbf{k}_m, z_i, \mathbf{p}_h; \phi, \alpha), \quad (1.3.43)$$

where

$$\hat{\mathcal{P}}^{(SR)}(z_{i-1}, z_i) = e^{-i k_z \Delta z} \text{ and } i = 1, 2, \dots. \qquad (1.3.44)$$

The recursion is carried out for all depth levels of interest and initialized with a zero wavefield. Notice that in this notation the total wavefield $\Psi(\mathbf{k}_m, \mathbf{k}_h, z_i, \omega)$ contains the reflection scattering contributions from all previous depth levels.
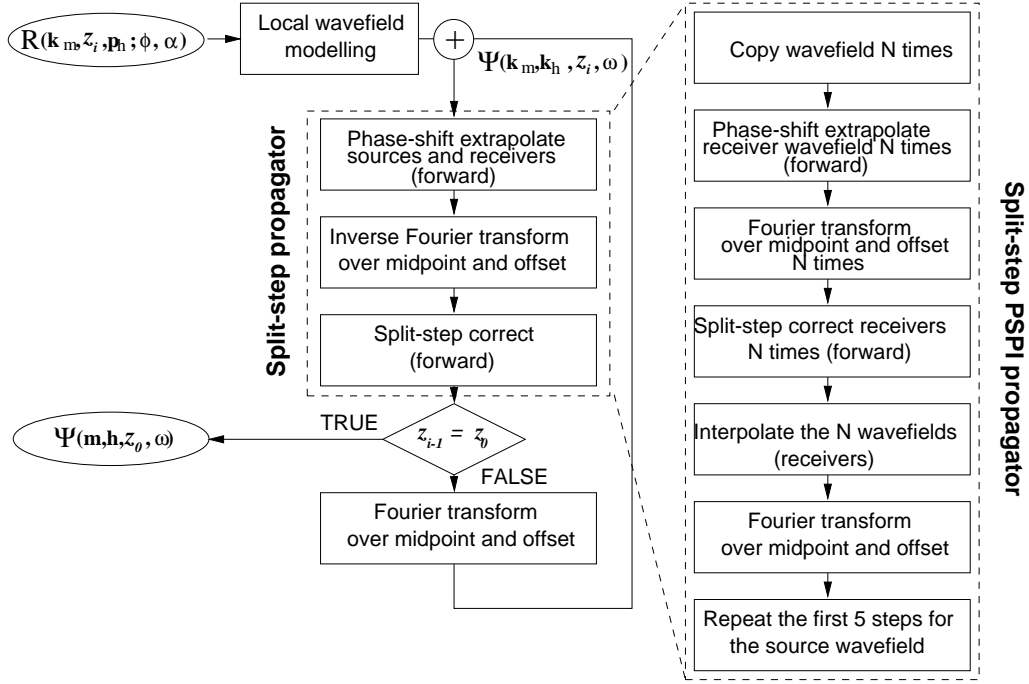
Figure 1.12: Flowchart for recursive generalized DSR modelling. Both the split-step DSR modelling and the split-step PSPI DSR modelling propagator are illustrated. The recursion is initialized with a zero wavefield and $i = 1, 2, \ldots$. For simplicity, the initial midpoint Fourier transform for the reflectivity $R$ has been omitted in the flowchart.

**Non-recursive DSR modelling**

An alternative, non-recursive, form of the DSR operator in laterally invariant media proves useful in the next section:

$$\Psi(\mathbf{k}_m, \mathbf{k}_h, z_0, \omega) = \int_{z_0}^{\infty} e^{-i \int_{z_0}^{z} k_z \, dz'} \mathcal{A} \mathcal{I}_\omega R(\mathbf{k}_m, z, \mathbf{p}_h; \phi, \alpha) dz, \qquad (1.3.45)$$

where the discrete slab thickness $\Delta z$ has been replaced by the differential $dz$. Instead of applying the phase-shift recursively, the cumulative phase-term is calculated and applied to the wavefield all at once, and the reflection contributions from all depth levels are integrated into the surface wavefield. As shown below, this form allows for the derivation of a DSR modelling formula for separate offsets $\mathbf{h}$. However, the non-recursive form (1.3.45) precludes the use of correction techniques such as the split-step approximation that make the DSR propagator suitable for laterally varying media.

**Separate offset DSR modelling**

If the scattering mechanism is reflection angle independent the offset-domain version of formula (1.3.45) follows:

$$
\begin{aligned}
\Psi(\mathbf{k}_m, \mathbf{h}, z_0, \omega) &= \int_{z_0}^{\infty} \mathcal{F}_{\mathbf{k}_h}^{-1} \left\{ e^{-i \int_{z_0}^{z} k_z dz'} \right\} \Psi_{loc}(\mathbf{k}_m, \mathbf{h} = \mathbf{0}, z, \omega) dz \\
&= \int_{z_0}^{\infty} \alpha(\mathbf{k}_m, \mathbf{h}, z_0, z, \omega) \Psi_{loc}(\mathbf{k}_m, \mathbf{h} = \mathbf{0}, z, \omega) dz,
\end{aligned} \qquad (1.3.46)
$$

where $\Psi_{loc}(\mathbf{k}_m, \mathbf{h} = \mathbf{0}, z, \omega) = \mathcal{F}_{\mathbf{k}_h}^{-1} \mathcal{I}_{\mathbf{k}_h,\omega} R(\mathbf{k}_m, z) \equiv R(\mathbf{k}_m, z)$. The inverse offset Fourier transform of the exponential in equation (1.3.46) entails the cumulative phase-shift term $\alpha(\mathbf{k}_m, \mathbf{h}, z_0, z, \omega)$ as a function of offset (Popovici, 1995). Clearly, this formula allows for the direct computation of separate offset data. The computational cost, however, is comparable to that of formula (1.3.45), since the phase-shift term still needs to be calculated for all involved wavenumbers. For the special case of zero-offset data $\Psi(\mathbf{k}_m, \mathbf{h} = \mathbf{0}, z_0, \omega)$ there exists a analytical stationary phase approximation (see also Appendix C) that allows for an easy computation of the phase-shift term $\alpha$. Within a constant factor this approximation amounts to setting $\mathbf{k}_h$ in equation (1.3.41) to zero (Stolt and Benson, 1986; Popovici, 1995; Alkhalifah, 2000):

$$
\Psi(\mathbf{k}_m, z_0, \omega) = \int_{z_0}^{\infty} e^{-i \int_{z_0}^{z} k_z dz'} \Psi_{loc}(\mathbf{k}_m, z, \omega) dz, \qquad (1.3.47)
$$

where

$$
k_z = \frac{2\omega}{c} \sqrt{1 - \frac{c^2 |\mathbf{k}_m|^2}{4\omega^2}}, \qquad (1.3.48)
$$

and

$$
\Psi_{loc}(\mathbf{k}_m, z, \omega) \equiv R(\mathbf{k}_m, z). \qquad (1.3.49)
$$

This is the 'exploding reflector' modelling formula (Claerbout, 1985) which forms the basis for post-stack migration. The local wavefield $\Psi_{loc}(\mathbf{k}_m, z, \omega)$ is set up by distributing the scattering coefficient $R(\mathbf{k}_m, z)$ over the frequency band to be modelled. A recursive implementation of equation (1.3.47) makes correction techniques that accommodate lateral velocity variations applicable.

**Implementation in laterally varying media**

Generalized DSR modelling in laterally heterogenous media is implemented using either the split-step or the split-step PSPI algorithm. First, consider the generalized DSR operator extended by the split-step correction (Popovici, 1996). The recursive algorithm follows:

$$\Psi(\mathbf{m}, \mathbf{h}, z_{i-1}, \omega) = \mathcal{P}^{(SR)}(z_{i-1}, z_i)\Psi(\mathbf{m}, \mathbf{h}, z_i, \omega) + \mathcal{F}_{\mathbf{k}_h}^{-1}\mathcal{A}\mathcal{I}_\omega R(\mathbf{m}, z_{i-1}, \mathbf{p}_h; \phi, \alpha), \quad (1.3.50)$$

where

$$\mathcal{P}^{(SR)}(z_{i-1}, z_i) = \mathcal{S}_{s_0}^{(SR)}\mathcal{F}_{\mathbf{k}_m}^{-1}\mathcal{F}_{\mathbf{k}_h}^{-1}e^{-i(k_{sz}^0 + k_{rz}^0)\Delta z}\mathcal{F}_{\mathbf{m}}\mathcal{F}_{\mathbf{h}}, \quad (1.3.51)$$

with

$$\mathcal{S}_{s_0}^{(SR)} = \mathcal{S}_{s_0}^{(S)}\mathcal{S}_{s_0}^{(R)} = e^{-i\omega(\Delta s^{(S)} + \Delta s^{(R)})\Delta z}. \quad (1.3.52)$$

The slowness perturbations for the sources and receivers, respectively, are:

$$\Delta s^{(S)} = s(\mathbf{m} - \mathbf{h}) - s_0 \text{ and } \Delta s^{(R)} = s(\mathbf{m} + \mathbf{h}) - s_0. \quad (1.3.53)$$

The wavefield at the initial depth level is zero. Figure 1.12 details the efficient computer implementation of split-step DSR modelling by means of a flowchart representation. Better accuracy is achieved with the split-step PSPI DSR propagator. Let

$$\mathcal{P}^{(S),(R)}(z_{i-1}, z_i) = \mathcal{E}_N^{(S),(R)}\mathcal{S}_{s_{ref}^n}^{(S),(R);N}\mathcal{F}_{\mathbf{k}_m}^{-1,N}\mathcal{F}_{\mathbf{k}_h}^{-1,N}e^{-ik_{sz,rz}^n\Delta z}\mathcal{C}_N\mathcal{F}_{\mathbf{m}}\mathcal{F}_{\mathbf{h}}, \quad (1.3.54)$$

and

$$\mathcal{S}_{s_{ref}^n}^{(S),(R);N} = e^{-i\omega\Delta s^{(S),(R);n}\Delta z}, \quad (1.3.55)$$

with

$$\Delta s^{(S),(R);n} = s(\mathbf{m} \mp \mathbf{h}) - s_{ref}^n. \quad (1.3.56)$$

With these definitions the split-step PSPI DSR propagator becomes:

$$\mathcal{P}^{(SR)}(z_{i-1}, z_i) = \mathcal{P}^{(S)}(z_{i-1}, z_i)\mathcal{P}^{(R)}(z_{i-1}, z_i), \quad (1.3.57)$$

which means that the receiver and the source component of the separable DSR propagator are applied consecutively. See Figure 1.12 for the flowchart representation of split-step PSPI modelling. The number of midpoint and offset Fourier transforms involved

in equation (1.3.57) ($2 \times (4 \times N + 4)$ per depth step) prohibits a practical implementation of the split-step PSPI propagator in three spatial dimensions. The computational burden is significantly reduced in two dimensions allowing for a feasible computer implementation for moderately sized datasets. For a more detailed discussion surrounding computational issues refer to Chapter 5.

**2.5-D DSR modelling**

The attention is now turned to the problem of seismic data collected along a 2-D line ($y_r = y_s = 0$) for a medium that does not vary in the $y$ direction. That is, the data collection is understood to be perpendicular to the reflector strike direction. The term 2.5-D refers to a modelling formula that is based on the $y$ invariance of the medium properties but yet approximately accounts for 3-D wavefield propagation effects (Stolt and Benson, 1986). Consider the DSR modelling equation in the form (1.3.45). Since the medium is invariant and the wavefield's offset dependence is singular along the $y$ coordinate, the local wavefield becomes: $\Psi_{loc}(k_{mx}, k_{hx}, z, \omega)\delta(k_{my}) = \mathcal{AI}_\omega R(k_{mx}, z, p_{hx}; \phi)\delta(k_{my})$, where $\mathcal{AI}_\omega$ is understood to be applied in 2-D. Equation (1.3.45) is now evaluated for the profile line $y_r = y_s = 0$ (Stolt and Benson, 1986):

$$
\begin{aligned}
\Psi_{2.5}(k_{mx}, k_{hx}, z_0, \omega) &= \int dk_{my} \int_{z_0}^{\infty} e^{-i\int_{z_0}^{z}(k_{sz}+k_{rz})dz'} \Psi_{loc}(k_{mx}, k_{hx}, z, \omega)\delta(k_{my})dz \\
&= \int_{z_0}^{\infty} \Psi_{loc}(k_{mx}, k_{hx}, z, \omega) \\
&\quad \times \int dk_{sy} \int dk_{ry} e^{-i\int_{z_0}^{z}(k_{sz}+k_{rz})dz'}\delta(k_{sy}+k_{ry})dz.
\end{aligned}
\tag{1.3.58}
$$

One of the $k_y$ integrals is trivial. The other one is solved by a stationary phase approximation (Appendix C), leading to:

$$
\Psi_{2.5}(k_{mx}, k_{hx}, z_0, \omega) = \int_{z_0}^{\infty} \mathcal{D}_{2.5}^{-1} e^{-i\int_{z_0}^{z}(k_{sz}+k_{rz})dz'} \Psi_{loc}(k_{mx}, k_{hx}, z, \omega)dz,
\tag{1.3.59}
$$

where

$$
\mathcal{D}_{2.5} = \sqrt{i\int_{z_0}^{z}(k_{sz}^{-1}+k_{rz}^{-1})dz'},
\tag{1.3.60}
$$

and $k_{sz}$ and $k_{rz}$ are evaluated at the stationary point $k_{sy} = k_{ry} = 0$. Dropping the factor $\mathcal{D}_{2.5}$ in the denominator is equivalent to the 2-D version of equation (1.3.45). The effect

of $\mathcal{D}_{2.5}^{-1}$ is to convert line sources into point sources (Stolt and Benson, 1986). Assuming a constant velocity earth and small propagation angles the expression for $\mathcal{D}_{2.5}$ simplifies to:

$$\mathcal{D}_{2.5} \approx \sqrt{i\omega 2 \frac{(z - z_0)}{c}} = \sqrt{i\omega t_{TWT}}, \tag{1.3.61}$$

where $t_{TWT}$ is the two-way travel-time. In practice, the phase-shift induced by $\sqrt{i\omega}$ is frequently ignored, but the amplitude scaling factor $\mathcal{D}_{2.5}^{-1} \approx (t_{TWT})^{-\frac{1}{2}}$ should be considered when 2-D formulas are to be applied to real-world data (Chapter 4).

# Chapter 2

# Seismic migration/inversion

Chapter 1 gives an extensive description of forward seismic data modelling based on wavefield propagators. The goal now is to invert the forward operator for the model parameters, the location and the relative magnitude of the (angle dependent) reflectivity. To this end imaging/inversion is cast into the framework of least-squares inversion. This approach yields both approximate analytical imaging/inversion formulas and iterative inversion schemes that lean upon well developed optimization techniques. An integral part of (least-squares) imaging/inversion is inverse wavefield extrapolation or back-propagation. Inverse one-way extrapolation requires the input of an *a priori* macro- or background velocity model. This model does not have to be the exact subsurface velocity. The macro-velocity model is a smooth representation of the true subsurface velocities that determines the travel-time or low frequency attributes of the seismic wavefield. The closer the model is to the truth the better. On the other hand, the one-way propagators do not account for fine detail. That means, even an exact velocity model is not expected to give fundamentally different results than a somewhat smoother representation. Hence, the logic of imaging/inversion is described as follows: A smooth macro-velocity model is provided to back-propagate the seismic wavefield into the subsurface and an AVP/AVA inversion/analysis yields the medium's short wavelength details (i.e., the angle dependent reflection coefficients). The procedure for building the macro-velocity model draws information from many different sources. These include geologic models or borehole information. One very important technique to infer velocity information is based on the imaging operator itself. The redundant illumination of each

subsurface point with waves impinging from different angles allows for a focusing analysis called 'migration velocity analysis' (e.g., Yilmaz and Chambers (1984), Biondi and Sava (1999)). If the 'correct' macro-velocity model is provided back-propagated waves originating from the same subsurface location should reproduce the same spatial image. Discrepancies, on the other hand, lead to an out-of-focus subsurface image. Focusing is achieved by recursively updating the macro-velocity model. As simple as it appears, migration velocity analysis requires significant effort and ingenuity and is the topic of ongoing geophysical research. The following chapter relies on the fact the macro-velocity model is sufficiently well known to ensure reasonably accurate wavefield propagation.

## 2.1  Least-squares inversion

The development of least-squares inversion adopts a description in terms of vectors and matrices. In the continuous case, vectors are elements of an infinite dimensional vector-space and matrices are linear operators. The vector-matrix description applies to discretized spaces and can easily be translated into computer code. The usually irregularly sampled wavefield data are sorted into midpoint-offset bins. This binning procedure results in a finite and discrete data vector $\mathbf{d}$ (in 'lexicographical arrangement') with an irregular pattern of live and dead traces (i.e., bins filled with zeros). The reflection coefficient $R(\mathbf{m}, z, \theta) \equiv R(\mathbf{m}, z, \mathbf{p}_h; \phi, \alpha)$ is discretized and arranged in a model vector $\mathbf{f}$ as a function of midpoint, depth and horizontal slowness by means of the relationship (1.3.33). That is, the model vector contains the ray parameter dependent common image gathers (CIGs) for all midpoint positions and the reflector dip angle $\phi$ and the azimuth $\alpha$ are implicit parameters in the model space vector $\mathbf{f}$. The discrete model and the binned data are related via the following linear system:

$$\mathbf{d} = \underset{\sim}{\mathbf{L}} \mathbf{f} + \mathbf{n}, \tag{2.1.1}$$

where $\underset{\sim}{\mathbf{L}}$ represents a numerical realization of the generalized recursive DSR modelling operator. The error term $\mathbf{n}$ stands for modelling errors, missing data and noise (Duijndam, 1988). The 2-D computer implementation utilizes phase-shift, split-step, or split-step PSPI propagators, depending on the complexity of macro-velocity field. A 3-D implementation has not been attempted.

The linear system is inverted using the Bayesian approach (e.g., Menke (1984), Tarantola (1987)) by seeking the maximum of the *a posteriori* probability density function (pdf):

$$p(\mathbf{f}|\mathbf{d}) \sim p(\mathbf{d}|\mathbf{f})p(\mathbf{f}), \tag{2.1.2}$$

where $p(\mathbf{d}|\mathbf{f})$ is the likelihood function and $p(\mathbf{f})$ the *a priori* distribution of the model vector. This solution to the inverse problem is called the MAP (maximum *a posteriori* probability) estimator. Assuming a Gaussian distribution for the seismic wavefield data the likelihood function is given by the normal distribution with data covariance matrix $\mathbf{C}_d$:

$$p(\mathbf{d}|\mathbf{f}) \sim e^{-\frac{1}{2}(\mathbf{d}-\mathbf{L}\mathbf{f})^T \mathbf{C}_d^{-1}(\mathbf{d}-\mathbf{L}\mathbf{f})}. \tag{2.1.3}$$

Unfortunately, seldom in seismic data processing is there a good estimate of the data covariance. However, empty bins are accommodated by choosing $\mathbf{C}_d$ to be diagonal with entries $\sigma_d^2 \gg 1$ for the dead traces and $\sigma_d^2 = 1$ for live data. For the moment, let the prior model distribution be normal with a diagonal covariance matrix with constant variance. To simplify the problem the diagonal weighting matrix $\mathbf{W}$ is introduced such that $\mathbf{C}_d^{-1} = \mathbf{W}^T\mathbf{W}$. That is, weights much smaller than one are assigned to empty bins and weights of magnitude one to live traces (unless the live traces exhibit an assessable variance). The maximum *a posteriori* solution to the inverse problem is the solution that minimizes the following cost or objective function:

$$\min \ F(\mathbf{f}) = \|\mathbf{W}(\mathbf{d} - \mathbf{L}\mathbf{f})\|^2 + \frac{1}{\sigma_f^2}\|\mathbf{f}\|^2. \tag{2.1.4}$$

This is the standard, weighted least-squares inverse problem with damping regularization (Menke, 1984). The solution is the well-known normal equation:

$$\mathbf{f}_{LS} = (\mathbf{L}'\mathbf{W}^T\mathbf{W}\mathbf{L} + \frac{1}{\sigma_f^2}\mathbf{I})^{-1}\mathbf{L}'\mathbf{W}^T\mathbf{W}\mathbf{d}, \tag{2.1.5}$$

where the operator $\mathbf{L}'$ is the adjoint of the modelling operator $\mathbf{L}$. In terms of matrix algebra, the adjoint is obtained by transposition and complex conjugation. From the structure of the normal equations it is clear that applying the adjoint operator $\mathbf{L}'$ yields a first approximation of the model vector. Indeed, conventional migration imaging is defined as the adjoint of modelling (Claerbout, 1992):

$$\mathbf{f}_{MIG} = \mathbf{L}'\mathbf{d}. \tag{2.1.6}$$

The data weighting operator $\underline{\mathbf{W}}^T\underline{\mathbf{W}}$ is omitted here, since it does not have any influence on the migration result when incomplete data sampling is the issue.

Instead, the more general least-squares solution can be obtained by minimizing the cost function (2.1.4) with a gradient optimization technique. To this end, the modelling and the migration operators $\underline{\mathbf{L}}$ and $\underline{\mathbf{L}}'$, respectively, need to be applied recursively. This also opens up the opportunity to incorporate more sophisticated model regularization techniques (i.e., a non-diagonal model covariance matrix). However, first the focus is on the migration operator $\underline{\mathbf{L}}'$ and its improvements derived from the least-squares inversion approach.

## 2.2 Seismic migration

Consider the generalized DSR modelling operator as given by equation (1.3.37):

$$\Psi(\mathbf{m}, \mathbf{h}, z_0, \omega) = \int_{z_0}^{\infty} \mathcal{P}^{(SR)}(z_0, z)\mathcal{F}_{\mathbf{k}_h}^{-1}\mathcal{A}\mathcal{I}_\omega R(\mathbf{m}, z, \mathbf{p}; \phi, \alpha)dz. \qquad (2.2.1)$$

In the discrete inverse problem the following identifications are made:

$$\mathbf{d} \equiv \Psi(\mathbf{m}, \mathbf{h}, z_0, \omega), \qquad (2.2.2)$$

$$\underline{\mathbf{L}} \equiv \int_{z_0}^{\infty} dz\,\mathcal{P}^{(SR)}(z_0, z)\mathcal{F}_{\mathbf{k}_h}^{-1}\mathcal{A}\mathcal{I}_\omega, \qquad (2.2.3)$$

$$\mathbf{f} \equiv R(\mathbf{m}, z, \mathbf{p}; \phi, \alpha). \qquad (2.2.4)$$

The application of the migration operator $\underline{\mathbf{L}}'$ in $\mathbf{f}_{MIG} = \underline{\mathbf{L}}'\mathbf{d}$ involves taking the individual adjoint operators and reversing their order: [1]

$$R_{MIG}(\mathbf{m}, z, \mathbf{p}_h; \phi, \alpha) = \int d\omega \mathcal{A}'\mathcal{F}_{\mathbf{h}}\mathcal{P}^{(RS)'}(z, z_0)\Psi(\mathbf{m}, \mathbf{h}, z_0, \omega), \qquad (2.2.5)$$

where $\mathcal{P}^{(RS)'}(z, z_0) = \left[\mathcal{P}^{(SR)}(z_0, z)\right]'$. Migration involves two distinct steps. First, the data $\Psi(\mathbf{m}, \mathbf{h}, z_0, \omega)$ are back-propagated by the adjoint operator $\mathcal{P}^{(RS)'}(z, z_0)$. Consider, for the moment, the DSR phase-shift propagator $\hat{\mathcal{P}}^{(SR)}(z_0, z)$ in equation (1.3.40). If the evanescent modes in the upward propagator $\hat{\mathcal{P}}^{(SR)}(z_0, z)$ are neglected, the adjoint phase-shift propagator (the anti-causal downward propagator) is in fact the inverse. The

---

[1]The adjoint of the linear integration operator $\int dz$ is the identity $\mathcal{I}_z$. A similar relationship holds with respect to the frequency variable: $\left[\int d\omega\right]' = \mathcal{I}_\omega$.

evanescent solutions decay exponentially and do not contribute significantly to the seismic wavefield. Therefore, this is a very good approximation. Second, the cascaded operators $\int d\omega \mathcal{A}'$ estimate the model $R_{MIG}(\mathbf{m}, z, \mathbf{p}_h; \phi, \alpha)$. Effectively, $\int d\omega \mathcal{A}'$ is the RTT (Appendix B) in the $(\mathbf{k}_h, \omega)$ space followed by a summation over frequency (Figure 1.10). The summation over frequency is equivalent to the classical migration imaging condition (e.g., Claerbout (1985)). Stolt and Weglein (1985) interpret the frequency summation in terms of the causality principle.

**Implementation in laterally varying media**

Modelling and migration in heterogenous media are implemented by recursive extrapolation. The recursive form of the DSR modelling formula (1.3.50) is reiterated for easier comparison:

$$\Psi(\mathbf{m}, \mathbf{h}, z_{i-1}, \omega) = \mathcal{P}^{(SR)}(z_{i-1}, z_i)\Psi(\mathbf{m}, \mathbf{h}, z_i, \omega) + \mathcal{F}_{\mathbf{k}_h}^{-1}\mathcal{A}\mathcal{I}_\omega R(\mathbf{m}, z_i, \mathbf{p}_h; \phi, \alpha), \quad (2.2.6)$$

with the $\mathcal{P}^{(SR)}(z_{i-1}, z_i)$ operator as defined in equation (1.3.51) for split-step propagation, and in equations (1.3.54) and (1.3.57) for split-step PSPI propagation. The adjoint procedure, the migration algorithm, follows:

$$\Psi(\mathbf{m}, \mathbf{h}, z_i, \omega) = \mathcal{P}^{(RS)'}(z_i, z_{i-1})\Psi(\mathbf{m}, \mathbf{h}, z_{i-1}, \omega), \quad (2.2.7)$$

and

$$R_{MIG}(\mathbf{m}, z_i, \mathbf{p}_h; \phi, \alpha) = \int d\omega \mathcal{A}'\mathcal{F}_{\mathbf{h}}\Psi(\mathbf{m}, \mathbf{h}, z_i, \omega). \quad (2.2.8)$$

The adjoint DSR propagator in terms of the split-step propagation is (Figure 2.1):

$$\mathcal{P}^{(RS)'}(z_i, z_{i-1}) = \mathcal{F}_{\mathbf{k}_m}^{-1}\mathcal{F}_{\mathbf{k}_h}^{-1}e^{i(k_{rz}^0 + k_{sz}^0)\Delta z}\mathcal{F}_{\mathbf{m}}\mathcal{F}_{\mathbf{h}}S_{s_0}^{(RS)'}, \quad (2.2.9)$$

with

$$\mathcal{S}_{s_0}^{(RS)'} = \mathcal{S}_{s_0}^{(R)'}\mathcal{S}_{s_0}^{(S)'} = e^{i\omega(\Delta s^{(R)} + \Delta s^{(S)})\Delta z}. \quad (2.2.10)$$

Apart from the sign change in the argument of the complex exponentials, the split-step modelling and migration operators differ only by the order in which they apply the split-step correction. Similarly, the adjoint split-step PSPI propagator follows (Figure 2.1):

$$\mathcal{P}^{(RS)'}(z_i, z_{i-1}) = \mathcal{P}^{(R)'}(z_i, z_{i-1})\mathcal{P}^{(S)'}(z_i, z_{i-1}), \quad (2.2.11)$$
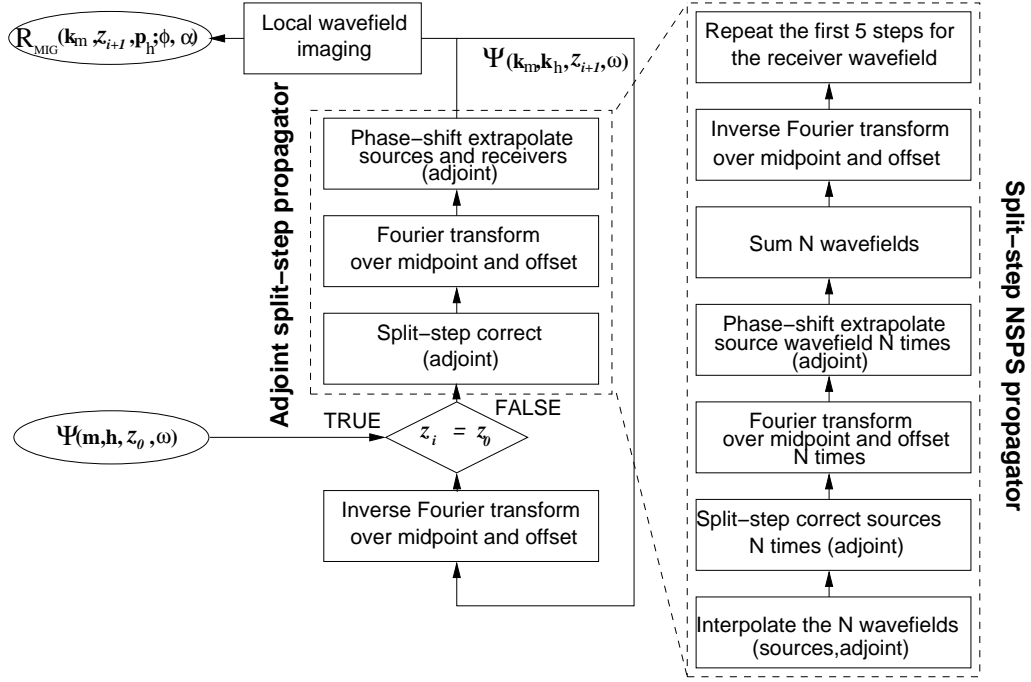
Figure 2.1: Flowchart for recursive generalized DSR migration $\underline{\mathbf{L}}'$. Both the split-step DSR migration and the split-step PSPI DSR migration propagator are illustrated ($i = 0, 1, 2 \ldots$). Compare to the modelling flowchart in Figure 1.12. For simplicity, the final midpoint Fourier transform for the estimate $R_{MIG}$ has been omitted in the flowchart.

with

$$\mathcal{P}^{(R)',(S)'}\left(z_i, z_{i-1}\right) = \mathcal{F}_{\mathbf{k}_m}^{-1} \mathcal{F}_{\mathbf{k}_h}^{-1} \mathcal{C}'_N e^{i k_{rz,sz}^n \Delta z} \mathcal{F}_{\mathbf{m}}^N \mathcal{F}_{\mathbf{h}}^N \mathcal{S}_{s_{ref}^n}^{(R)',(S)';N} \mathcal{E}_N^{(S)',(R)'}, \qquad (2.2.12)$$

where

$$\mathcal{S}_{s_{ref}^n}^{(R)',(S)';N} = e^{i\omega \Delta s^{(R),(S);n} \Delta z}. \qquad (2.2.13)$$

The adjoint split-step PSPI propagator corresponds to the windowed non-stationary-phase-shift (NSPS) propagator described by Margrave and Ferguson (1999). First the sources and then the receivers are back-propagated. At the entry stages of each recursion step, the adjoint linear interpolation operator $\mathcal{E}_N^{(S)',(R)'}$ distributes the weighted initial wavefield into N reference wavefields with weights according to equation (1.2.54). The adjoint wavefield copying operator $\mathcal{C}'$ simply amounts to a summation of the N reference wavefields.
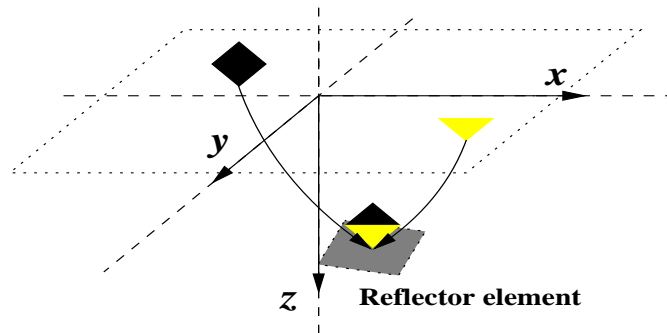
Figure 2.2: The 'survey-sinking' thought experiment. Consider a source (diamond) and a receiver (triangle) located at the reference plan $z_0$. The 'adjoint' operation to equation (1.3.32) can be thought of as datuming the sources and receivers along their ray paths back to the reflector location.

It is important to note that if the split-step NSPS propagator were used for modelling in Chapter 1, the split-step PSPI migration operator would result as a consequence. Whether one propagator technique should be given preference over the other for either modelling or migration is not obvious. This ambiguity stems from the fact that neither the split-step nor the split-step PSPI/NSPS propagator are symmetric. Symmetry is relatively easily restored in split-step propagation by applying half of the split-step 'time-shift' before and the other half after the phase-shift operator (Lee et al., 1991). The split-step PSPI/NSPS propagators can also be made symmetric (Ferguson and Margrave, 2002). Unfortunately, the symmetric version of split-step PSPI/NSPS propagation requires significantly more computational effort. Whether the symmetric propagators hold any numerical advantages for least-squares migration has not been investigated. However, a comparative test in Chapter 3 demonstrates that split-step NSPS and split-step PSPI perform equally well for zero-offset migration.

The recursive computer implementation of generalized DSR migration is illustrated in Figure 2.1. Compare the schematic flowchart also to Figure 1.12. Figure 2.2 interprets the duality between modelling and migration by invoking the 'survey-sinking' thought experiment as the 'adjoint of survey-raising' in Figure 1.11.

**Angle independent migration**

The above modelling and migration formulas all contain the ray parameter dependent operators $\mathcal{AI}_\omega$ and $\int d\omega \mathcal{A}'$, respectively. It is clear, however, that nothing changes in terms of wavefield propagation when these operators are replaced with their ray parameter independent counterparts, $\mathcal{I}_{\mathbf{k}_h,\omega}$ from equation (1.3.38) and its adjoint $\int d\mathbf{k}_h \int d\omega$. For migration, the result is the more conventional DSR imaging formula (Claerbout, 1985) that is suitable for structural imaging. The adjoint operation $\int d\mathbf{k}_h \int d\omega$ evaluates the local wavefield at $t = 0$ and $\mathbf{h} = 0$. This is in agreement with the concept of a local wavefield collapsing to an offset $\delta$-function at the image point. This is also equivalent to summing (stacking) the ray parameter CIGs along the ray parameter axis which effectively averages the angle dependent reflection coefficients. Chapter 3 has examples for both angle-independent and angle-dependent migration.

**Zero-offset migration**

So far, all described imaging operators fall into the category of pre-stack migration. In practice, pre-stack imaging is sometimes replaced by a simplified post-stack imaging strategy that separates the imaging process into two stages. First, the data are normal-move-out (NMO) corrected and stacked to approximately simulate zero-offset data. Second, zero-offset migration yields the structural image based on the adjoint of the modelling formula (1.3.47):

$$R_{MIG}(\mathbf{k}_m, z) = \int e^{i \int_{z_0}^{z} k_z dz'} \Psi(\mathbf{k}_m, z_0, \omega) d\omega. \tag{2.2.14}$$

Again, a recursive implementation with an appropriate operator expansion takes care of lateral velocity variations. This is exemplified in Chapter 3 for zero-offset modelling and migration using split-step and split-step PSPI/NSPS propagators.

## 2.2.1 Ray parameter imaging Jacobian

If ray parameter/angle information is to be extracted from the local wavefield an improved migration formula should be considered. One way to improve the migration is by recognizing that migration involves changing from the data space ($\omega$ dependence) to the model space ($z$ dependence) and therefore constitutes a change of variables that

should ideally consider the corresponding (imaging) Jacobian (Stolt and Benson, 1986; Sava et al., 2001). In an approximate sense, this imaging Jacobian is equivalent to the cascaded operators $\underline{\mathbf{L}}'\underline{\mathbf{L}}$ in equation (2.1.5) without the data weighting operator $\underline{\mathbf{W}}^T\underline{\mathbf{W}}$. To see this, it is assumed that the velocity field is laterally invariant for the entire area between the reference datum $z_0$ and the target reflector location $z$: [2]

$$R_{MIG}(\mathbf{k}_m, z, \mathbf{p}_h; \phi, \alpha) = \int d\omega \mathcal{A}' e^{i \int_{z_0}^{z} k_z dz'} \Psi(\mathbf{k}_m, \mathbf{k}_h, z_0, \omega). \tag{2.2.15}$$

It is useful to formulate equation (2.2.15) as a function of constant offset slowness $\mathbf{p}_h$. This is achieved by reversing the order of the RTT operator $\mathcal{A}'$ with the propagation operator for a constant $\mathbf{p}_h$, which is equivalent to migration in the $\tau - p$ domain (Ottolini and Claerbout, 1984). [3] Hence, one can dispense with the radial trace transform and write the migration formula, including the data $\Psi$, as a function of $\mathbf{p}_h$:

$$R_{MIG}(\mathbf{k}_m, z, \mathbf{p}_h; \phi, \alpha) = \int d\omega e^{i \int_{z_0}^{z} k_z|_{\mathbf{p}_h} dz} \Psi(\mathbf{k}_m, \mathbf{p}_h, z_0, \omega), \tag{2.2.16}$$

The same logic is applied to the modelling formula. Concatenating constant ray parameter modelling and migration according to $\underline{\mathbf{L}}'\underline{\mathbf{L}}|_{\mathbf{p}_h}$ leads to:

$$R_{MIG}(\mathbf{k}_m, z, \mathbf{p}_h; \phi, \alpha) = \int d\omega \int dz' e^{i \int_{z}^{z'} k_z|_{\mathbf{p}_h} dz''} R(\mathbf{k}_m, z', \mathbf{p}_h; \phi, \alpha). \tag{2.2.17}$$

The phase term is rapidly oscillating for all $\omega$ except when $z = z'$ (Stolt and Benson, 1986). Hence, the velocity around the target is taken as constant leading to:

$$R_{MIG}(\mathbf{k}_m, z, \mathbf{p}_h; \phi, \alpha) = \int d\omega e^{-ik_z|_{\mathbf{p}_h} z} \int dz' e^{ik_z|_{\mathbf{p}_h} z'} R(\mathbf{k}_m, z', \mathbf{p}_h; \phi, \alpha). \tag{2.2.18}$$

A change of variables from $\omega$ to $z$ yields:

$$R_{MIG}(\mathbf{k}_m, z, \mathbf{p}_h; \phi, \alpha) = \int dk_z e^{-ik_z|_{\mathbf{p}_h} z} \left.\frac{d\omega}{dk_z}\right|_{\mathbf{p}_h} \int dz' e^{ik_z|_{\mathbf{p}_h} z'} R(\mathbf{k}_m, z', \mathbf{p}_h; \phi, \alpha). \tag{2.2.19}$$

Consequently,

$$R_{MIG}(\mathbf{k}_m, k_z, \mathbf{p}_h; \phi, \alpha) = \left.\frac{d\omega}{dk_z}\right|_{\mathbf{p}_h} R(\mathbf{k}_m, k_z, \mathbf{p}_h; \phi, \alpha). \tag{2.2.20}$$

---

[2]This assumption is less restrictive than it first appears, since, within the limits of one-way wave propagation, one can always datum the seismic wavefield through the complex overburden to a new reference plane $z_0$ close to the target reflector.

[3]The RTT and the DSR propagator do not commute for arbitrary velocities.

In the vertical wavenumber domain the action of applying $\underset{\sim}{\mathbf{L}}'\underset{\sim}{\mathbf{L}}|_{\mathbf{p}_h}$ is equivalent to applying the imaging Jacobian $\mathcal{J} = \frac{d\omega}{dk_z}|_{\mathbf{p}_h}$. This suggests that (locally) pre-multiplying the downward continued wavefield with the inverse of the (diagonal) Jacobian $\mathcal{J}^{-1}$ annihilates the amplitude distortion induced by the change from data to model space (Sava et al., 2001). Given in its recursive form, the amplitude scaled migration algorithm follows:

$$\Psi(\mathbf{m}, \mathbf{h}, z_i, \omega) = \mathcal{P}^{(SR)'}(z_i, z_{i-1})\Psi(\mathbf{m}, \mathbf{h}, z_{i-1}, \omega), \tag{2.2.21}$$

and

$$R(\mathbf{m}, z_i, \mathbf{p}_h; \phi, \alpha) \approx \mathcal{F}^{-1}_{\mathbf{k}_m} \int d\omega \mathcal{J}^{-1} \mathcal{A}' \mathcal{F}_{\mathbf{m}} \mathcal{F}_{\mathbf{h}} \Psi(\mathbf{m}, \mathbf{h}, z_i, \omega). \tag{2.2.22}$$

The explicit expression for the Jacobian can be found in Appendix D. The imaging Jacobian is indeed helpful to retrieve the correct angle dependence as demonstrated in Chapter 3.

### 2.2.2 Illumination operator

Duquet et al. (2000) follow a different strategy to improve the migration operator $\underset{\sim}{\mathbf{L}}'$. Their technique involves an approximation of the cascaded operator $\underset{\sim}{\mathbf{L}}'\underset{\sim}{\mathbf{W}}^T\underset{\sim}{\mathbf{W}}\underset{\sim}{\mathbf{L}}$, including the data weighting operator. They aim at compensating for illumination issues generated by the acquisition geometry (acquisition footprint) and the velocity field structure (wavefield focusing/defocusing effects). To this end, the simplified, reflection angle independent subsurface parameterization is adopted. Duquet et al. (2000) compute the diagonal of the chained operator $\underset{\sim}{\mathbf{L}}'\underset{\sim}{\mathbf{W}}^T\underset{\sim}{\mathbf{W}}\underset{\sim}{\mathbf{L}}$ by means of ray tracing (Appendix A). Ideally, application of the inverse of the diagonal operator should balance the subsurface illumination. A similar, propagator-based, approach can be followed using the separate offset formula in equation (1.3.46) (Kuehl and Sacchi, 2001a). However, as opposed to the ray tracing technique of Duquet et al. (2000) the restriction to laterally invariant media applies. Consider the (angle independent) model space $\delta$-function:

$$\mathbf{f}_{\mathbf{m}', z'} \equiv R(\mathbf{m}', z') = \delta(\mathbf{m} - \mathbf{m}')\delta(z - z'). \tag{2.2.23}$$

Applying the cascaded operators $\underset{\sim}{\mathbf{L}}'\underset{\sim}{\mathbf{W}}^T\underset{\sim}{\mathbf{W}}\underset{\sim}{\mathbf{L}}$ to the unit impulse model function (2.2.23) yields the corresponding 'diagonal element'. The modelling operator impulse response

is:

$$\Psi_\delta(\mathbf{m}, \mathbf{h}, z_0, \omega) = \underset{\sim}{\mathbf{W}} \mathcal{F}_{\mathbf{k}_m}^{-1} \left\{ \alpha(\mathbf{k}_m, \mathbf{h}, z_0, z', \omega) e^{-i\mathbf{k}_m \cdot \mathbf{m}'} \right\}, \tag{2.2.24}$$

where $\underset{\sim}{\mathbf{W}}$ is the weighting operator containing the binning information. The application of the adjoint migration operator to the impulse response $\Psi_\delta$ yields at the image point location $(\mathbf{m}', z')$:

$$\tilde{\mathbf{f}}_{\mathbf{m}',z'} = \mathcal{F}_{\mathbf{k}_m}^{-1} \int d\omega \left\{ \mathcal{F}_{\mathbf{m}} \left\{ \underset{\sim}{\mathbf{W}}^T \Psi_\delta(\mathbf{m}, \mathbf{h}, z_0, \omega) \right\} \alpha'(\mathbf{k}_m, \mathbf{h}, z', z_0, \omega) \right\}, \tag{2.2.25}$$

where the inverse midpoint Fourier transform is understood to be evaluated for $\mathbf{m}'$. The quantity $\tilde{\mathbf{f}}_{\mathbf{m}',z'}$ measures the scattered wavefield energy that is successfully recorded and subsequently imaged at its origin as a function of offset $\mathbf{h}$. In other words, $\tilde{\mathbf{f}}_{\mathbf{m}',z'}$ is a subsurface illumination function/map that is sensitive to both acquisition footprint and wavefield focusing/defocusing effects. The adjoint phase term $\alpha'$ is conveniently obtained from $\alpha$ by a simple sign change. The formula (2.2.25) is computationally expensive. However, it becomes manageable if only a few frequencies are considered. When $\underset{\sim}{\mathbf{W}}$ is the identity the innermost midpoint Fourier transform pair disappears. The cost of computing the formula (2.2.25) is then similar to two pre-stack migrations. Finally, applying the inverse of $\tilde{\mathbf{f}}_{\mathbf{m}',z'}$ to all subsurface points of the migrated image compensates for the aforementioned effects, since $\tilde{\mathbf{f}}_{\mathbf{m}',z'} = \mathrm{diag}\left\{ \underset{\sim}{\mathbf{L}}' \underset{\sim}{\mathbf{W}}^T \underset{\sim}{\mathbf{W}} \underset{\sim}{\mathbf{L}} \right\} \approx \underset{\sim}{\mathbf{L}}' \underset{\sim}{\mathbf{W}}^T \underset{\sim}{\mathbf{W}} \underset{\sim}{\mathbf{L}}$. However, the usefulness of equation (2.2.25) is very limited because of its restriction to laterally invariant media. In practice, illumination issues arise in media with a complex velocity structure. Hence, as it stands, ray tracing is the method of choice for the computation of illumination maps. A 2-D example for equation (2.2.25) can be found in Chapter 3.

## 2.3 Constrained least-squares migration/inversion

Instead of trying to find approximations to the least-squares solution, numerical optimization techniques offer the possibility to minimize the objective function (2.1.4) iteratively. Better yet, numerical minimization allows to incorporate regularization strategies that help to improve the robustness of the inversion. It turns out that a costly minimization of the standard least-squares objective function (2.1.4) holds relatively little advantage over (amplitude scaled) migration in equation (2.2.22) unless significant illumination issues due to a varying midpoint fold plague the inversion (Kuehl and Sacchi, 2001b). On the other hand, the performance and robustness of least-squares migration for AVP/AVA inversion can be significantly enhanced by model space regularization (Kuehl and Sacchi, 2002). A model smoothness constraint penalizes roughness (i.e., discontinuities and rapid amplitude changes) in the ray parameter dependent CIGs:

$$\min \ F(\mathbf{f}) = \|\mathbf{W}(\mathbf{d} - \mathbf{L}\mathbf{f})\|^2 + \lambda^2 \|\mathbf{D}\mathbf{f}\|^2, \tag{2.3.1}$$

where $\mathbf{D} \equiv \partial_{p_h}^n$ is the n-th order radial derivative in the $(p_{hx}, p_{hy})$ plane. [4] The idea is that roughness is caused by imaging artifacts and acquisition footprint noise, not AVA effects. The derivative operator acts as a low-pass filter that suppresses undesired ray parameter fluctuations. In this thesis only first order derivatives have been used. Effectively, the regularization imposes a similarity constraint on neighboring constant ray parameter sections. It is noted that Duquet et al. (2000) followed a similar strategy to suppress kinematic artifacts in constant offset Kichhoff migration. The tradeoff parameter $\lambda^2$ determines the weight of the roughness penalty term in equation (2.3.1). With the ray parameter sampling interval $\Delta p_h = \sqrt{\Delta p_{hx}^2 + \Delta p_{hy}^2}$ the product $\gamma = \lambda^2 \times \Delta p_h$ controls the amount of smoothing.

Iterative gradient minimization by conjugate gradients (CG) (Hestenes and Stiefel, 1952; Scales, 1987) is an excellent tool for seismic inversion. CG minimization does not require any explicit matrix operator inversion and thus is suitable for an operator application 'on the fly'. It avoids forming the product $\mathbf{L}'\mathbf{W}^T\mathbf{W}\mathbf{L}$. This is a crucial feature, since migration and modelling operators are coded as functions rather than matrices.

---

[4]In a 3-D implementation azimuthal smoothness could be imposed as well.

Moreover, CG minimization converges faster than the more conventional steepest descent technique (Strang, 1986). A CG recipe for least-squares inversion (CGLS) reads as follows (Scales, 1987):

Choose the starting model $\mathbf{f}_0$ to be zero. Put the data auxiliary vector $\mathbf{s}$ equal to the binned seismic data: $\mathbf{s}_0 = \mathbf{d}$. The auxiliary model vectors $\mathbf{r}$ and $\mathbf{p}$ are initialized with the migration: $\mathbf{r}_0 = \mathbf{p}_0 = \underline{\mathbf{L}}'\mathbf{s}_0$, and the second auxiliary data vector $\mathbf{q}$ is set up with the modelled (de-migrated) data: $\mathbf{q}_0 = \underline{\mathbf{L}}\mathbf{p}_0$. Then for $i = 0, 1, 2, \ldots$:

$$
\begin{aligned}
\alpha_{i+1} &= \frac{\mathbf{r}_i \cdot \mathbf{r}_i}{\mathbf{q}_i \cdot \mathbf{q}_i} \\
\mathbf{f}_{i+1} &= \mathbf{f}_i + \alpha_{i+1}\mathbf{p}_i \\
\mathbf{s}_{i+1} &= \mathbf{s}_i - \alpha_{i+1}\mathbf{q}_i \\
\mathbf{r}_{i+1} &= \underline{\mathbf{L}}'\mathbf{s}_{i+1} \\
\beta_{i+1} &= \frac{\mathbf{r}_{i+1} \cdot \mathbf{r}_{i+1}}{\mathbf{r}_i \cdot \mathbf{r}_i} \\
\mathbf{p}_{i+1} &= \mathbf{r}_{i+1} + \beta_{i+1}\mathbf{p}_i \\
\mathbf{q}_{i+1} &= \underline{\mathbf{L}}\mathbf{p}_{i+1},
\end{aligned}
\tag{2.3.2}
$$

where $\underline{\mathbf{L}}$ and $\underline{\mathbf{L}}'$ are the modelling and migration operator, respectively, in the temporal frequency domain.

The iterative process can be stopped and resumed at any stage. Additional model and data space operators are incorporated by augmenting the operators $\underline{\mathbf{L}}$ and $\underline{\mathbf{L}}'$ appropriately. For instance, to minimize the regularized cost function (2.3.1) the following augmentation retains the algorithmic structure of CGLS (Scales, 1987):

$$
\underline{\mathbf{L}} \equiv \begin{pmatrix} \mathbf{W}\underline{\mathbf{L}} \\ \lambda\underline{\mathbf{D}} \end{pmatrix} \quad \text{and} \quad \mathbf{d} \equiv \begin{pmatrix} \mathbf{W}\mathbf{d} \\ \mathbf{0} \end{pmatrix}.
\tag{2.3.3}
$$

Most commonly, model space regularization means either damping, in which case $\underline{\mathbf{D}}$ is diagonal or finite-difference smoothing, in which case $\underline{\mathbf{D}}$ is banded. It is important that the (augmented) operators $\underline{\mathbf{L}}'$ and $\underline{\mathbf{L}}$ are indeed an adjoint operator pair. To test this property Claerbout (1992) proposed the so-called 'dot-product test'. The numerical operator implementations have to satisfy:

$$
\mathbf{d} \cdot \tilde{\mathbf{d}} = \mathbf{f} \cdot \tilde{\mathbf{f}},
\tag{2.3.4}
$$

for any vectors $\mathbf{f}$ and $\mathbf{d}$, where $\tilde{\mathbf{d}} = \underset{\sim}{\mathbf{L}}\mathbf{f}$ and $\tilde{\mathbf{f}} = \underset{\sim}{\mathbf{L}}'\mathbf{d}$. The input vectors $\mathbf{f}$ and $\mathbf{d}$ define the model and data space, respectively. They are loaded with random numbers. For properly coded operator pairs $\underset{\sim}{\mathbf{L}}$ and $\underset{\sim}{\mathbf{L}}'$ the 'dot-product test' should be satisfied down to the least significant digit.

Constrained least-squares migration for AVP/AVA inversion based on equation (2.3.1) is exemplified and extensively tested with numerous examples in Chapter 3. Chapter four presents a real-world data example.

# Chapter 3

# Synthetic data examples

This chapter covers both conventional migration and least-squares migration examples that illustrate and test the theory outlined in the previous parts of the thesis. Synthetic data tests are valuable to gain insight into the performance of imaging/inversion algorithms. However, the tests have to be interpreted with care. It is important that the synthetic data are generated by a more general operator than the one the inversion operator is originally based on. The full acoustic wave-equation, the starting point in Chapter 1, is certainly a good choice for forward modelling. Full wave-equation finite difference modelling is well developed and yields data that, when carefully implemented, contain the relevant physics and few numerical artifacts (Clayton and Engquist, 1990; Press et al., 1997). Effects that are absent from the synthetic acoustic 2-D finite difference data include: surface multiples, absorption, anisotropy, out-of-plane reflections, mode conversions etc., all of which can potentially obscure the test results. For low contrast, layered media faster ray-tracing modelling can replace the computing intensive finite-difference approach. If a migration/inversion method fails to perform well under these 'clinical' conditions, there is no hope it can succeed when applied to real-world data.

## 3.1   Migration

As amply discussed, the goal of migration is less ambitious than that of inversion. However, migration is the nucleus of inversion, since accurate propagation is a prerequisite for successful inversion. It is therefore instructive to examine the structural imaging capabilities of migration operators. In structural imaging the 'stacked' migrated section is
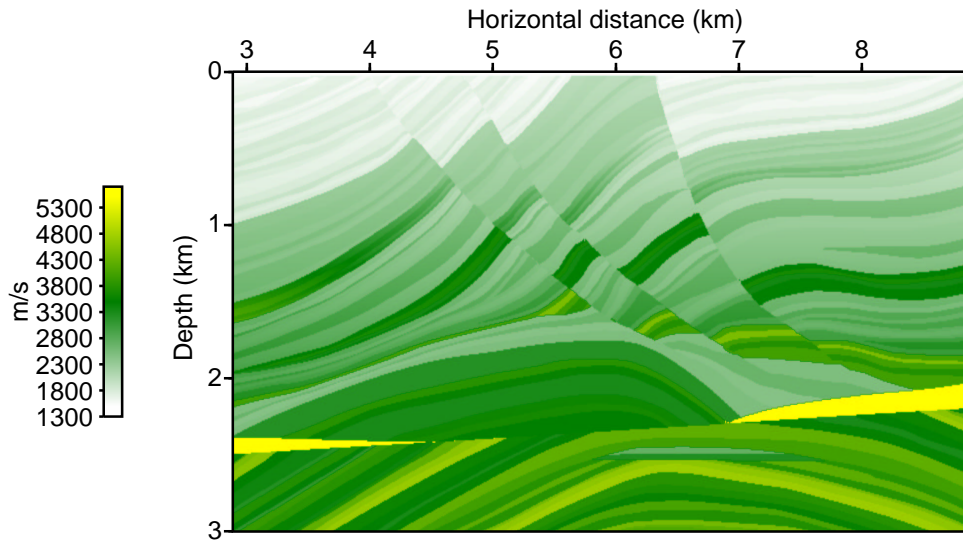
Figure 3.1: The Marmousi compressional velocity field. The velocities range from $1500$ to $5500$ m/s. The Marmousi model is structurally complex, with many thin layers broken by several major faults and an unconformity surface. The folded carbonate sedimentation series at about $2.5$ km forms the structural hydrocarbon trap.

of interest. Stacking is the summation of the CIGs along offset ray parameter. This is equivalent to applying the simplified imaging operator $\int d\mathbf{k}_h \int d\omega$ to the local wavefield. Stacking enhances the signal-to-noise ratio, suppresses imaging artifacts and multiples and thus improves the image quality in general. Obviously, one is deprived of this powerful tool in (least-squares) migration for AVP/AVA inversion.

The first two sections introduce generic synthetic datasets that have become quasi standards for the testing of imaging algorithms. The first dataset is based on the so-called 2-D Marmousi model. The Marmousi dataset is well suited for the testing of both structural imaging and AVP/AVA inversion (Section 3.2.2). The second 2-D dataset is derived from the 3-D SEG/EAGE salt model. The salt model is a challenge to imaging algorithms due to its strong velocity contrasts. It is a very good example to demonstrate the superior performance of the split-step PSPI over the split-step propagator but its model parameterization makes it less useful for assessing AVP/AVA inversion methods.
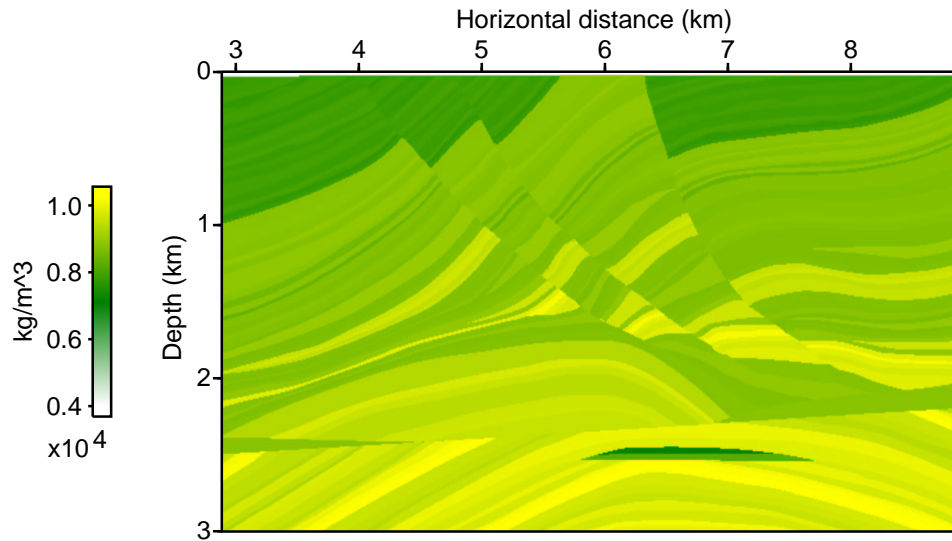
Figure 3.2: The Marmousi density field. The Marmousi dataset is based on a variable-velocity and density model making it well suited for acoustic AVP/AVA studies (see Section 3.2.2).

### 3.1.1 The Marmousi model

The Marmousi model is based on a geological cross section through the North Quenguela Trough in the Cuanza Basin in Angola (Versteeg, 1994). The dataset consists of 240 'single-cable marine shot records' acquired using acoustic finite-difference modelling, with variations in both acoustic velocity and density (Figure 3.1 and Figure 3.2). Details regarding the data generation can be found in Versteeg (1994). The model was generated by the French Petroleum Institute, and was released to the public for the purpose of testing migration and velocity estimation techniques.

Versteeg (1994) describes the geologic background of the Marmousi model. In summary, the geologic history underlying the model consists of two distinct phases. The first phase is marked by a continuous sedimentation of marls and carbonates. These deposits were folded and then eroded with the erosion surface being flat. The resulting anticlinal structure forms the hydrocarbon trap. The second phase began with the deposition of an isopachous saliferous evaporitic series. On this series a clayey-marly series and later shaly-sandy detrital sediments were deposited. These sediments are strongly affected by normal growth faults caused by lateral salt creep due to the overburden pressure.
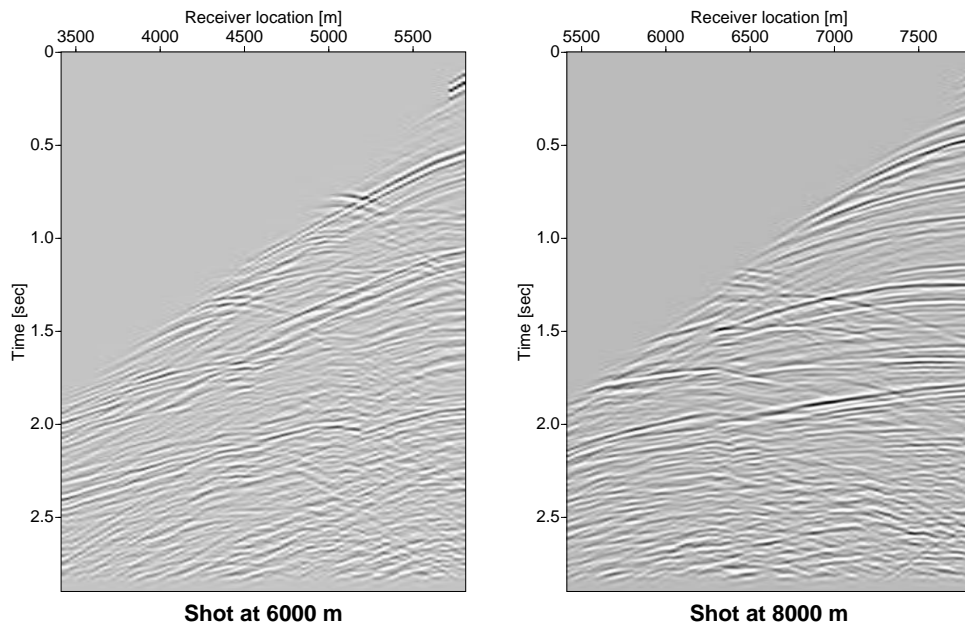
Figure 3.3: Two shots of a total of 240 shot records. The distance between two consecutive receivers is 25 m with a total of 96 traces per shot. Initial offset is 200 m and maximum offset is 2575 m . The data were filtered with a trapezoid frequency filter with $(0, 10, 35, 55)$ Hz. The line was 'shot' in an end-on configuration from west to east (left to right in Figure 3.1). Distance between shots is 25 m. The direct arrival and refracted waves have been muted.

The high velocity wedges seen in Figure 3.1 are remnants of this process. The Marmousi model is structurally complex, with many very thin layers, which makes for very realistic synthetic data. Two example shots in Figure 3.3 illustrate the data complexity. Even when the correct velocity model is used, many imaging methods cannot completely image the hydrocarbon trap (Gray and May, 1994).

The split-step DSR propagator proves sufficiently accurate to produce a very good image of the Marmousi model. The migration code has been implemented on an SGI Origin 2400 shared-memory parallel computer (400-MHz processors). The algorithm's parallelization is done with respect to the temporal frequencies. More details on the computational aspects of the pre-stack migration are discussed in Chapter 5. The migration used every second midpoint of the original midpoint-offset sorted dataset. This results in a data cube of size $256 \times 64 \times 1024$ including zero padding for the Fourier/Hartley transforms (see also Chapter 5). The migration was performed for a frequency band of 5
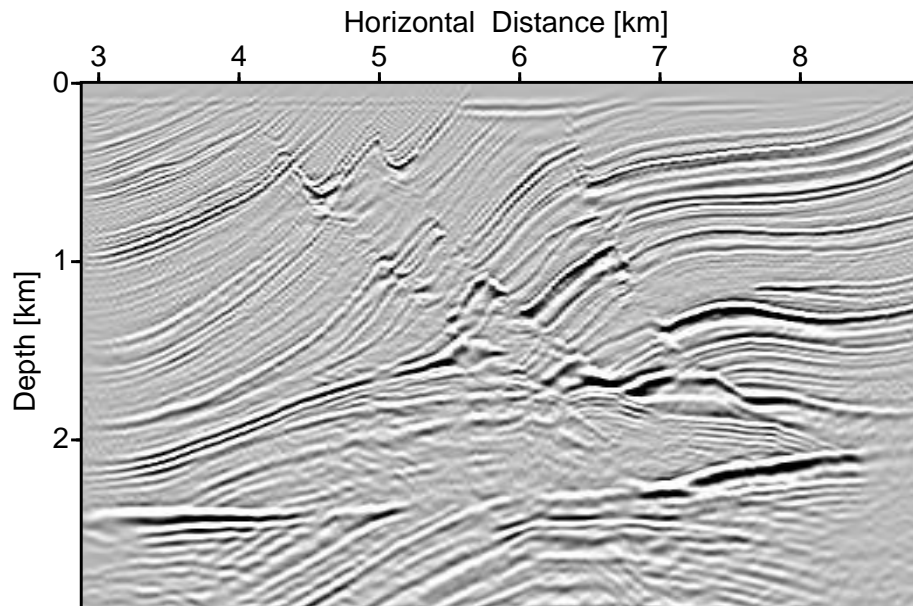
Figure 3.4: The split-step DSR migrated Marmousi data. The split-step approximation yields a very good Marmousi image despite the structural complexity of the model. The hydrocarbon trap is clearly delineated.

to 60 Hz and took about one minute on 32 processors. A fast computational turnaround is critical when least-squares migration/inversion is to be carried out. Figure 3.4 shows the very good imaging result.

### 3.1.2 The SEG/EAGE salt model

For the purpose of a comparative propagator test, the SEG/EAGE salt model is introduced (Aminzadeh et al., 1994). As mentioned earlier, the SEG/EAGE model serves solely as a test for structural imaging. The salt model assumes a constant density limiting its usefulness for AVP/AVA studies. More importantly, most reflectors are represented in a 'spiky' rather than a 'blocky' fashion making these reflectors unsuitable for AVP/AVA inversion. Figure 3.5 gives an overview over the 3-D velocity field and its embedded geologic structures. The model was designed to address 3-D imaging issues in a typical Gulf of Mexico setting. At this stage, 3-D implementations of the (least-squares) migration algorithm or approximations thereof have not been considered (Biondo and Palacharla, 1996). The shown examples are based on a 2-D profile running through the
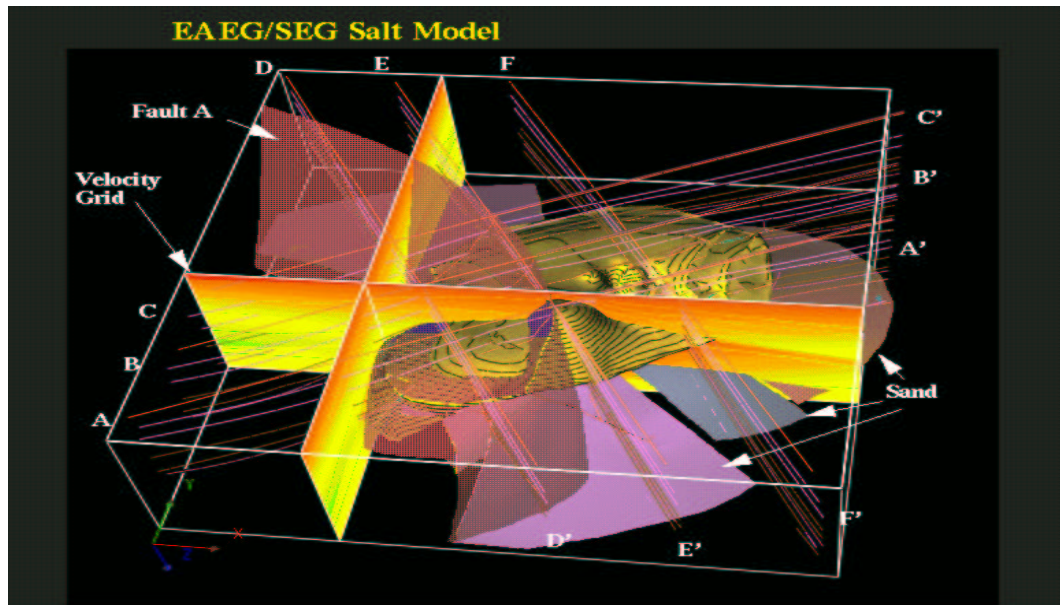
Figure 3.5: 3-D perspective of the EAGE/SEG salt model (Aminzadeh et al., 1994) with the salt sill, different faults, sand bodies and lenses. The overall model dimensions are $13.5 \times 13.5 \times 4.2$ km in the $x, y, z$ directions, respectively. The salt crest is at about $325$ m. The model has been designed in part to test various imaging algorithms in different geologic settings: salt flank, salt overhang and sub-salt. The velocities surrounding the salt body are typical of Gulf of Mexico sediments. Two velocity profiles are shown. Hot colors correspond to low velocities with red being the water velocity of $1500$ m/s. The velocity profile for the cross section A-A' is shown in Figure 3.6.

salt model (profile A-A' in Figure 3.5). The simulated data are purely 2-D in that they do not include 3-D propagation effects and out-of-plane reflections which is in theoretical agreement with the 2-D versions of the migration formulas derived in Chapter 2.

The first migration example involves zero-offset migration in equation (2.2.14). The conducted tests investigate the accuracy of split-step, split-step PSPI, and split-step NSPS extension of equation (2.2.14). The synthetic data in Figure 3.7 have been generated by 'exploding-reflector' modelling to assess the best-case capabilities of zero-offset/post-stack migration (O'Brien and Gray, 1996). Rather than the exact adjoint of the migration operator a full wave-equation version analogous to equation (1.3.47) calculated the up-going wavefield. Since the full wave-equation does not have any numerical propagation angle limitations, the occurring discrepancies between the migration and the model are attributed to inaccuracies of the employed migration propagator. O'Brien and Gray
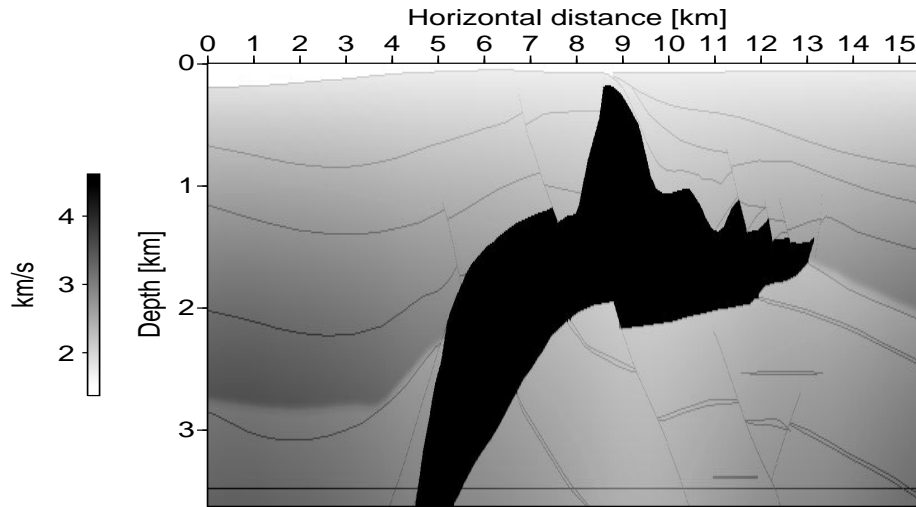
Figure 3.6: Velocity profile A-A′ from the SEG/EAGE salt model. The velocities range from 1500 m/s (water) to 4481 m/s (salt). Darker shades denote higher velocities. Notice the relatively lower velocities below the overpressure surface.
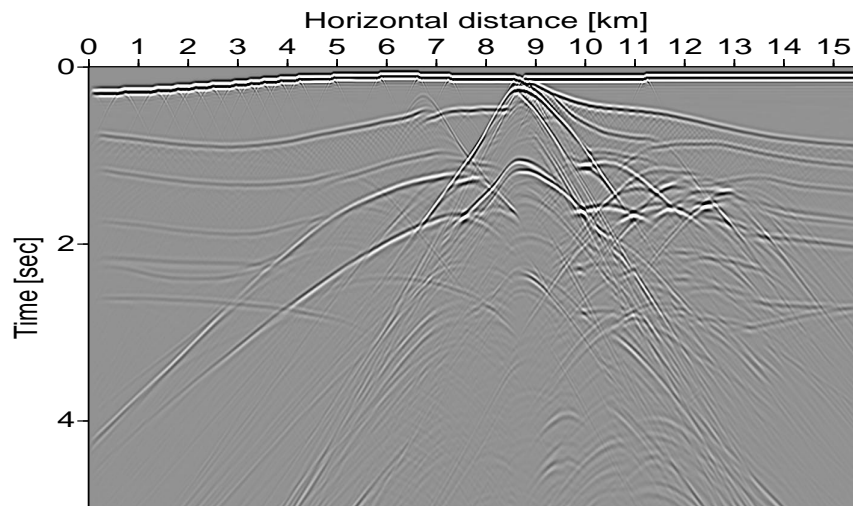


Figure 3.7: The 'exploding-reflector' dataset for the profile A-A′ of the SEG/EAGE salt model. The data approximately simulate a zero-offset seismic section. The dataset serves to assess the structural imaging capabilities of different zero-offset/post-stack migration algorithms. To achieve more realism one has to run full shot-record simulations (see also Figure 3.11).
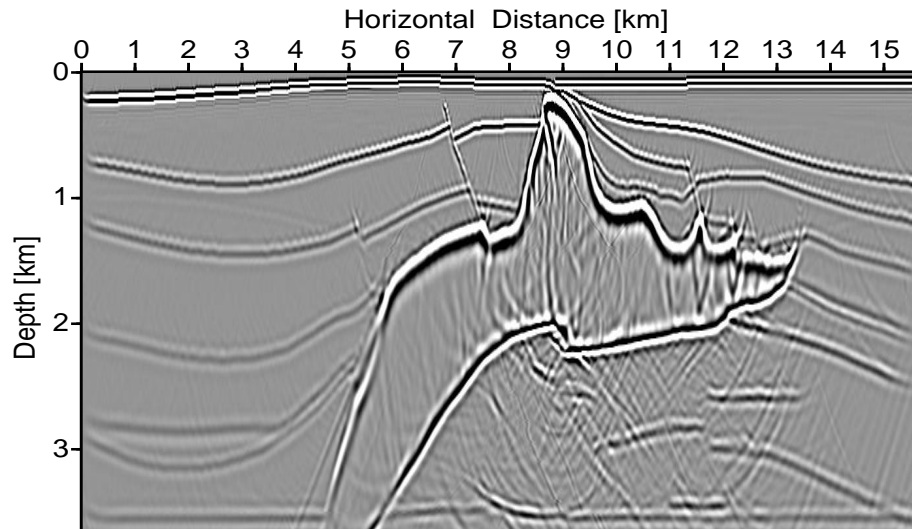
Figure 3.8: Split-step zero-offset migration of the 'exploding-reflector' data in Figure 3.7. There is a significant amount of artifacts in the sub-salt area.

(1996) conducted a similar study comparing wave-equation (i.e., propagator based imaging) versus Kirchhoff migration (i.e., ray theoretical imaging).

The split-step migrated 'exploding-reflector' data are shown in Figure 3.8. Obviously, the high velocity salt body presents a problem for the split-step technique. Given the ideal input data, the migration result is only fair. The artifacts in the sub-salt region are due to the insufficient wide-angle accuracy of the split-step approximation in the presence of high velocity contrasts (see also Figure 1.3). The zero-offset migration obtained with the split-step PSPI propagator is seen in Figure 3.9. Overall, the split-step PSPI migration produces a much better imaging result than the faster split-step migration. However, the split-step PSPI method shows slight deficiencies for the steep salt flank, and not all of the steep faults in the sub-salt zone are properly imaged. To select the velocities at each depth step, the adaptive algorithm described by Bagaini et al. (1995) has been employed, averaging 5.7 reference velocities per depth step in this example. For comparison, Figure 3.10 shows the result obtained with the split-step NSPS propagator. The images in Figure 3.9 and Figure 3.10 are nearly identical. The same reference velocities were used. Upon close inspection the split-step NSPS technique appears to have imaged
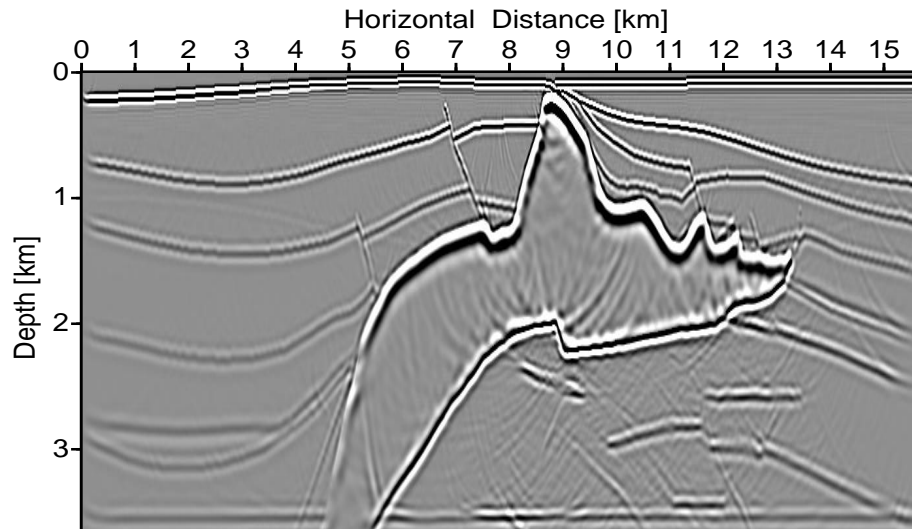
Figure 3.9: Split-step PSPI zero-offset migration of the 'exploding-reflector' data in Figure 3.7. The sub-salt area is cleaner and better imaged than in Figure 3.8.

the salt flank slightly better than the split-step PSPI algorithm, but the differences are subtle.

An additional level of realism is added to the tests by generating finite-difference shot records across the model. Because surface sources are used in the shot modelling, there is no guarantee that all reflection points will be illuminated as effectively as they were when modelled by exploding reflectors (O'Brien and Gray, 1996). In addition, internal multiple reflections are now included in the data. Surface related multiples are not present because of an absorbing surface boundary condition. Figure 3.11 is the zero-offset data extracted from the full shot records. A comparison between Figure 3.7 and Figure 3.11 indicates that the more 'true-to-life' zero-offset section could pose challenging data quality problems. Not all events seen in the 'exploding-reflector' data are equally well represented in the zero-offset data. The sub-salt image produced by split-step DSR migration is illustrated in Figure 3.12. The superimposed lines indicate reflectors to be imaged. The split-step PSPI DSR migration in Figure 3.13 benefits from the multi-reference velocity approach. The reflectors are better imaged and phase inconsistencies present in the split-step migration have been largely resolved.
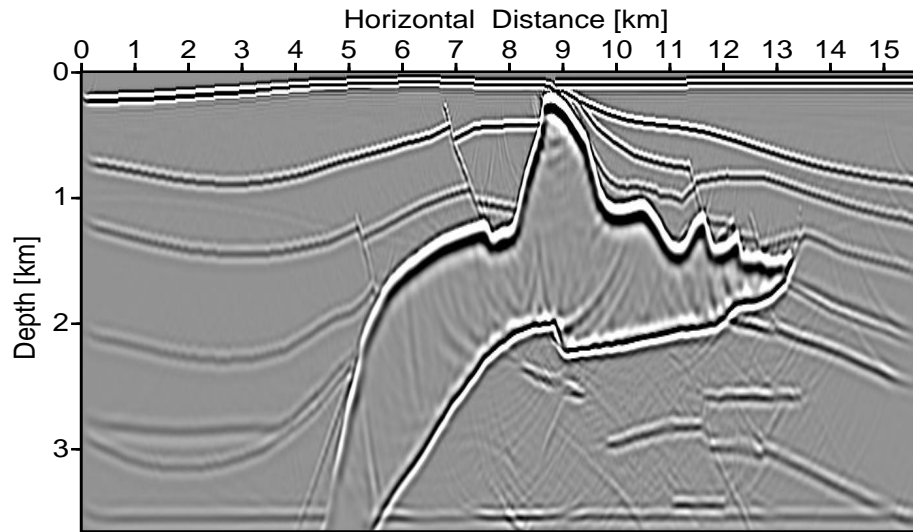
Figure 3.10: Split-step NSPS zero-offset migration of the 'exploding-reflector' data in Figure 3.7. The image is nearly identical to the split-step PSPI result in Figure 3.9. The split-step NSPS technique has produced a slightly better image of the steep salt flank than split-step PSPI.
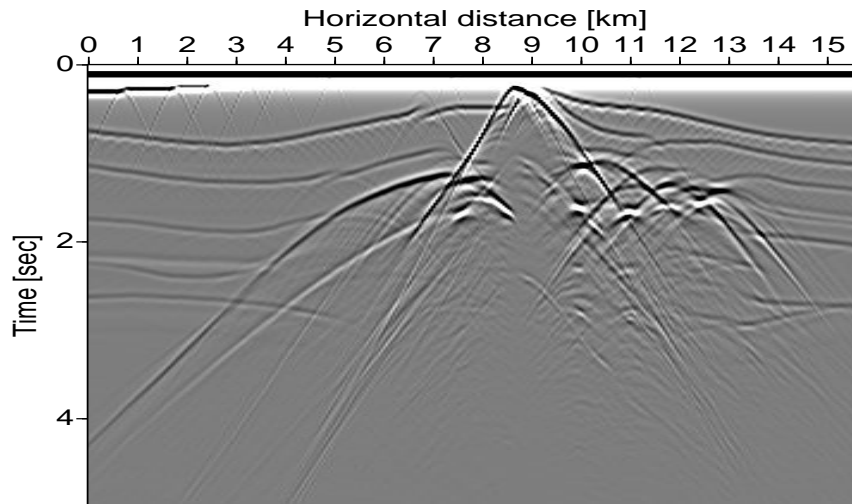


Figure 3.11: The zero-offset traces for the profile A-A' of the SEG/EAGE salt model. The data were acquired using finite-difference simulations. Only the zero-offset traces are shown. The migration examples in Figures 3.12 and 3.13 use the corresponding offset data.

69
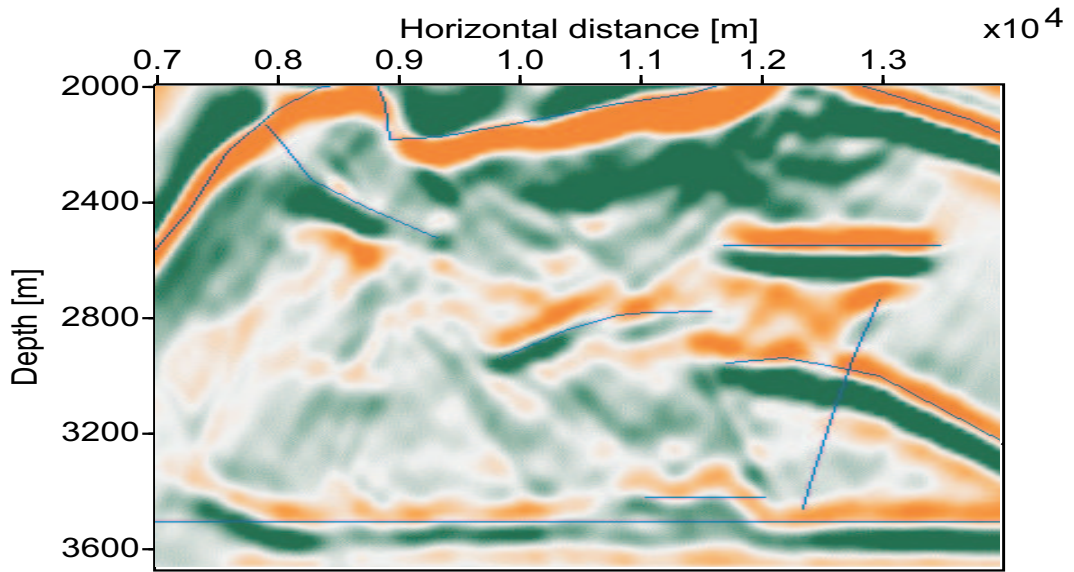
Figure 3.12: Sub-salt image of the split-step DSR migrated dataset for the profile A-A' of the SEG/EAGE salt model. The superimposed lines indicate some of the reflectors of the sub-salt area. The migration used a total of 323 midpoints with offsets ranging from 0 to 2097 m.
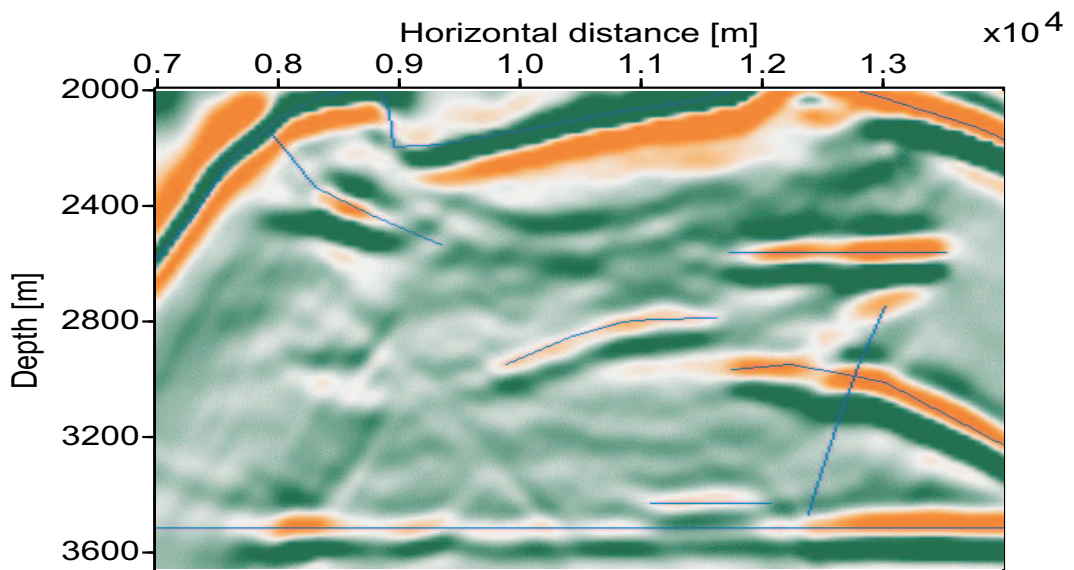


Figure 3.13: Sub-salt image of the split-step PSPI DSR migrated dataset for the profile A-A' of the SEG/EAGE salt model. Compare this figure to Figure 3.12. The split-step PSPI algorithm handles the large velocity contrast better. The imaged reflectors match the true model more closely. Notice the improved phase consistency.

## 3.2 Least-squares migration

The following least-squares migration examples fall roughly into two categories:

- (post- and pre-stack) least-squares migration using reflection angle independent operators, and

- reflection angle dependent least-squares migration for AVP/AVA inversion.

The lack of compelling advantages of the first category over conventional migration provides the incentive for studying the latter, modelling/migration that considers angle/ray parameter dependent CIGs. As it turns out, regularized least-squares migration for reflectivity inversion has the potential to perform considerably better than conventional migration.

### 3.2.1 Angle independent least-squares migration

This section deals exclusively with examples investigating reflection angle independent least-squares migration. That is to say, the generation of CIGs is not an option. The benefits of this rather simplistic approach are limited. Despite this somewhat pessimistic assertion, the experience gained from applying the various forms of least-squares migration makes it a worthwhile exercise. The perhaps more important findings are discussed in next section that is devoted to least-squares migration for AVP/AVA inversion.

The potentials and limitations of least-squares migration are assessed stepwise. When developing least-squares algorithms the first tests usually involve the application of the inversion algorithm to data modelled by the original forward operator itself. This is useful to confirm the correct implementation of the minimization algorithm. In addition, the 'adjointness' of the operator should always be confirmed with the 'dot-product test' (equation 2.3.4). Clearly, tests of this kind do not make any statement about the quality of the operators themselves.

The first example uses a simple bandlimited reflectivity model (Figure 3.14). The examined method is zero-offset least-squares migration using the split-step extended version of the operator pair in equation (1.3.47) and equation (2.2.14) (Kuehl and Sacchi, 1999). Reflection angle independent least-squares migration amounts to minimizing the
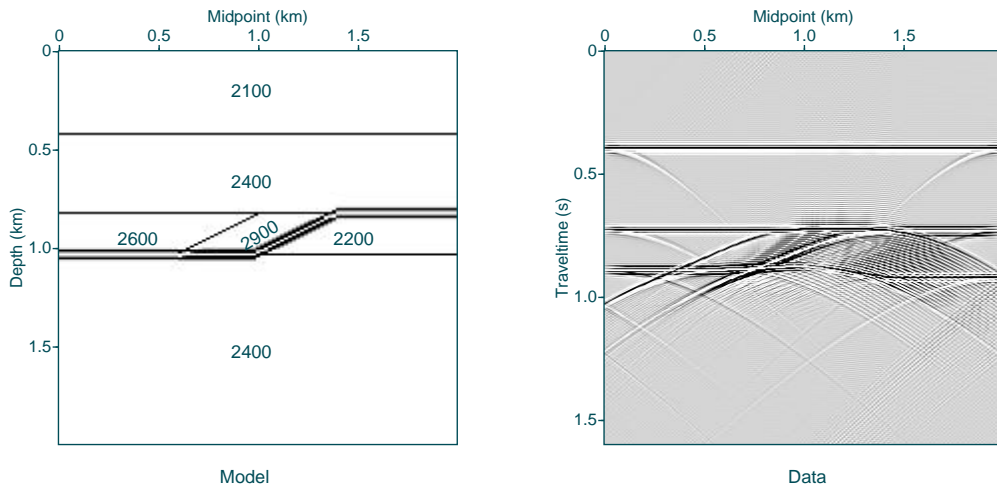
Figure 3.14: Left: A simple reflectivity model convolved with a Ricker wavelet. The interval velocities are in meters per second. Right: The zero-offset data generated by the forward split-step modelling operator.

objective function (2.1.4). The 'exploding-reflector' data in Figure 3.14, the presumed surface data, have been generated with the forward (angle independent) modelling operator. Noticeably, there are edge effects in the data. Any artifacts caused by the forward operator, and all intrinsic simplifications diminish the robustness of the inversion when applied to real-world data. Nonetheless, it is instructive to perform the inversion on the forward operator modelled data to assess the algorithm's performance under ideal conditions. The migration and the least-squares migration are depicted in Figure 3.15. Least-squares migration removes almost all of the spurious energy after 5 iterations of the CG algorithm (2.3.2). Only a few iterations are necessary to achieve convergence. The least-squares test is repeated for the reflection angle independent version of the split-step DSR operator (equations (1.3.51) and (2.2.9)). Figure 3.16 shows four modelled common-midpoint (CMP) gathers based on the reflectivity model in Figure 3.14 (left). Five iterations of the pre-stack least-squares algorithm suffice to obtain a fairly good result in terms of artifact reduction (Figure 3.17). Unfortunately, neither angle independent pre-stack nor post-stack least-squares migration prove to be a robust tool when applied to seismic data that were generated by a more general modelling technique (e.g., finite difference modelling). In other words, there is no guarantee that this somewhat 'naive'
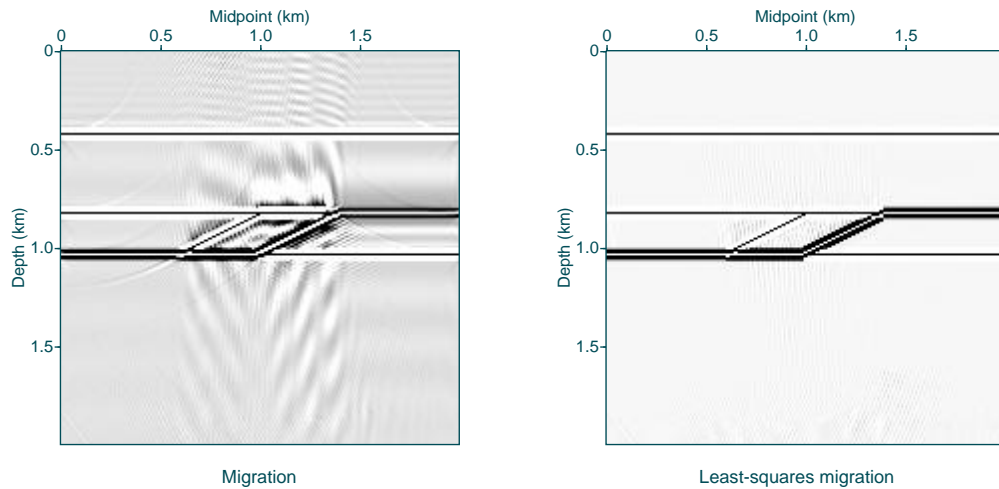
Figure 3.15: Left: The split-step migration using the data in Figure 3.14. The application of the adjoint operator causes residual artifacts. The image amplitudes have been clipped to emphasize the differences between the migration and the model in Figure 3.14 (left). Right: In the least-squares migrated image the artifacts are almost completely removed. The retrieved reflectivity is close to the true model after 5 iterations of the CG algorithm.

least-squares migration approach provides superior imaging when applied to well sampled real-world wavefield data (Nemeth et al., 1999). On the contrary, in the worst case, artifacts can result that otherwise would be absent from the conventionally migrated image. On the other hand, if the wavefield sampling is sub-optimal the data weighting operator in the objective function (2.1.4) takes effect and least-squares migration reveals some of its potential.

**Subsurface illumination**

The following examples are intended to demonstrate that least-squares migration can correctly balance the seismic amplitudes when the seismic wavefield is unevenly sampled. In particular, the illumination issue caused by a strongly varying midpoint fold is addressed. Figure 3.18 (top) shows the first five of a total of one hundred midpoint gathers obtained by Kirchhoff modelling (Bleistein et al., 2001). Figure 3.19 (top) is the split-step DSR migration of the complete data. The model consists of two types of reflectors, labelled as reflector *1* and *2*. Reflector *1* has about 70% of the reflection amplitude of reflector *2*. Despite finite survey line effects, this ratio is well preserved for the most

DSR data / midpoint-offset gathers
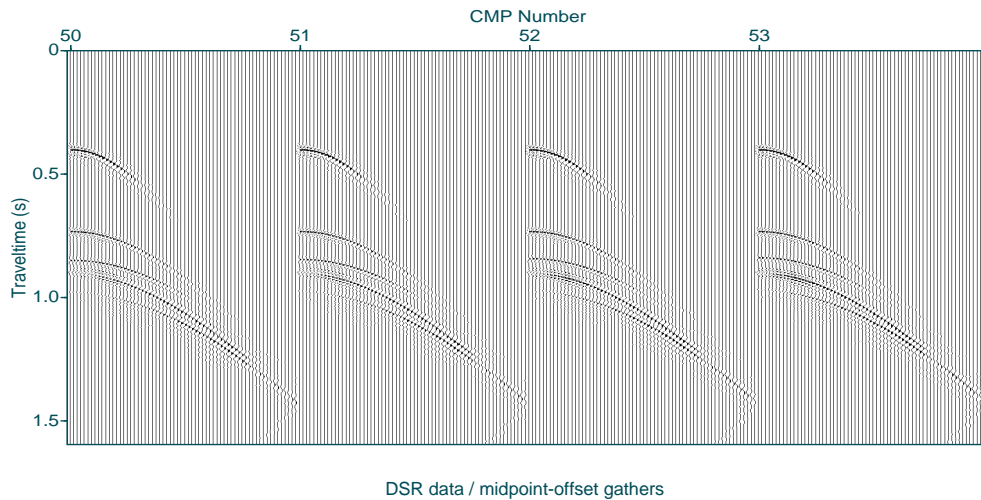
Figure 3.16: Four common midpoint (CMP) gathers modelled with the reflection angle independent split-step DSR operator.

part of the migrated section. Figure 3.18 (bottom) depicts the five midpoint gathers after having randomly removed 80% of the data in the first half of the midpoint gathers. This creates a severe illumination issue due to a strongly non-uniform midpoint fold distribution. The migration of the incomplete data (Figure 3.19) shows incorrect reflection strengths all across the section, plus some spurious artifacts. Large parts of the image are dimmed while the least-squares migration in Figure 3.19 (bottom) retrieves the reflectors after seven iterations with the correct amplitude ratio preserved. Figure 3.20 demonstrates that least-squares migration gives robust results also when random noise is added to the data. These examples are encouraging. However, it is also true that conventional migration in combination with an appropriate input data normalization is likely to produce comparable results. Zheng et al. (2001) investigate weighting strategies to remedy the effects of the acquisition footprint on Kirchhoff migrated gathers for AVA analysis. They tested different techniques with mixed results, area weighting (Canning and Gardner, 1998) being the most promising approach. In any case, if more forgiving structural imaging is the goal (i.e., the stacked seismic image) even a simple CMP fold normalization balances the subsurface illumination sufficiently well. This reflects the ambivalence of the stacking process. Stacking is tremendously healing for structural imaging but, at the same time, destroys valuable amplitude information. The angle independent
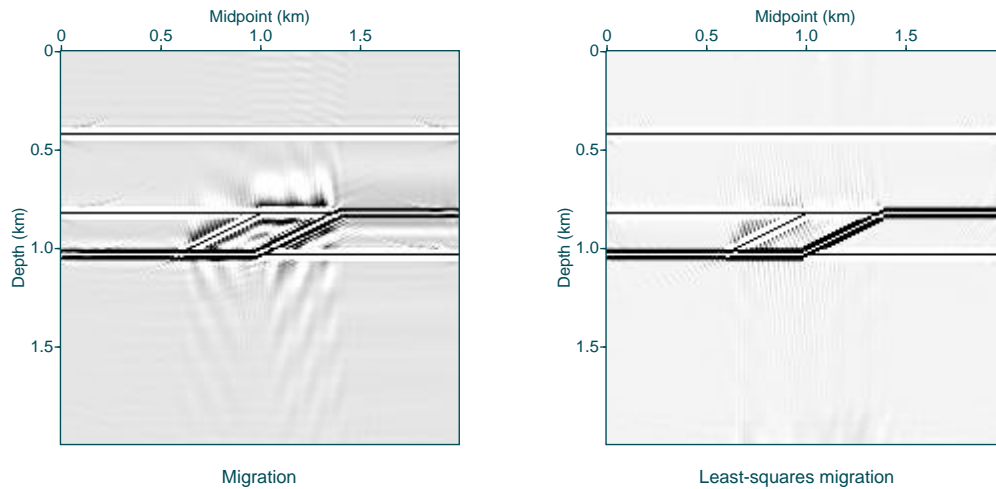
Figure 3.17: Left: The migrated pre-stack data from Figure 3.16. Right: The pre-stack least-squares migrated data after 5 iterations of the CG algorithm.

modelling/imaging operators do not offer the option to generate CIGs. Consequentially, least-squares migration is expected to have more relevance for reflection angle dependent migration/inversion than for structural imaging.

A different, data sampling independent, illumination issue arises in media where the velocity structure causes focusing and defocusing effects (e.g., shadow-zones). As an alternative to least-squares migration, the computation of the illumination operator can, then, help to scale the migrated section to compensate for these effects (Duquet et al., 2000; Rickett, 2001). Illumination compensation can be critical when seismic data are to be interpreted in terms of amplitude anomalies (e.g., bright/dim spots). A step towards this approach is discussed in Section 2.2.2. As it stands, the proposed technique in Section 2.2.2 is restricted to laterally invariant velocity fields and therefore is of very limited use.

In spite of this important caveat, a constant offset illumination map (h = 100 m) is shown in Figure 3.21 (top) for illustration. The underlying velocity field increases linearly with depth. As in the previous examples, the midpoint fold is varying with a reduction of about 80% for the first 50 CMPs. The dark shades in Figure 3.21 denote better illumination. The lateral variation in the illumination is obvious. Apart from that, the lack of depth penetration due to the small offset is apparent. The constant offsets illuminate a relatively narrow band centering around 0.2 km that soon peters out with

depth. As expected, for larger offsets (600 m) the deeper parts of the model become better illuminated (Figure 3.21 (middle)). When all offsets (0 to 600 m) are included illumination is dominated by the lateral variance due to the irregular midpoint fold (Figure 3.21 (bottom)).

Alternatively, Duquet et al. (2000) employed ray-tracing to calculate the illumination operator in arbitrary media. More recently, Rickett (2001) favored wavefield propagators for the same task. He took advantage of a conjecture by Claerbout and Nichols (1994) to normalize the migrated data. They observed that after consecutive modelling and migration of a reference image, the ratio between the reference image and the modelled/demigrated image will be a weighting function with the correct physical units. Rickett (2001) tested different reference images with partially promising results. Whether the propagator approach offers any real advantages over the ray-tracing based technique remains to be seen.
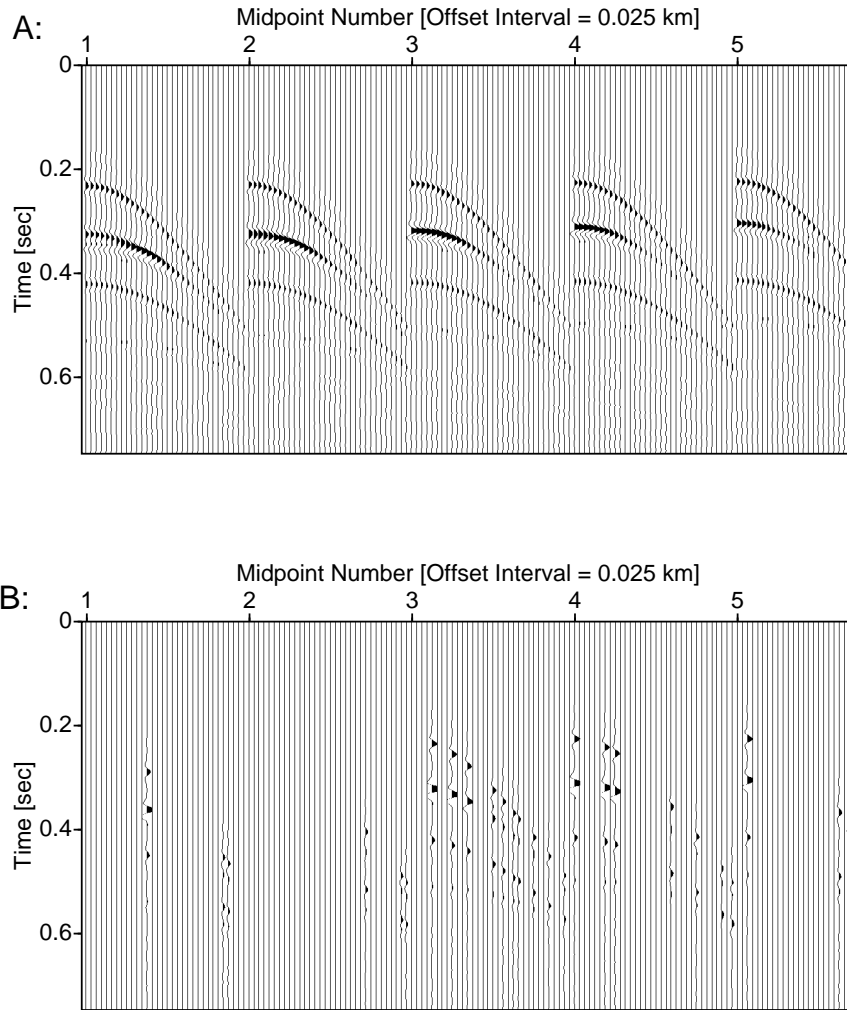
Figure 3.18: Top: The first five of one hundred midpoint gathers generated by a Kirchhoff modelling code. Bottom: The same midpoint gathers after randomly removing 80% of the data.
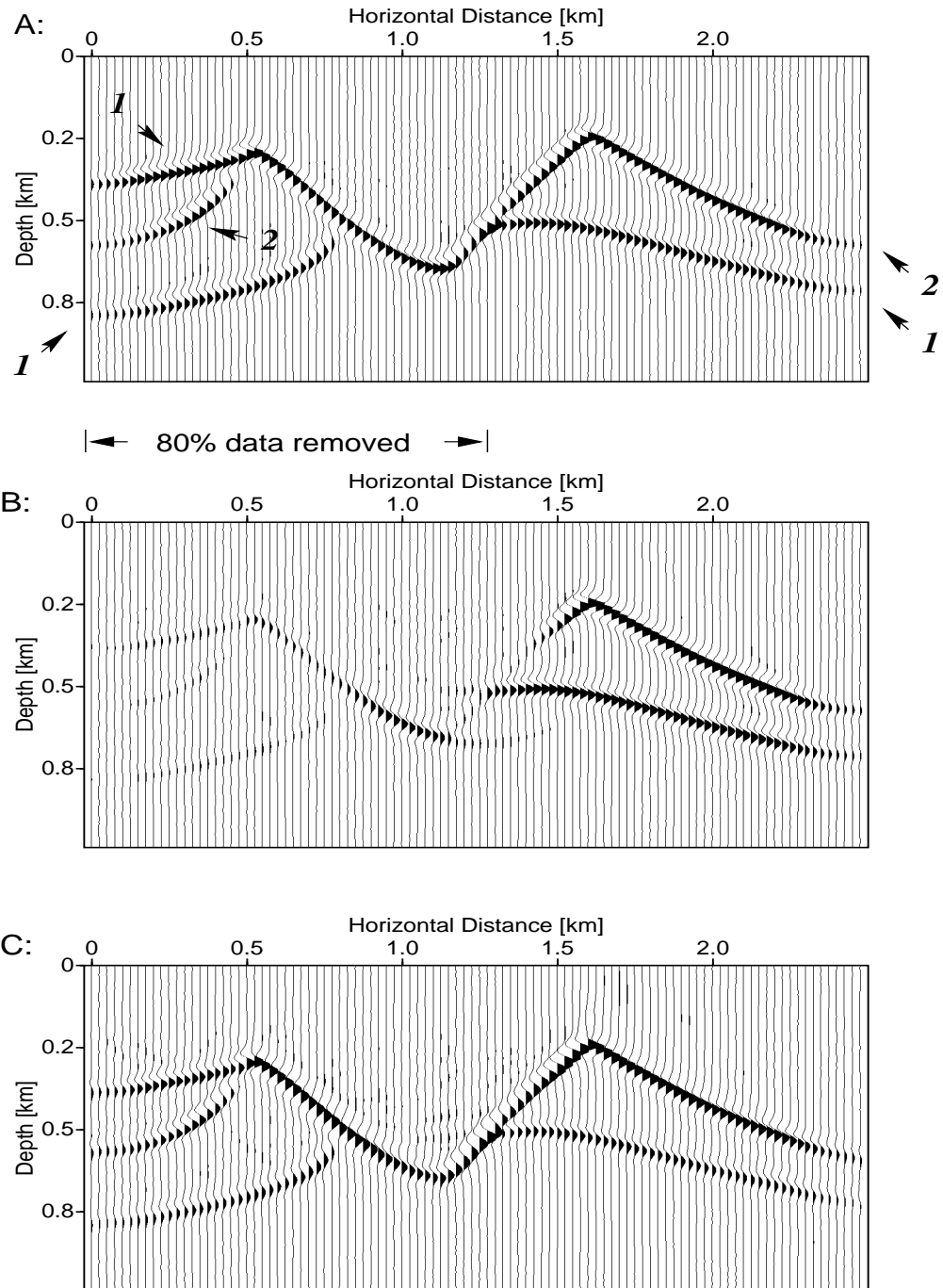
Figure 3.19: Top: Pre-stack migration of the complete dataset. Middle: Migration of the incomplete data. Bottom: Least-squares migration of the incomplete data (7 CG iterations).
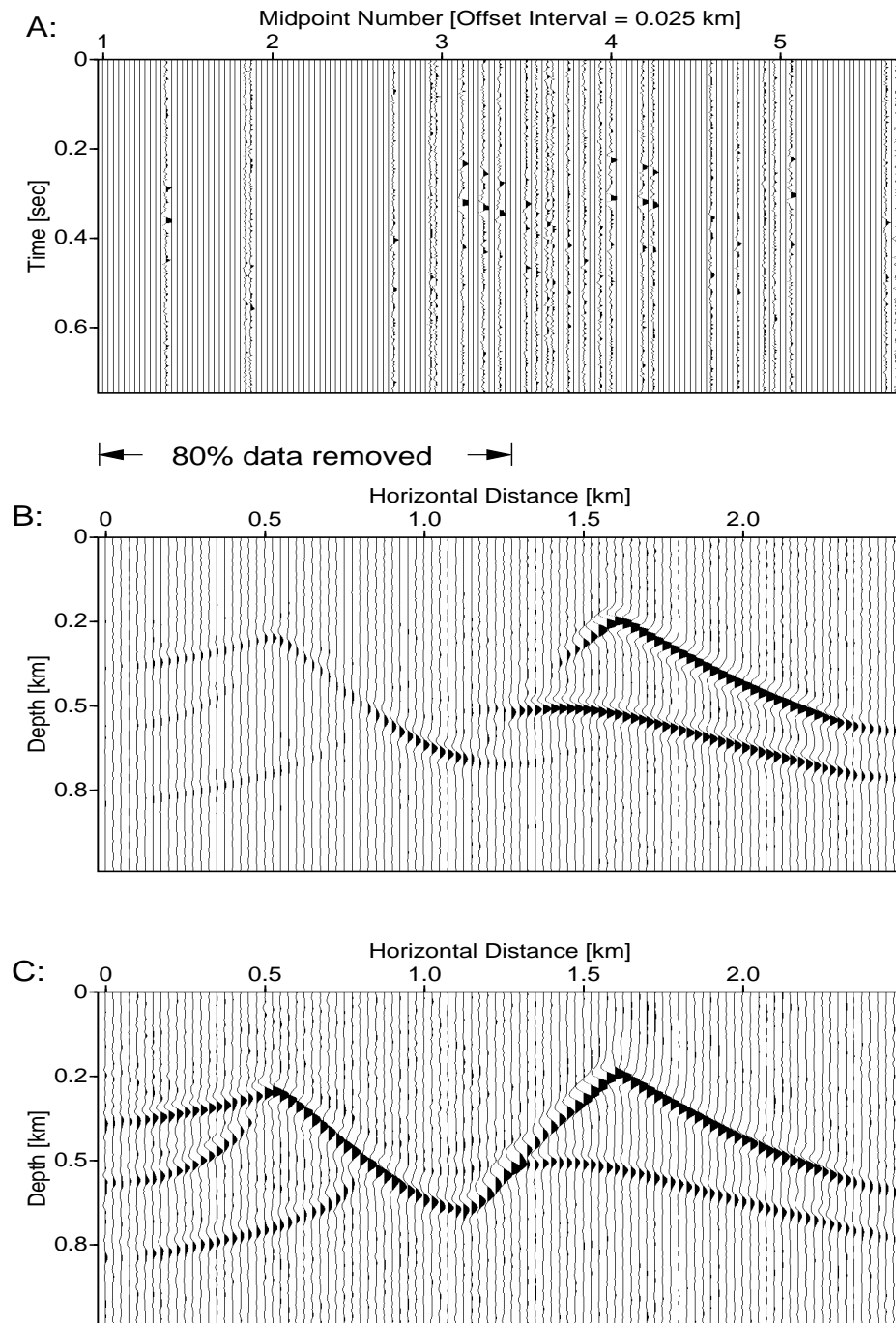
Figure 3.20: Top: Incomplete CMP data with 10% random noise added. Middle: Migration of the incomplete noisy data. Bottom: Least-squares migration of the incomplete noisy data (7 CG iterations).
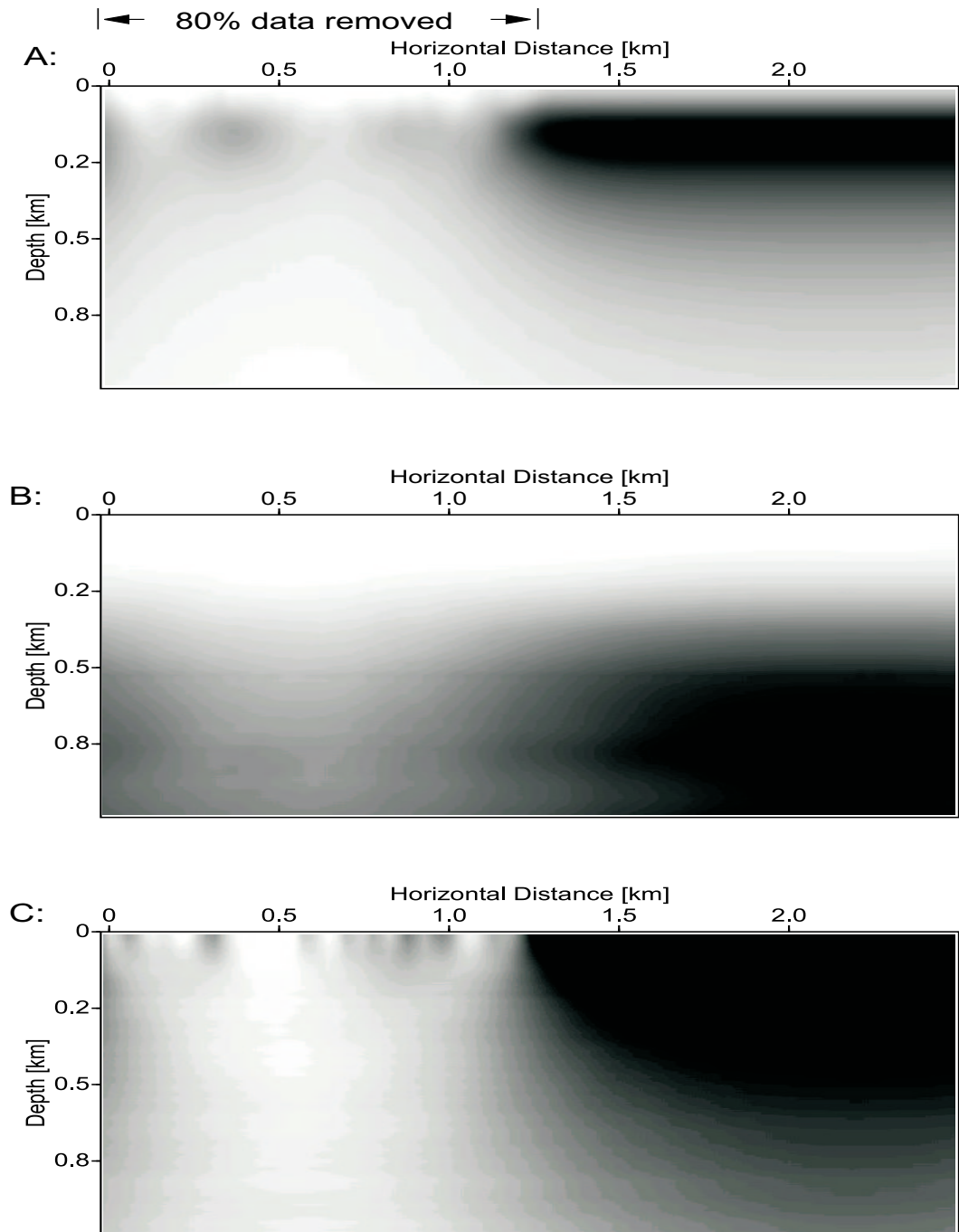
Figure 3.21: Top: Near offset illumination map (100 m). Darker shades mean better illumination. The underlying velocity field increases linearly with depth. Middle: Far offset illumination map (600 m). Far offsets penetrate deeper than the near offsets. Bottom: The illumination map computed for all offsets (0-600 m). The illumination is dominated by the acquisition footprint, especially the near surface.

### 3.2.2 Least-squares migration for AVP/AVA inversion

Reflection angle dependent modelling/migration adds an extra dimension to the seismic image. The ray parameter dependent CIGs carry meaningful and valuable AVP information that is closely related to the target reflector AVA. The CIGs allow to incorporate a smoothing regularization that improves robustness of least-squares migration considerably (Kuehl and Sacchi, 2002). The objective function to be minimized is now equation (2.3.1). It is important to study the selection of the inversion parameters: the tradeoff parameter $\lambda$, and the smoothing length $\Delta p_h$ that is determined by the ray parameter sampling interval. Synthetic (finite-difference) data tests facilitate the determination of parameter combinations that are likely to yield reasonable inversion result when, as with real-world data, the true solution is unknown. Moreover, subsurface models with increasing complexity provide insight into the potentials and pitfalls of least-squares migration for AVP/AVA inversion in general.

The first example is a simple, horizontally layered model. For 1-D earth models less sophisticated techniques, such as trace-by-trace attenuation compensation (e.g., compensation for geometrical spreading) followed by NMO correction, that convert the data into a form suitable for amplitude analysis can work reasonably well (Stolt and Weglein, 1985; Castagna, 1993). However, the relatively low computational cost of least-squares migration in layered media greatly facilitates the study of various aspects considering the algorithm's performance. The second model is structurally slightly more interesting and makes the split-step approximation necessary. However, it poses no real challenge for the split-step propagator. The test primarily confirms that the AVP/AVA inversion formulas also apply to dipping and moderately curved reflectors. The last example in this section is the Marmousi model. As previously described, the Marmousi dataset is based on a variable velocity and density model. The intricate model structure makes the data very realistic. Unfortunately, this complexity also complicates the comparison to the theoretical AVA in equation (1.3.23). Rarely are the events seen in the CIGs due to simple, well isolated interfaces. Most events are merely a superposition of reflections from a series of layers and fine structure, and thus have complex AVA behavior. Despite the dominating 'composite reflectors', two relatively well isolated reflectors have been picked to

| Velocity (m/s) | Density (g/cm$^3$) | Thickness (m) |
|----------------|--------------------|---------------|
| 2000 | 2.25 | 500 |
| 2350 | 1.6 | 300 |
| 1900 | 2.3 | 300 |
| 2500 | 1.7 | 300 |
| 2500 | 2.0 | Half-space |

Table 3.1: Parameters for the horizontally layered model with 4 reflecting interfaces. The parameters have been chosen such that the absolute magnitude of the normal incidence reflection coefficient does not exceed 0.1. This model is considered a low contrast medium. See Figure 3.24 for the angle dependent reflection coefficients. Polarity reversals (180° phase changes) in the AVA occur for the first three reflectors. The last reflector exhibits a constant AVA characteristic.

demonstrate the benefits (and pitfalls) of least-squares migration for AVP/AVA inversion in complex media.

**Horizontally layered model**

The horizontally layered model consists of four reflecting interfaces. The acoustic model parameters in terms of compressional velocities and densities range from 1900 m/s to 2500 m/s and from 1.6 g/cm$^3$ to 2.25 g/cm$^3$, respectively. More details including the layer thicknesses are specified in Table 3.1. All interfaces are well separated. Two meth-
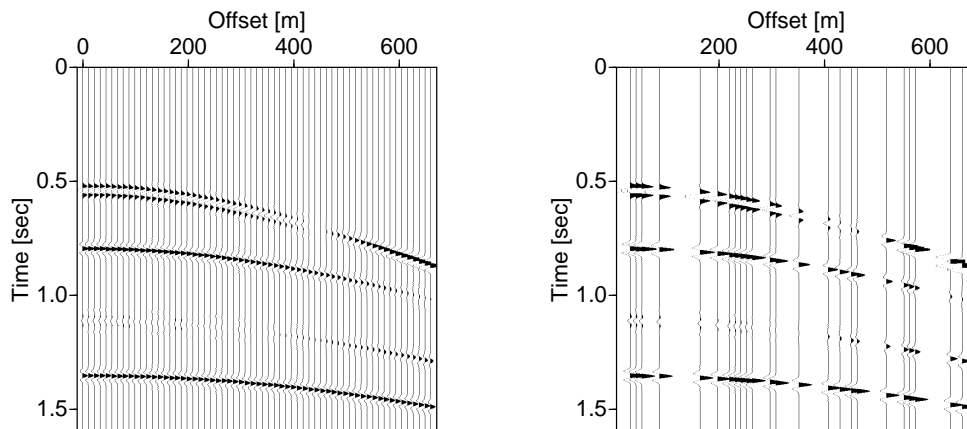


Figure 3.22: Left: CMP gather generated by a ray-tracing code. The code models (cylindrical) geometrical spreading but no transmission effects. The offsets range from 0 to 660 m. The third reflector is about one order of magnitude weaker than the first reflector. Right: The same CMP after randomly removing 50% of the data.
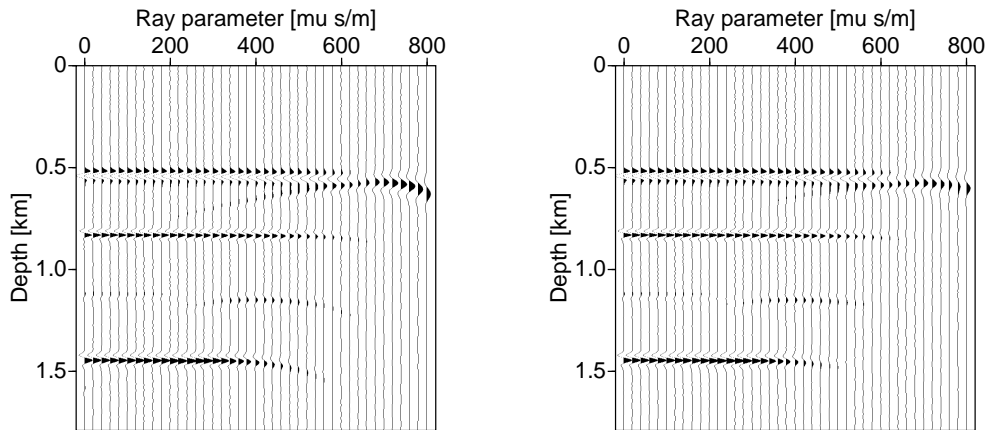
Figure 3.23: Left: Migrated CIG of the complete data. The offset ray parameter axis ranges from 0 to $800\mu s/m$ in steps of $20\mu s/m$. Right: Least-squares migrated CIG (4 iterations) of the complete data.

ods to generate the synthetic data have been chosen for this example: a ray-tracing and a finite-difference modelling technique. Unlike the finite difference algorithm, the ray-tracer does not account for energy partitioning at the interfaces. Hence, a comparison of the inversion results based on the two synthetic datasets reveals the effect of neglecting transmission losses in the inversion. For low contrast media the results are expected to be virtually identical. The example based on the ray-tracing test data is described first. The ray-tracer takes advantage of the fact that, in a stratified medium, the ray parameter is constant for a particular ray. The geometrical spreading has been calculated assuming a cylindrical wavefront resulting in a $1/\sqrt{s}$ amplitude scaling, where $s$ is the distance travelled by the ray. The CMP data are shown in Figure 3.22. They exhibit a clear amplitude variation versus offset (AVO). The offsets range from 0 to 660 m incrementing by 11 m. This corresponds to an offset-to-depth ratio of about $0.5$ for the deepest reflector. Figures 3.22 shows the same data after randomly removing $50\%$ of the live traces. The reduced dataset is used when the performance of the data-weighting operator $\underset{\sim}{\mathbf{W}}$ and the model regularization in equation (2.3.1) are to be tested under more difficult circumstances. Removing data is a simple way of introducing errors in the data.

Figure 3.23 depicts the migrated ray parameter CIG and the least-squares migrated ray parameter CIG after 4 iterations of the CG algorithm. The apparent AVP of the mi-
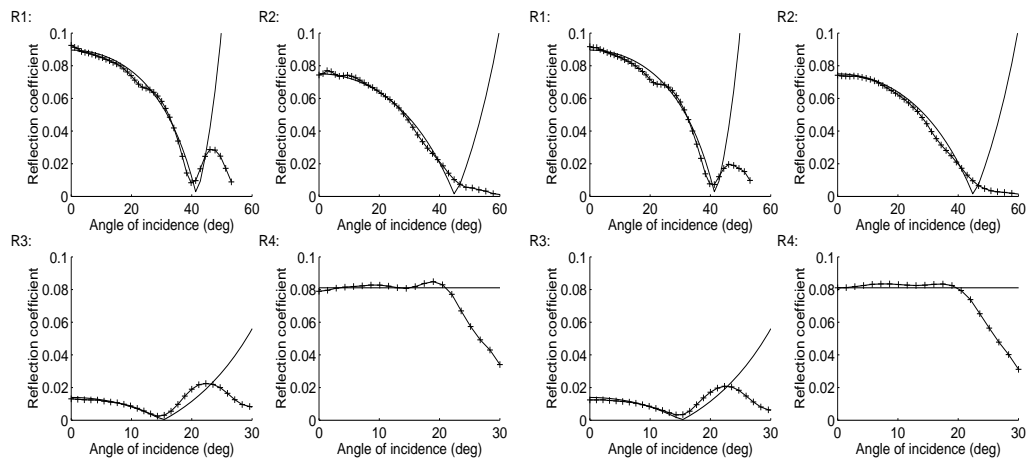
Figure 3.24: Left (R1-R4): AVA picked on the migrated CIG in Figure 3.23 (left). The labels R1 to R4 correspond to the four reflectors from top to bottom. The absolute amplitudes have been picked. All values have been scaled with the inverse of the ray parameter imaging Jacobian for horizontal interfaces. The moduli of the true AVA are shown as solid lines. Right (R1-R4): The same picks based on the least-squares CIG in Figure 3.23 (right) after 4 iterations of the CG algorithm. No angle dependent scaling has been applied.

grated CIG is slightly compromised by finite aperture effects. The wavelet broadening (dispersion) towards high ray parameters seen for the first reflector is explained by the frequency tapering effect inherent in the radial trace transform (see also Figure 1.10). The migrated CIG is otherwise clean and of good quality. The smearing due to the finite aperture is mitigated in the least-squares migrated result. The tradeoff parameter was set to $\lambda = 0.01$ and the ray parameter increment was $\Delta p = 20\mu s/m$ resulting in a moderate smoothing effect to ensure AVP/AVA preservation. Apart from some finite aperture effects the migrated and the least-squares migrated result are of comparable quality. This is confirmed by the AVP to AVA converted amplitude picks in Figure 3.24. The amplitude picking procedure involves the definition of windows on the CIGs and the determination of the absolute values within these windows. Since the absolute values have been picked sign changes appear as cusps in the AVA curves. Note that the cusps are not in contradiction to the smoothness constraint, since smoothness is enforced on the CIGs, not the AVA curves. Both the migrated picked AVA and the least-squares migrated AVA match the theoretical AVA closely for a large range of incidence angles. Inevitable finite recording aperture effects cause the AVA of all reflectors to eventually taper off to zero.
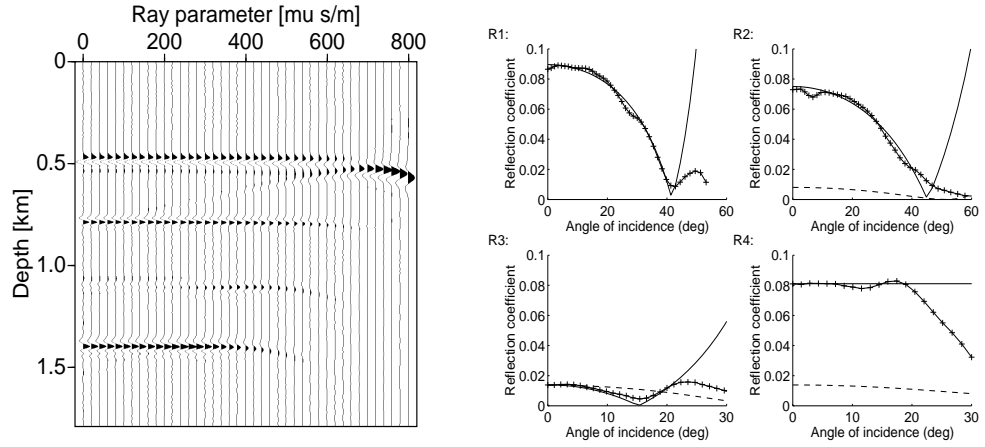
Figure 3.25: Left: Migrated CIG of the complete finite-difference data. As opposed to the ray-tracing data the wavelet has been shifted to be zero-phase. This explains the slightly earlier onset of all signals. Right: The corresponding picked AVA. The dashed line indicates the theoretical cumulative error due to neglected transmission losses.

Next, synthetic data generated by a finite-difference algorithm based on the full acoustic wave-equation have been inverted. Figure 3.25 shows the migrated CIG and the picked AVA. The CIG based on the ray-tracing data in Figure 3.23 and the CIG in Figure 3.25 are very similar. Differences are attributed to transmission loss, first arrival muting artifacts and a slightly narrower offset range for the finite difference input data. Furthermore, the highest frequencies may have been distorted slightly by finite-difference grid dispersion (Press et al., 1997). The picked AVA in Figure 3.25 follows the theoretical AVA closely. For comparison, the theoretical cumulative transmission losses are also plotted in Figure 3.25 indicating that the transmission angle dependence is weak in this case, but can have a negative impact where the AVA is small.

Based on the above findings one can conclude that migration gives reliable AVA estimates in layered media, provided the data are well sampled along offset and noise free. Of course, the inverse ray parameter imaging Jacobian $\mathcal{J}^{-1}$ needs to be applied. Nonetheless, it is important to keep in mind that the primary data representation assumes a low contrast medium and the absence of fine layering. While constrained least-squares migration helps to suppress spurious energy, the computing intensive least-squares migration is expected to be more compelling when the data sampling is poor.
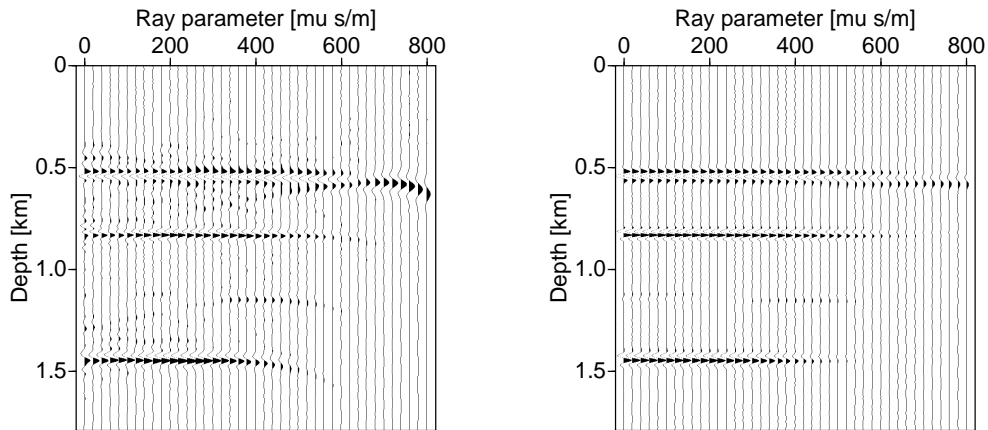
Figure 3.26: Left: Migrated CIG of the incomplete data. Right: Least-squares CIG (14 iterations) of the incomplete data. The data misfit for the least-squares migration is shown in Figure 3.27.

To challenge the inversion algorithm input data with significant irregularity, the reduced CMP in Figure 3.22 was inverted. The migrated CIG in Figure 3.26 clearly bears the stamp of acquisition footprint noise. The amplitudes are discontinuous along the ray parameter axis, and there is spurious energy between the reflectors. The least-squares migrated CIG (14 CG iterations) in Figure 3.26 is overall cleaner and exhibit a smooth AVP.

To ensure that the data weighting operator takes full effect the data residuals have been minimized to the point where the data misfit levels off to its plateau. Figure 3.27 is the data misfit up to 19 iterations of the CG algorithm. In this example, 14 iterations were sufficient to achieve a good inversion result. The picked AVA of the migrated and the least-squares migrated CIGs are portrayed in Figure 3.28. The migrated AVA curves are distorted. Especially, the AVA estimation for the two deepest reflectors is poor. On the other hand, when picked



Figure 3.27: Normalized data misfit (incomplete data).

on the least-squares CIG the curves are smooth and follow largely the theoretical AVA. For large ray parameters, where there is an abrupt change in the AVA due to the finite recording aperture, the smoothing regularization averages some of the finite offset effects
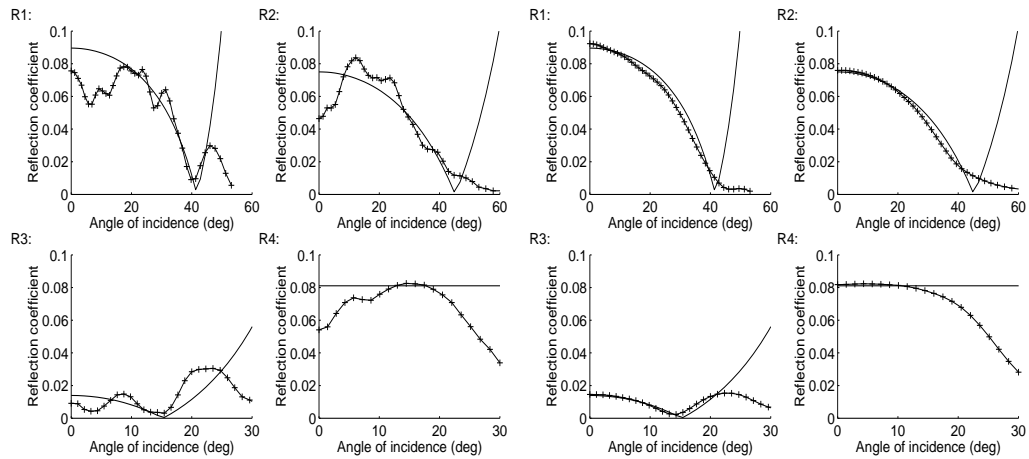
Figure 3.28: Left (R1-R4): AVA picked on the migrated CIG in Figure 3.26 (left). 50% of the data were randomly set to zero prior to migration (see also Figure 3.22). Right (R1-R4): The same picks based on the least-squares migrated CIG (14 iterations) in Figure 3.26 (right).

into the previously recoverable angle range. This is a reminder that smoothing has to be applied with care to avoid solutions that are 'too smooth' or 'too flat'. In this example, the tradeoff parameter was $\lambda = 0.01$. Compare this result also to Figure 3.24.

Figure 3.29 shows the CIG based on the incomplete data after 10 CG iterations and the least-squares CIG when the data weighting operator $\mathbf{W}$ in equation (2.3.1) is the identity
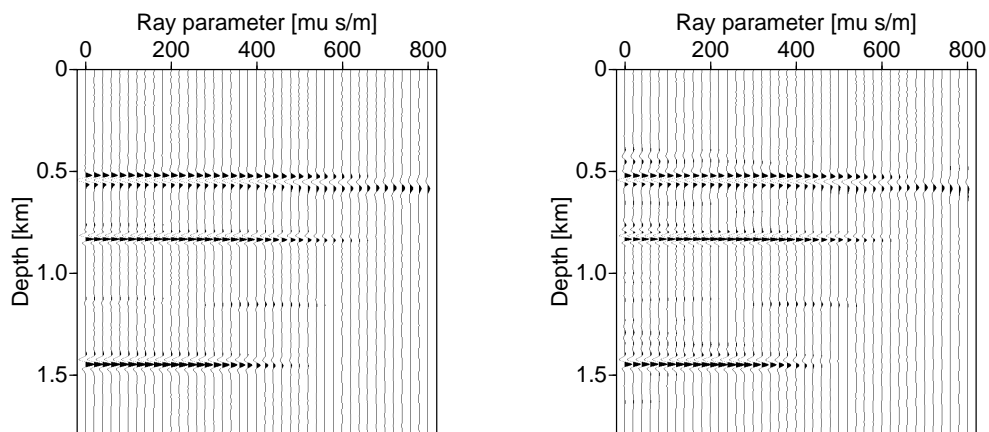


Figure 3.29: Left: Least-squares migrated CIG (10 iterations) of the incomplete data. Right: Least-squares migrated CIG (14 iterations) of the incomplete data without data weighting.

operator. The least-squares CIG after 10 iterations looks virtually identical to the one after 14 iterations in Figure 3.26. In terms of amplitudes, however, the picked AVA in Figure 3.30 reveals subtle differences. The least-squares CIG without data weighting exhibits residual wavelet distortions that are absent in the least-squares migrated CIG in Figure 3.26. Obviously, the AVA curves in Figure 3.30 are biased by the missing data. The curves are merely a smoothed version of the migration result in Figure 3.28. This example supports the important point that weighted least-squares migration produces smooth and clean solutions and yet fits the seismic data in a sensible way. That is, regularized least-squares migration can be interpreted as data consistent AVA smoothing.

The next example tests how random noise influences the inversion result. To make sure that the AVA is not too severely deteriorated noise with a moderate signal-to-noise ratio of 10 has been added, where the maximum absolute amplitude defines the signal strength. Figure 3.31 is the migrated and the least-squares migrated CIGs using the incomplete and noisy data. Clearly, the additional noise has further degraded the migrated CIG. The least-squares CIG (14 iterations) is significantly cleaner and has a smooth AVP. The corresponding picked AVA is shown in Figure 3.32. As expected, the migrated AVA
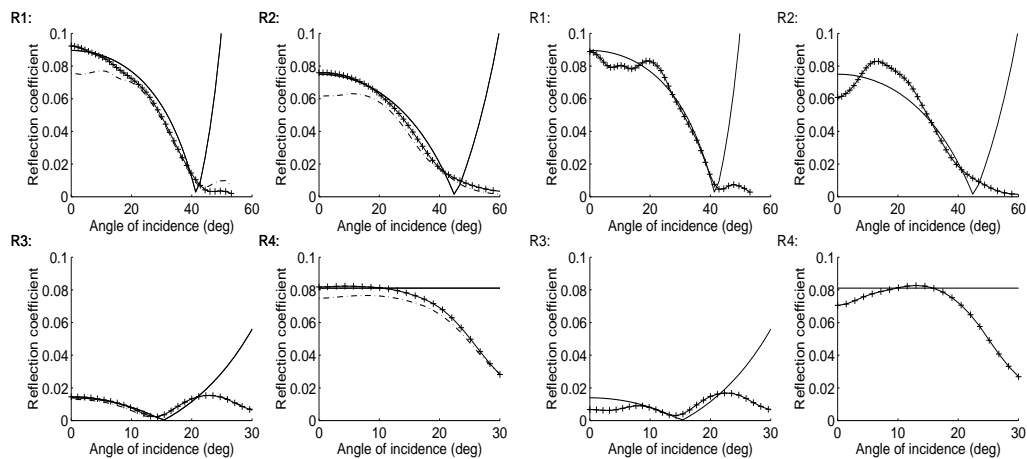


Figure 3.30: Left (R1-R4): AVA picked from the least squares-migrated CIG (10 iterations) in Figure 3.29 (left) shown as the dot-dashed line. The crossed line is the previously shown result after 14 CG iterations. Right (R1-R4): The picks based on the least squares migrated CIG (14 iterations) in Figure 3.29 (right) where the data weighting operator $\mathbf{W}$ has been replaced by the identity operator.
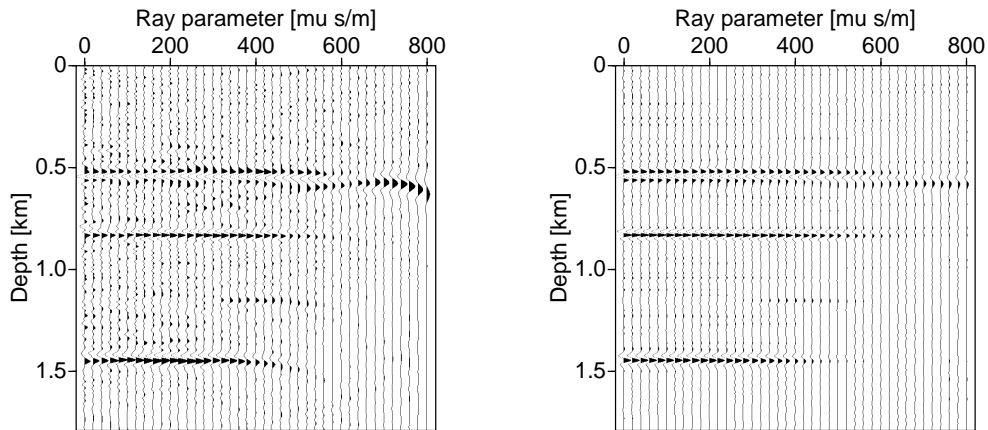
Figure 3.31: Left: Migrated CIG of the incomplete and noisy data. Right: Least-squares migrated CIG (14 iterations) of the incomplete and noisy data.

suffers significant distortions from acquisition footprint and random noise, whereas the least-squares migrated AVA matches the theoretical values much better, but is certainly not perfect. The high noise level relative to the third reflector has caused some deviation from the true AVA. The last test in this series confirms that this deviation is indeed due
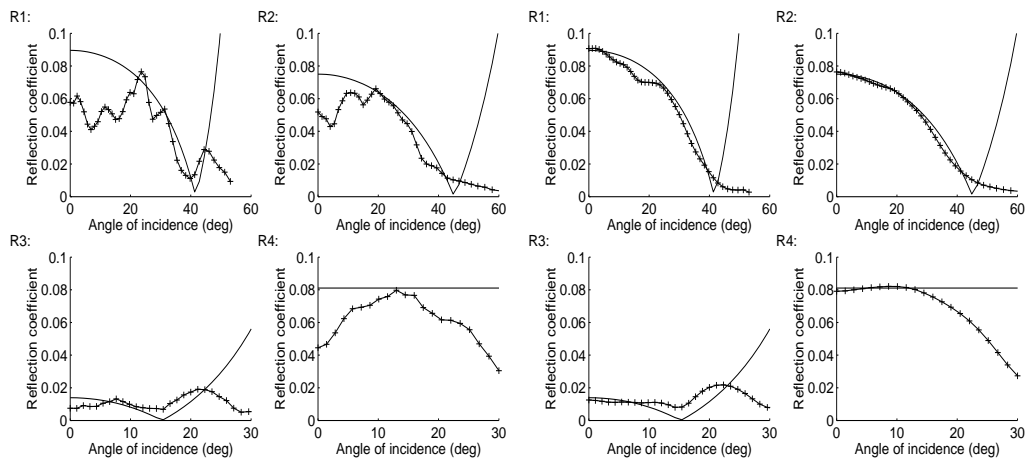


Figure 3.32: Left (R1-R4): AVA picked on the migrated CIG in Figure 3.31 (left). The data were incomplete and random noise with a signal to noise ratio of 10 (based on the absolute maximum amplitude) has been added. Right (R1-R4): The same picks from the least-squares migrated CIG (14 iterations) in Figure 3.31 (right).
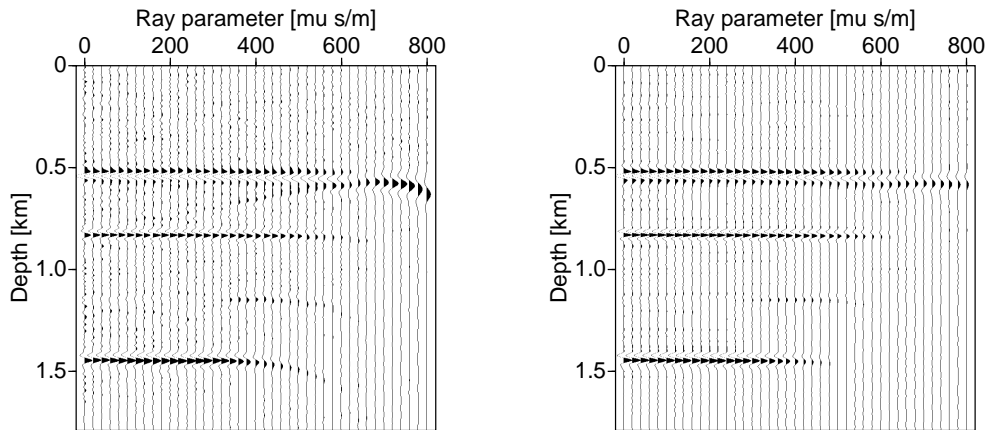
Figure 3.33: Left: Migrated CIG of the noisy data. Right: Least-squares migrated CIG (4 iterations) of the noisy data.

to random noise. This time, the input data were noisy but complete. See Figure 3.33 for the migrated and least-squares migrated CIGs. The associated AVA curves are in Figure 3.34. The least-squares migrated AVA curves are smoother than the migrated ones with both showing essentially the same trend. Since the data weighting operator $\mathbf{W}$ is the identity matrix except for a few padded far offset samples, the data misfit has not
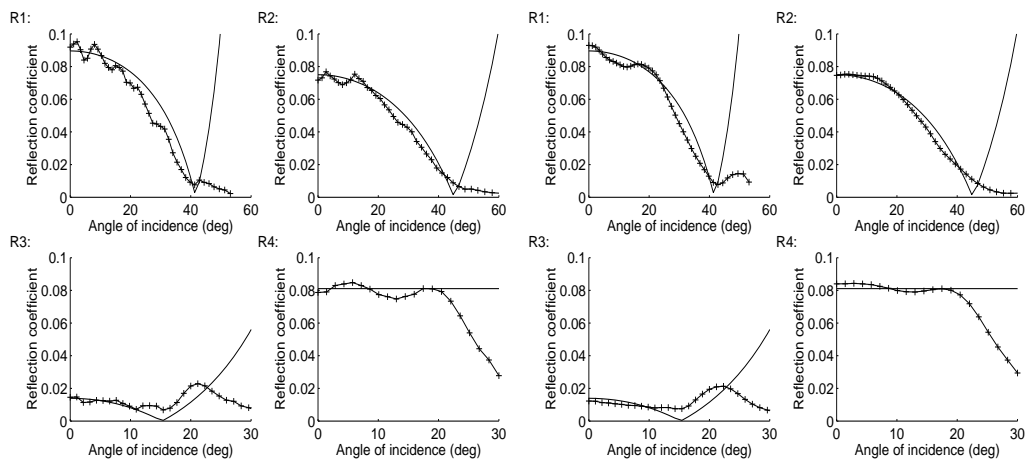


Figure 3.34: Left (R1-R4): AVA picked on the migrated CIG in Figure 3.33 (left). White noise with a signal-to-noise ratio of 10 has been added. Right (R1-R4): The same picks from the least-squares migrated CIG (4 iterations) in Figure 3.33 (right).

been minimized to its plateau. It seems reasonable to conjecture that smoothing and amplitude scaling equivalent to the application of the inverse imaging Jacobian takes effect after a few iterations.
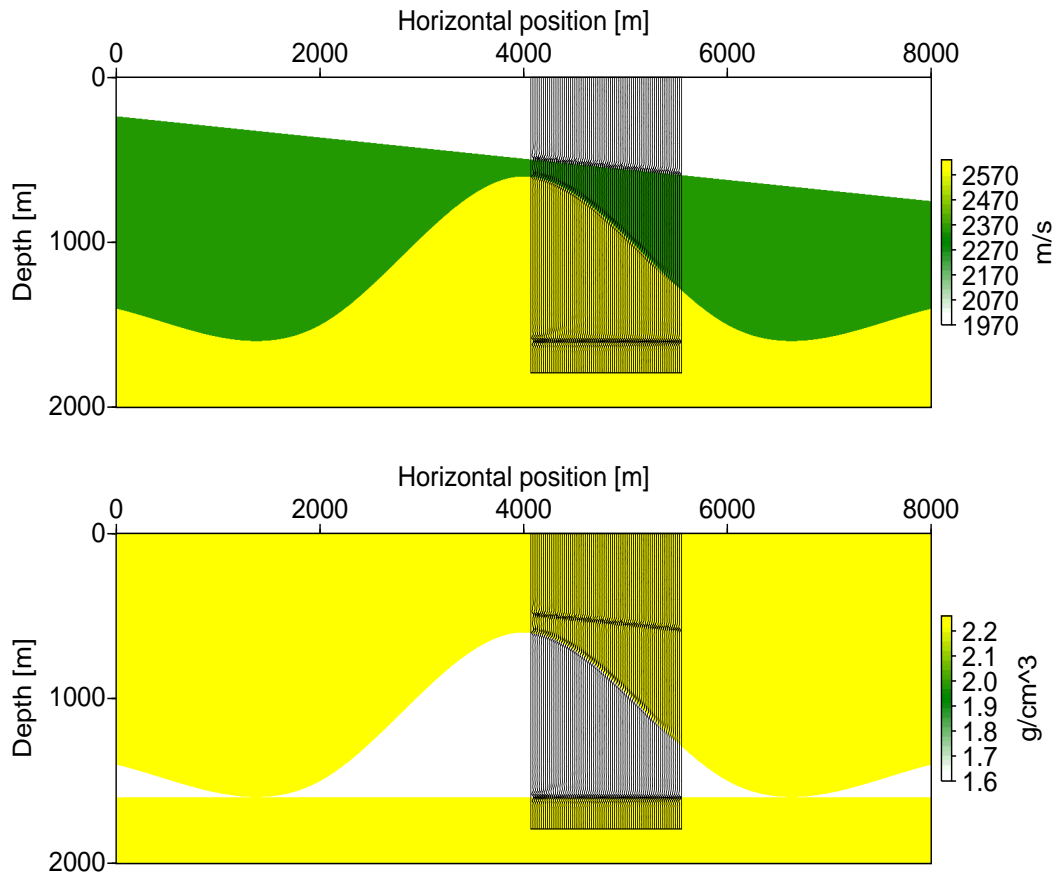
Figure 3.35: Velocity (top) and density model (bottom) with a slightly dipping, a moderately curved and dipping, and a flat reflector. The flat reference reflector is represented by a density change only. The migrated and stacked sections are shown as overlays.

**Model with a curved interface**

The previous model was restricted to depth dependent velocities allowing for a fast computational turnaround. The next model is also relatively simple but has lateral structure. Figure 3.35 portrays the velocity and density fields. The data have been generated by finite-difference modelling with offsets that range from 0 to 1140 m incrementing by $\Delta h = 20$m. The stacked split-step migration images a small portion of the model, shown as overlays in Figure 3.35. Figure 3.36 is the migrated and the least-squares migrated CIG at CMP location 4600 m. The relatively coarse offset sampling caused aliasing artifacts
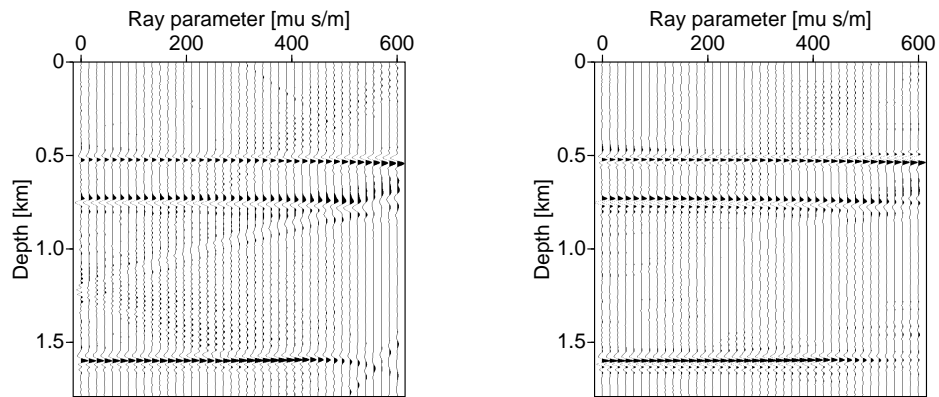
Figure 3.36: Left: Migrated CIG at CMP location 4600 m (see Figure 3.35). Finite aperture effects and offset aliasing cause spurious energy in the CIG. Right: Least-squares CIG (6 iterations) at CMP location 4600 m. Most of the spurious energy has been cleaned up. The picked AVA for the second and the third reflector are shown in Figure 3.37.

in the migrated CIG, whereas least-squares migration (6 iterations with $\lambda = 0.006$ and $\Delta p_h = 15\mu s/m$) suppresses the aliasing noise effectively. Figure 3.36 shows the picked AVA of the middle and the bottom reflector. The dot-dashed line is the AVA when the local dip angle in equation (1.3.33) is not considered in the AVP to AVA conversion. The result confirms nicely that a specular reflection process also holds for moderately curved interfaces.
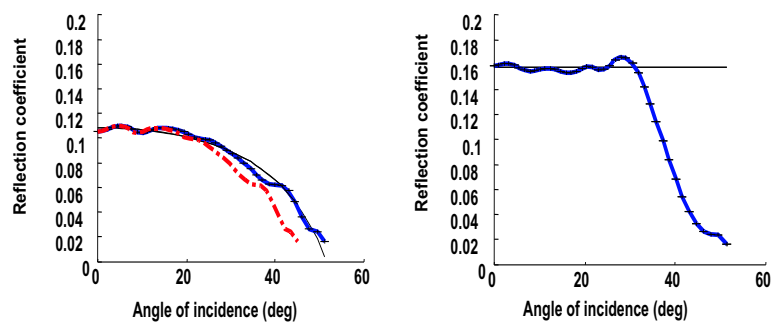


Figure 3.37: Left: AVA for the second reflector picked on the least squares CIG in Figure 3.36. The dot-dashed line indicates the AVA without dip correction. Right: AVA for the third reflector picked on the least-squares CIG in Figure 3.36.

**The Marmousi model**

The Marmousi model has been extensively described previously. As mentioned earlier, imaging techniques based on the high-frequency approximation (i.e., ray-tracing based imaging) often struggle to produce a good structural image of the Marmousi model. The relatively simple split-step wavefield propagator, on the other hand, yields good results. This is confirmed by the migrated image in Figure 3.4 shown earlier. Here the focus is on AVP/AVA inversion issues. The complex structure of the Marmousi model makes a careful selection of the depth point whose AVA is to be estimated crucial. Two criteria guided the selection process. First, the depth points should be located in the upper half of the model so as to ensure sufficiently large ray parameter/angle range coverage. Second, to compare the inverted AVA with the theoretical AVA the picked reflection event, the target, ought to be generated by a single, locally plane, interface. The Marmousi model is complex with significant fine layering. Hypothetically, composite reflections from mul-
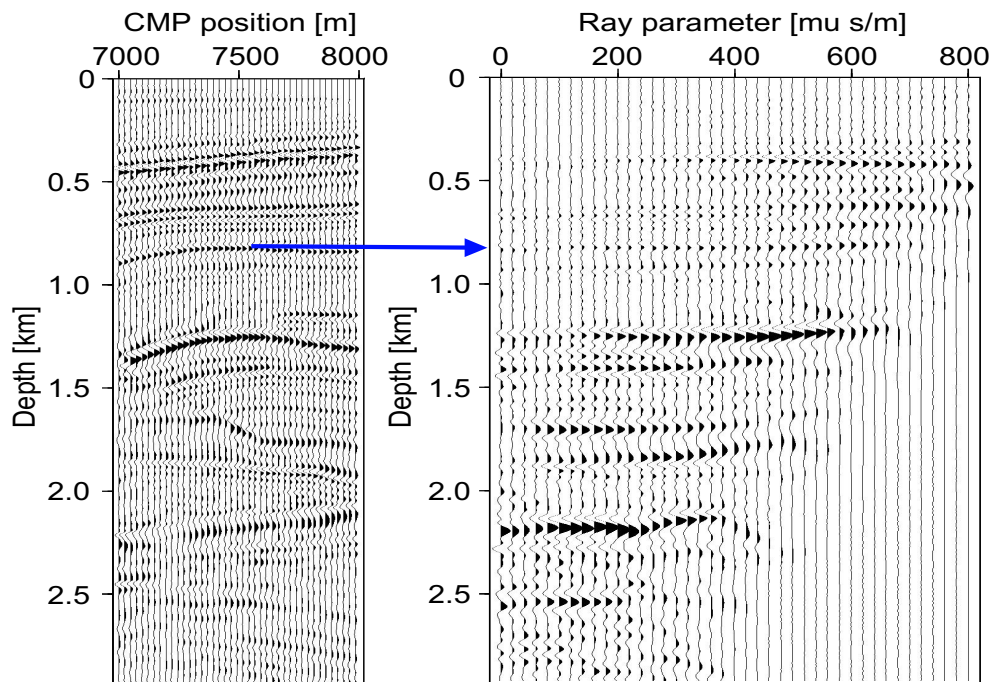


Figure 3.38: Left: Portion of the migrated and stacked Marmousi image. Right: CIG at CMP location 7500 m. The arrow indicates the reflector picked for AVA analysis.
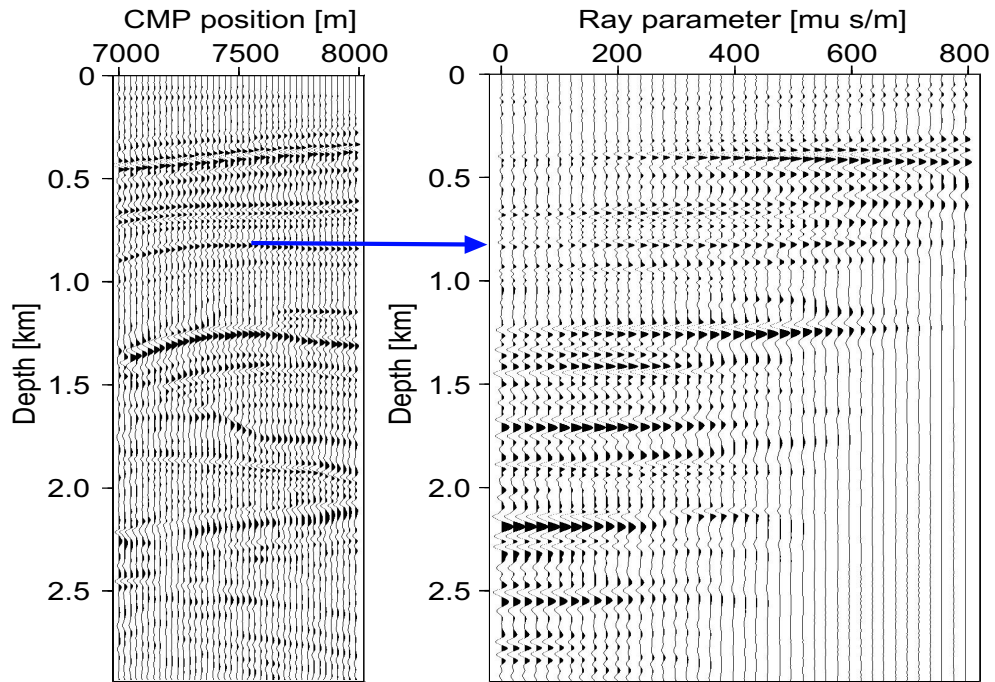
Figure 3.39: Left: Portion of the migrated and stacked Marmousi image. Right: Least-squares migrated CIG (4 iterations) at CMP location 7500 m.

tiple interfaces ('tuning effects') could be modelled and compared to the inverted CIGs, but this approach has not been pursued. Given the relatively low frequency content of the source wavelet only few reflections satisfy the 'single interface criterion'.

Figure 3.38 shows the first target reflector at CMP location 7500 m. The left image is a portion of the migrated and stacked Marmousi data with the arrow indicating the picked target phase in the CIG. All available offsets of the Marmousi data have been used in the migration. As it is often the case in reality, the near offsets up to 100 m are missing. The consistent absence of near offset information causes a dim region for small ray parameters. Visual inspection of the gathers can help to identify regions of missing data information. These areas should be excluded from a subsequent inversion for elastic/lithologic parameters. Figure 3.39 shows the same midpoint CIG after 4 iterations of the least-squares algorithm using a moderate smoothing regularization ($\lambda = 0.01$, $\Delta p = 15\mu s/m$). The energy in the previously dim zone has been partially boosted. Nevertheless, the small ray parameter amplitudes have to be interpreted with caution. Overall,

95
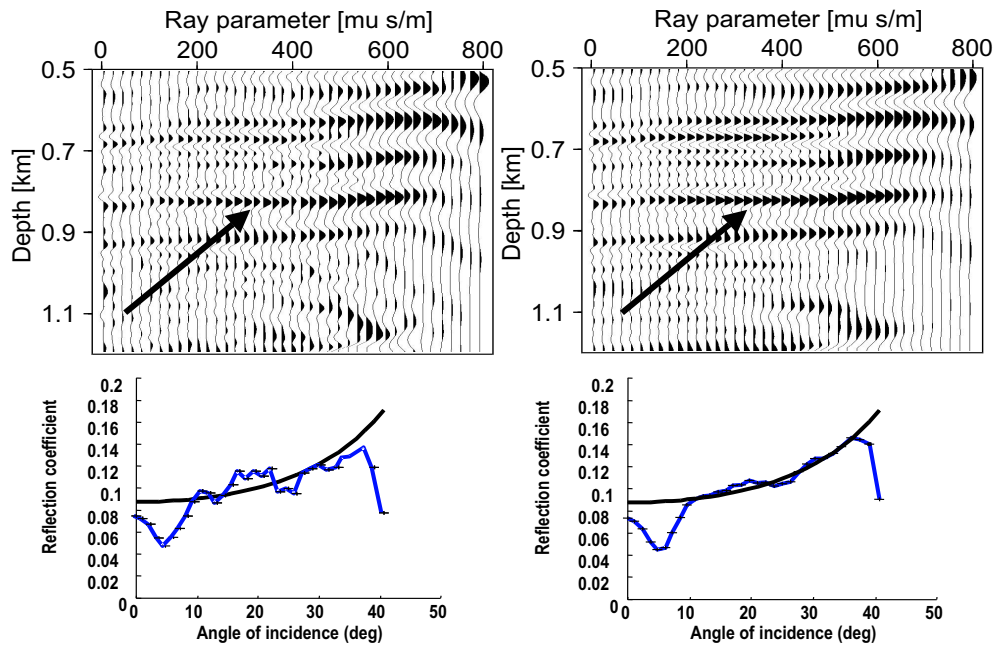
Figure 3.40: Left: Blow-up of the migrated target reflector CIG and the picked AVA curve. Right: Blow-up of the least-squares migrated target reflector CIG (6 iterations) and the corresponding AVA. One has to take care not to produce solutions that are 'too flat'.

the least-squares CIG exhibits improved wavelet continuity along ray parameter and appears more interpretable. However, it is once more emphasized that the interpretation of the amplitudes in terms of specular reflections breaks down where the target reflector is strongly irregular or has lateral support on the order of the dominant wavelength or less. In any case, as far as structural imaging is concerned, the stacked ray parameter CIGs yield the familiar DSR migration result.

Figure 3.40 zooms in on the target reflector for both the migrated and the least-squares migrated CIG. The picked AVA curves are shown below the CIGs. The AVA is biased by the missing near offset traces. Despite its roughness, the AVA curve picked on the migrated CIG agrees with the theoretical AVA trend. The least-squares migrated AVA after 6 iterations is smooth and closer to the true AVA. However, a higher number of iterations produces a solution that is 'too flat'. Since least-squares migration is computationally expensive, one desires to compute as few CG iterations as possible. A relatively high tradeoff parameter yields smooth and cleaner CIGs fast but can also jeopardize the AVA
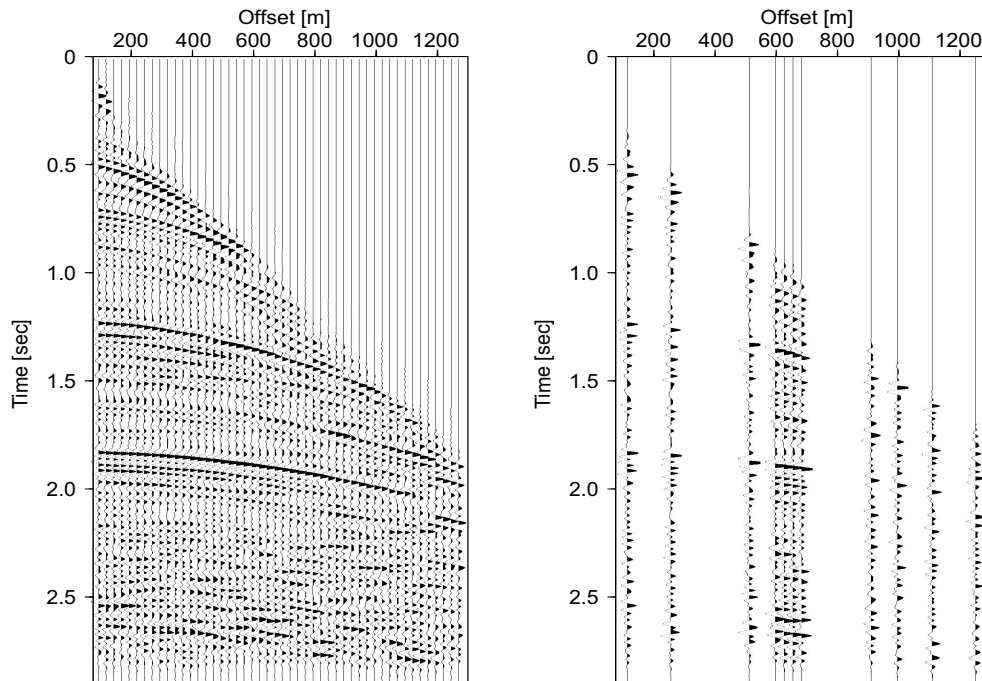
Figure 3.41: Left: CMP data at location 7500 m of the Marmousi model. Notice that the first live trace is at (half) offset 100 m. Right: The CMP after removing 70% of the live traces.

fidelity. Ideally, one would like to have a universal parameter $\gamma = \lambda^2 \times \Delta p_h$ that warrants AVA fidelity and yet produces smooth solutions efficiently. Future tests will show whether it is possible to come up with reliable, data independent values for $\gamma$.

In order to test the effect of sub-optimal wavefield sampling 70% of the Marmousi data have been randomly set to zero. The CMP data at location 7500 m in Figure 3.41 illustrate the sparseness of the reduced dataset. The corresponding migrated and least-squares migrated CIGs and their AVA curves are shown in Figure 3.42. The irregular acquisition geometry has left a strong imprint on the migrated CIG, and the reduced wavelet continuity is also reflected in the AVA picks. Although the correct AVA trend appears to be preserved the footprint noise renders a reliable AVA fit questionable, whereas the least-squares migration (12 iterations) restores continuity and reduces the footprint noise considerably. A comparison with the least-squares CIG using the full data in Figure 3.40 confirms that almost all retrieved events are real. The least-squares AVA matches the true AVA between 15 and 35 degrees. Missing data and perhaps smoothing have some-

97
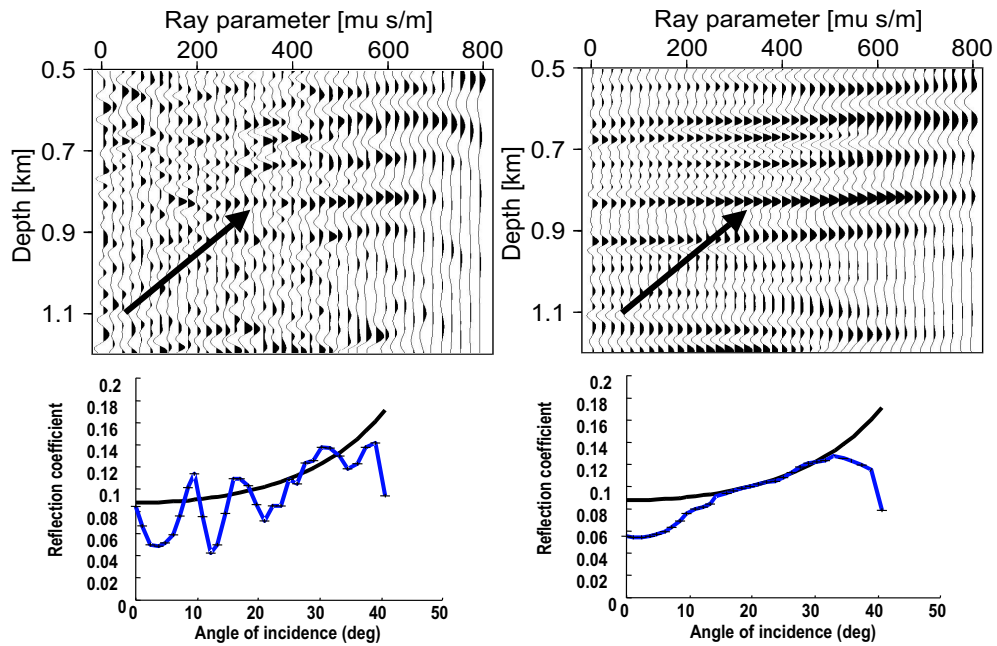
Figure 3.42: Left: Blow-up of the migrated target reflector and the picked AVA curve (incomplete wavefield data). Right: Blow-up of the least-squares migrated target reflector CIG (12 iterations) and the corresponding AVA (incomplete wavefield data).

what reduced the recovered angle range.

Figure 3.43 illustrates the second location chosen for an AVA study. The target reflector is dipping with $\phi = 30°$ and is located in the more complex, faulted area of the Marmousi model. Figure 3.43 depicts the least-squares migrated CIG for location 6200 m adjacent to the stacked migration. Figure 3.44 zooms in on the least-squares CIGs based on the complete and the incomplete data. The CIGs are strikingly similar. The wavefield phase with the strong positive anomaly for large ray parameters is identified as the target. The picks with and without dip correction are plotted in Figure 3.44. The dip correction helps to improve the match between the picked AVA and the theory. However, the match between the picked and the theoretical AVA based on the 'single interface assumption' is not quite as obvious as in the previous examples. This is attributed to fine structure AVA effects and, possibly, cumulative transmission losses caused by the relatively complex overburden.

Finally, the Figures 3.45, 3.46 and 3.47 compare constant ray parameter images ($p_h = $
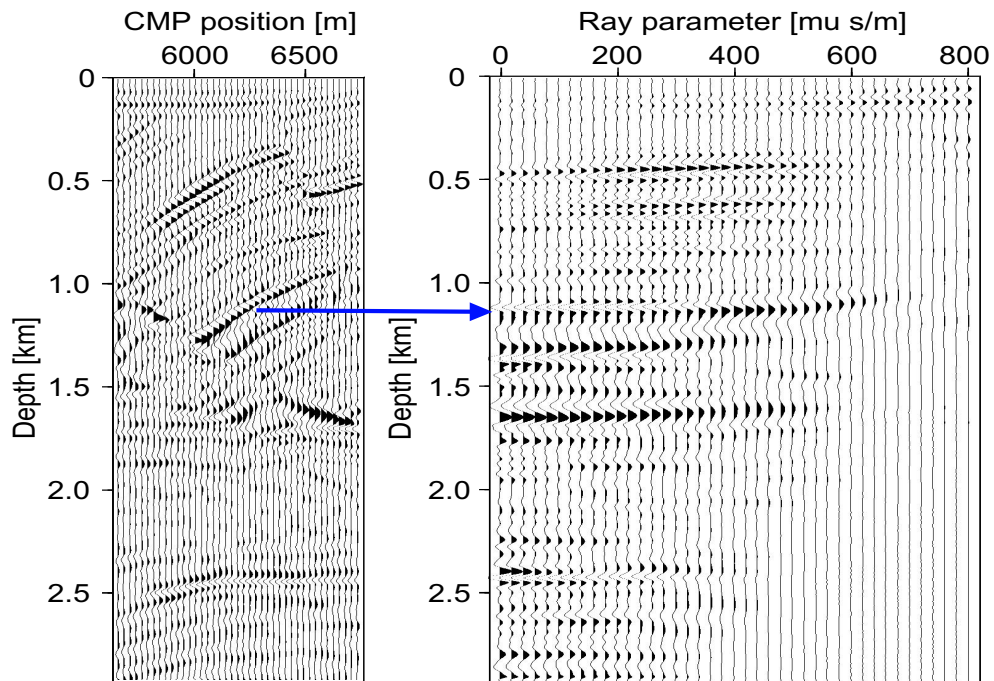
Figure 3.43: Left: Portion of the migrated and stacked Marmousi image CMP. Right: Least-squares migrated CIG (4 iterations) at CMP location 6200 m.

$400\mu s/m$) of the migrated complete data, the migrated incomplete data and the least-squares migrated incomplete data, respectively. The image quality in Figure 3.45 is clearly inferior to the migrated image in Figure 3.4. This is not surprising, since Figure 3.4 is equivalent to the summation over all constant ray parameter images. Figure 3.46 depicts the migrated incomplete data in which kinematic artifacts due to missing data have further deteriorated the image quality. Instead, the least-squares migrated constant ray parameter image in Figure 3.47 is comparable, and in many areas even superior, to the migrated complete data in Figure 3.45. In terms of kinematic artifact reduction, the smoothing regularization has a very similar effect as ray parameter stacking.

Yet another way to glean the inversion success is by comparing the original input data to the reconstructed data. The reconstructed data results from the application of the modelling operator. Figure 3.48 depicts both the complete and the reduced constant offset (500 m) Marmousi data. Figure 3.49 is the reconstructed data after the first CG iteration based on the incomplete input. The data gaps have been partially filled but streaks

remain clearly visible. After 12 iterations the wavefronts have been largely healed and the energy is well balanced. The reconstruction agrees well with the original data in Figure 3.48 (top). Most of the differences are attributed to the single scattering approximation of the modelling and migration operators.
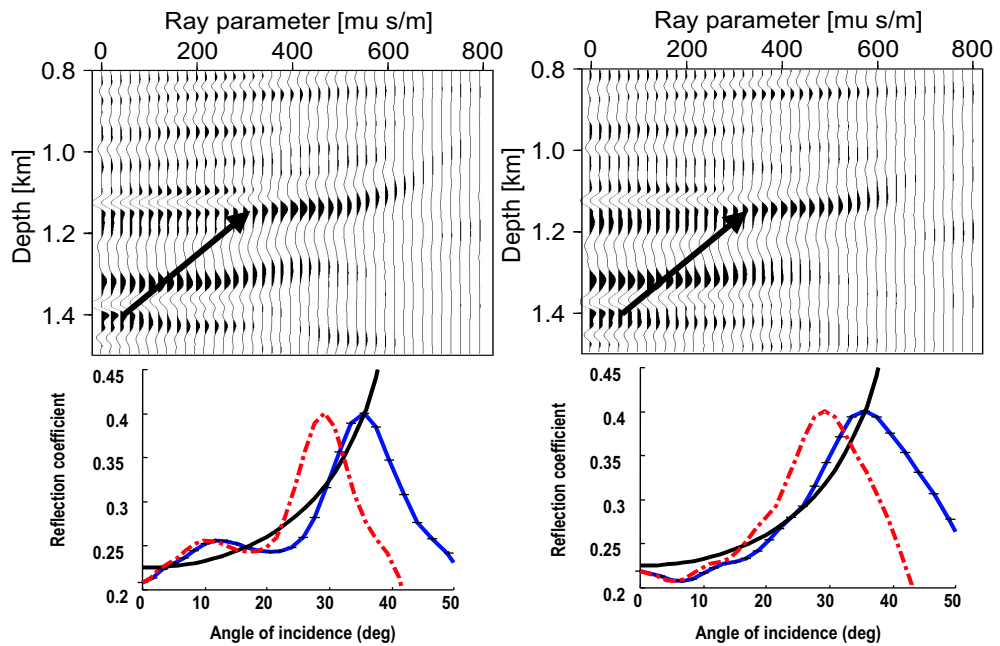
Figure 3.44: Left: Blow-up of the least-squares migrated target reflector CIG (4 iterations) and the picked AVA curve (complete wavefield data). The dot-dashed line is the AVA without dip correction. Right: Blow-up of the least-squares migrated target reflector CIG (12 iterations) and the corresponding AVA (incomplete wavefield data).
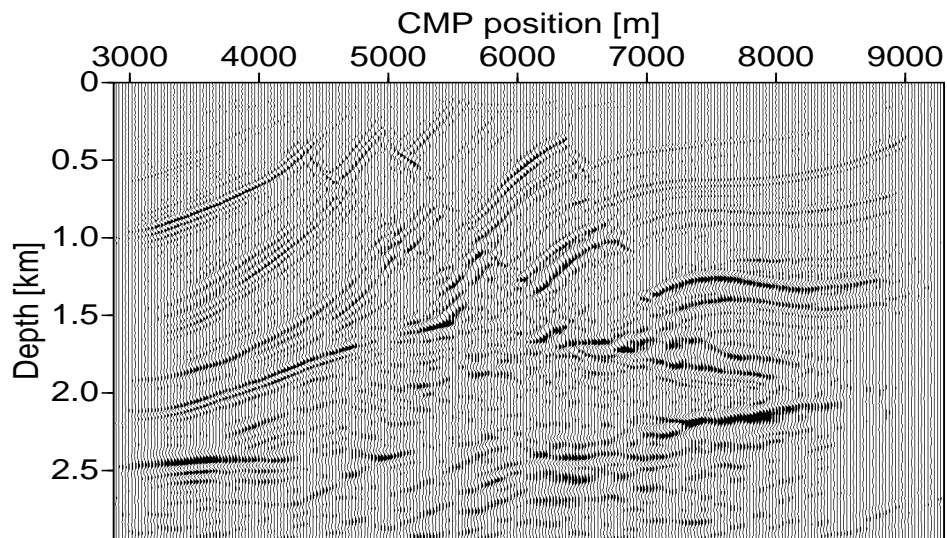


Figure 3.45: Constant ray parameter migration of the Marmousi model ($p_h = 400\mu s/m$). All available wavefield data were used in the migration.

101
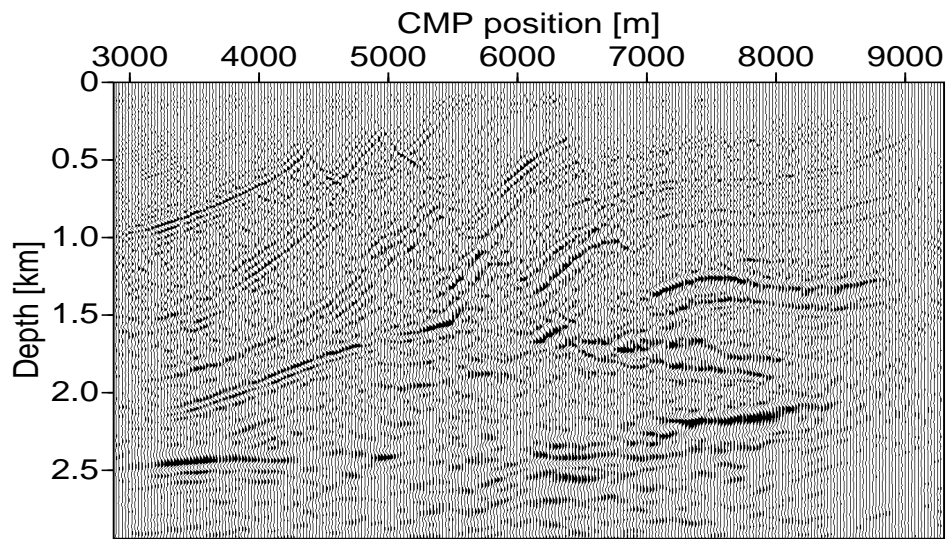
Figure 3.46: Constant ray parameter migration of the Marmousi model ($p_h = 400\mu s/m$). Only 30% of the available wavefield data were used in the migration.
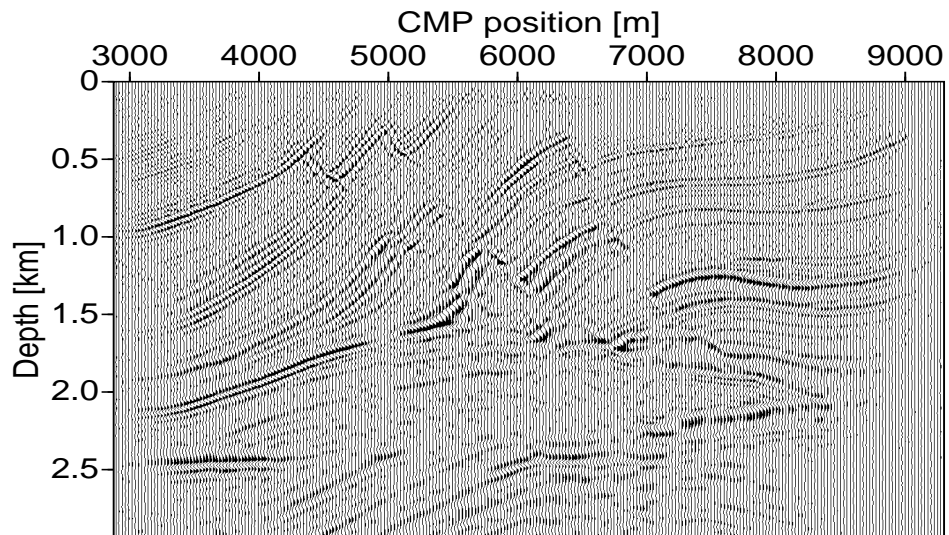


Figure 3.47: Constant ray parameter least-squares migration image of the Marmousi model ($p_h = 400\mu s/m$). Only 30% of the available wavefield data were used in the least-squares migration.
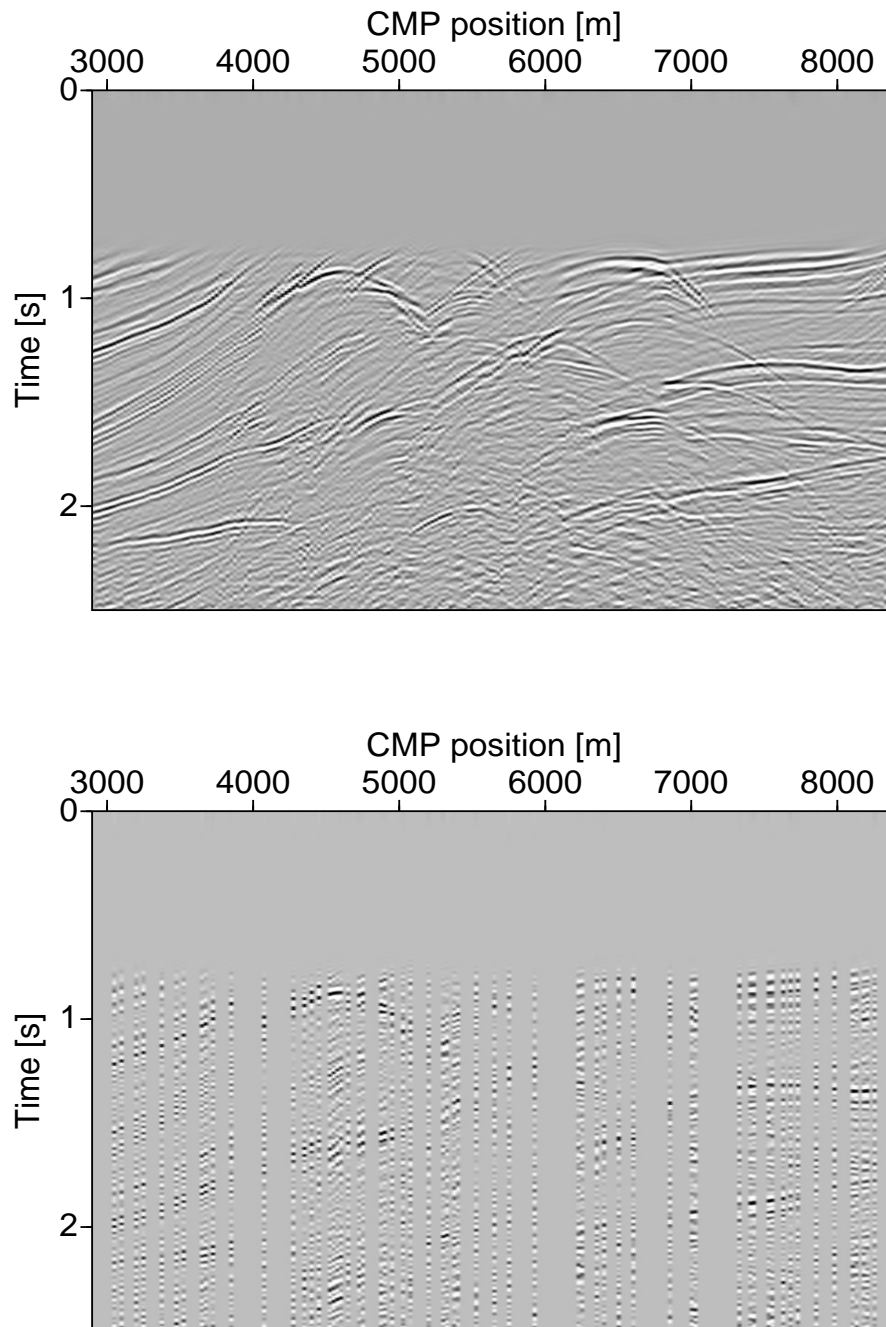
Figure 3.48: Top: Complete constant offset (500 m) Marmousi dataset. Bottom: 70% reduced constant offset dataset.
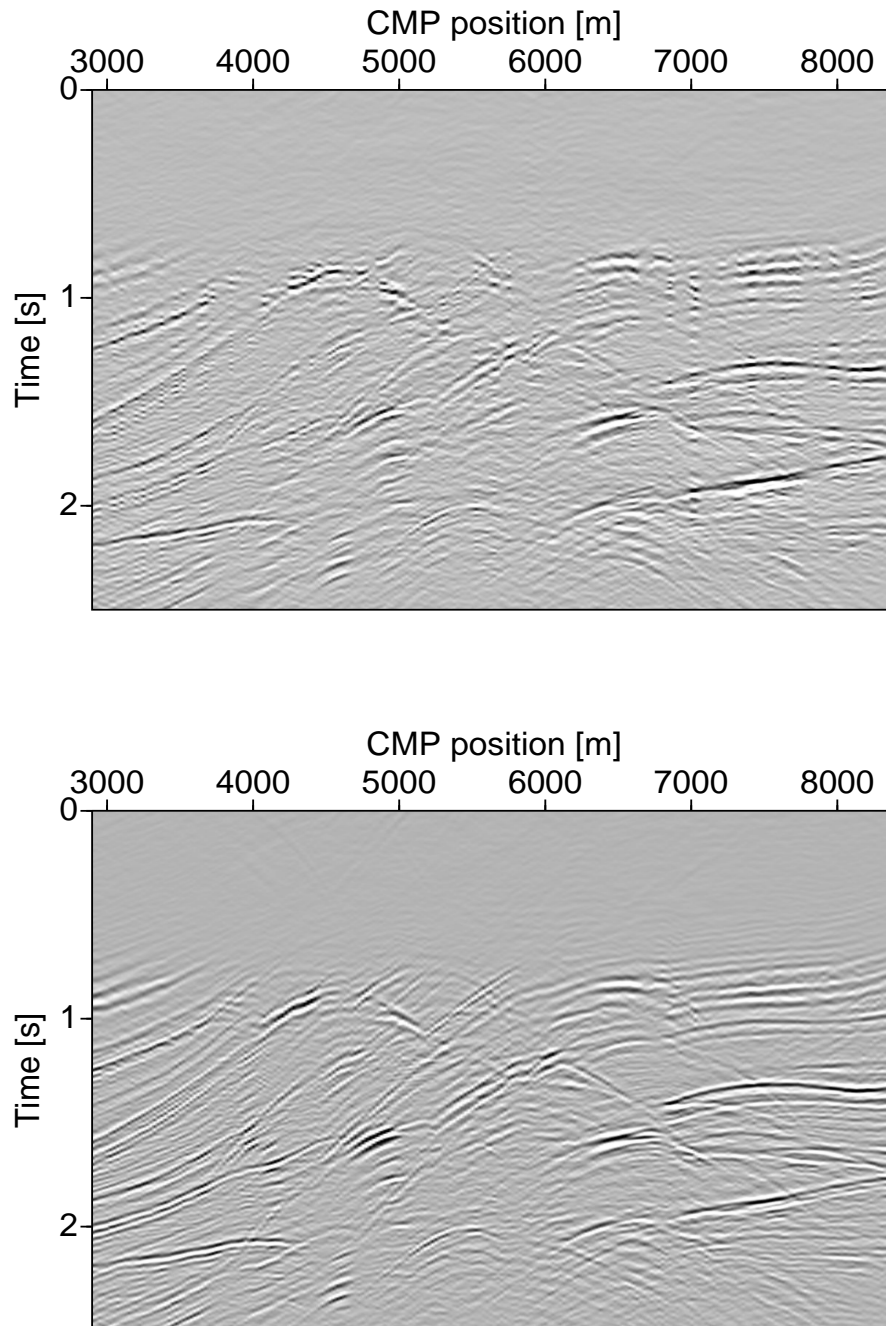
Figure 3.49: Top: Reconstructed constant offset data after one CG iteration based on the incomplete input data in Figure 3.48. Bottom: Reconstructed constant offset data after 12 CG iterations. Notice the wavefront healing effect.

# Chapter 4

# Field data example

The concept of AVP/AVA imaging/inversion is applied to a real data example. Analyzing AVP/AVA trends aids the interpretation of seismic data in relation to subsurface rock and pore-space properties. Rather than directly inverting for elastic parameters, the adopted strategy interprets the AVP/AVA response leaning upon a classification scheme that relates AVP/AVA trends and anomalies to certain reservoir types (Rutherford and Williams, 1989). This strategy is well established in 'industry-style' seismic exploration (Castagna, 1993). The seismic data have been acquired in the Gulf of Mexico and donated by Western Geophysical for testing purposes. The Gulf of Mexico is known for challenging sub-salt imaging issues. Moreover, free surface related multiples and a low primary-to-multiple energy ratio often hamper the image quality (Verschuur and Prein, 1999). Careful multiple attenuation during pre-processing is a prerequisite for AVP/AVA analysis. Furthermore, the velocity field needs to be inferred from the picked NMO stacking velocities (Dix, 1955). The pre-processed data are then analyzed with the focus on the angle behavior of a particular target reflector. The aim is to determine whether the target fits the AVP/AVA signature that is indicative of a gas bearing geologic formation. A previously conducted AVP/AVA study by Gratwick et al. (2002) identifies the reflector as a so-called class III bright spot (Rutherford and Williams, 1989). The anomaly is believed to be caused by a relatively low impedance gas bearing sand that exhibits a high amplitude anomaly on far offsets (i.e., large angles or ray parameters).

## 4.1 The Gulf of Mexico data

The provided line is located in relatively deep water (about 1400 m). The following acquisition parameters describe the initial field data set (Verschuur and Prein, 1999):

- shot numbers: 2000-3000,

- shot interval: 87.5 ft,

- number of traces per shot: 180,

- farthest offset: -15993 ft,

- nearest offset: -330 ft,

- group (receiver) spacing: 87.5 ft,

- number of samples per trace: 2404,

- time sampling 4 ms.

Figure 4.1 shows a portion of the NMO corrected and stacked data ('brute-stack'). Direct and refracted waves have been muted before NMO correction, and all distances are converted to the metric system. The area of interest is the sub-salt reflector at about 3.6 s at CMP location around 18 km. The first order ocean-bottom surface multiple is easily identified and partially masks the flat target reflector. The prominent salt body extends almost all across the shown part of the section. Together, the free surface, the ocean bottom and the top and bottom of the salt body act as a potent generator of first and higher order multiples that are often difficult to identify. The prominent first order ocean-bottom multiple is particularly troublesome for the AVP/AVA analysis of the target reflector. Thus, multiple suppression is crucial. In summary, the following processing steps were applied prior to (least-squares) migration:

- Direct and refracted wave muting,

- $\sqrt{t_{TWT}}$ scaling to approximately transform the amplitudes from point sources to lines sources (see equation (1.3.61)),
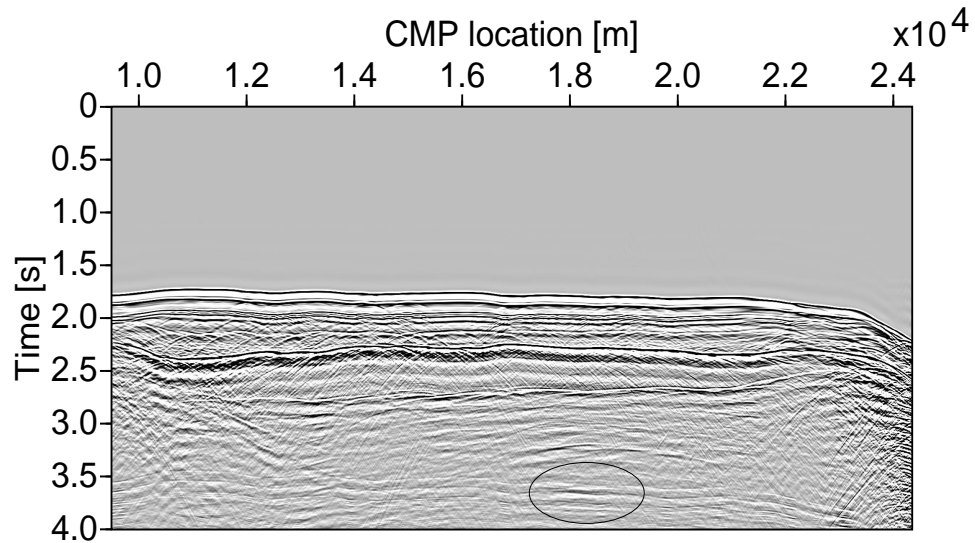
Figure 4.1: Brute-stack of the Gulf of Mexico data. The first-order ocean bottom multiple that partially masks the circled target reflector is easily identified.

- multiple suppression by high resolution parabolic Radon filtering (Sacchi and Porsani, 1999).

Figure 4.2 is the stacked section after multiple suppression. Compare the stack to the brute-stack in Figure 4.1. The flat target reflector is largely freed from multiple energy. The overlaid curves in Figure 4.2 are velocity profiles inferred from the picked stacking velocities with the help of a 'Dix inversion' algorithm (see below). In a strict sense, this type of velocity inversion is applicable only to media with no or small lateral variations. Since the area of interest does extend over the salt edges, Dix's velocity inversion is expected to work sufficiently well. The spatially interpolated velocities serve as the velocity field for the (least-squares) depth migration.

## 4.2 Velocity model building

Depth migration requires the input of a velocity model (i.e., interval velocities). The interval velocities (Figure 4.2) are obtained from the stacking velocities using a 1-D regularized least-squares 'Dix inversion'. The employed algorithm is similar to the one proposed
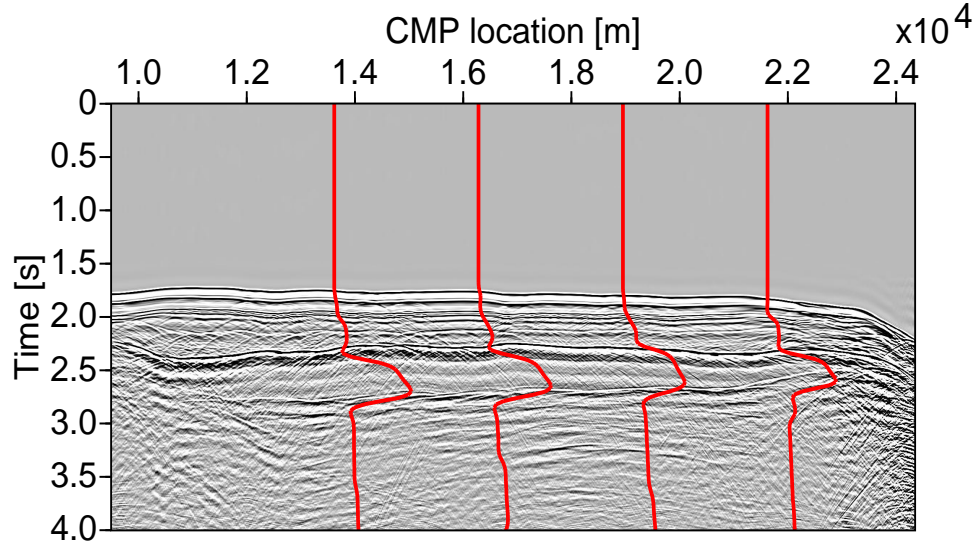
Figure 4.2: Stack after multiple suppression. The first order ocean-bottom multiple has been largely removed. The overlaid curves indicate the CMP positions where velocity profiles have been inverted. The salt body shows as a strong high velocity anomaly in the profiles.

by Lizarralde and Swift (1999) for inverting vertical seismic profile (VSP) data for interval velocities. However, in this case the forward operator is based on the linear relation between the squared stacking velocities $C^2(t)$ and the squared interval velocities $c_i^2$ (Dix, 1955):

$$C^2(t) = \frac{1}{t} \sum_{i=0}^{N-1} \Delta t_i c_i^2, . \tag{4.2.1}$$

where the time axis has been subdivided into $N-1$ equally spaced intervals $\Delta t_i$: $t = \sum_{i=0}^{N-1} \Delta t_i$. Equation (4.2.1) is simply the forward relation of Dix's well-known inversion formula for velocities in a layered medium (Dix, 1955). The forward relationship (4.2.1) is rewritten as a regularized least-squares fitting problem:

$$\min \ F(\mathbf{f}) = \|(\mathbf{d} - \underline{\mathbf{L}}\mathbf{f})\|^2 + \lambda^2 \|\underline{\mathbf{S}}\underline{\mathbf{D}}\mathbf{f}\|^2, \tag{4.2.2}$$

where $\mathbf{f}$ is the model vector with the unknown squared interval velocities, $\mathbf{d}$ is the data vector containing the stacking velocities and $\mathbf{L}$ is the summation operator in equation (4.2.1). An unregularized least-squares inversion of equation (4.2.1) is notoriously unstable for high frequency variations in the stacking velocities. Therefore the objective
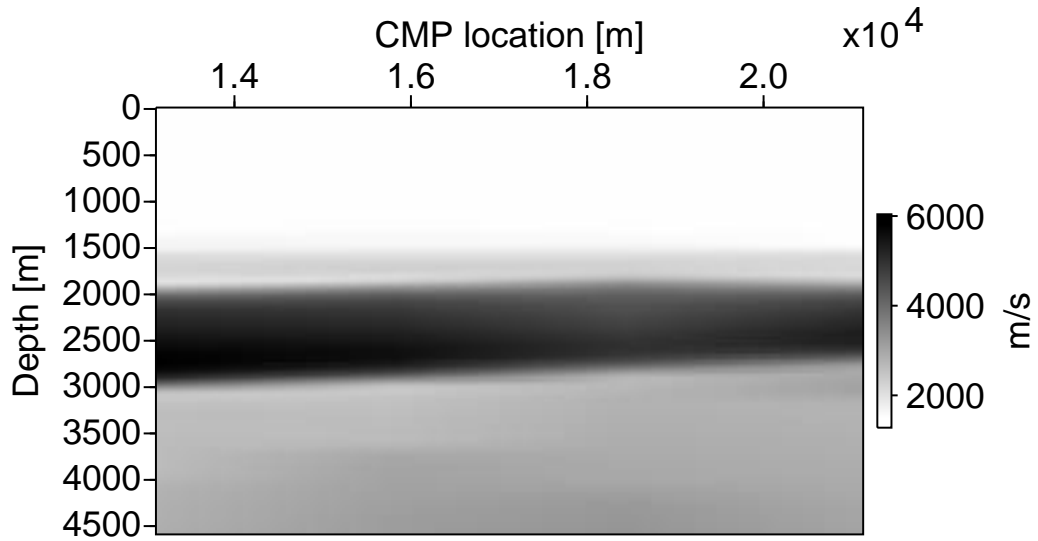
Figure 4.3: The migration velocity field obtained by spatial interpolation of the 1-D least-squares 'Dix inversion' result and time to depth conversion.

function (4.2.2) is supplemented with a regularization term that penalizes roughness in the solution. A selector operator $\underset{\sim}{S}$ complements the first-order differential operator $\underset{\sim}{D}$ in order to disable the smoothing regularization at time locations of reliable reflectors. Reflection times picked during the velocity analysis present a natural choice for the selector operator. The purpose of the selector operator is twofold. First, strong reflections imply high quality data, hence an accurate fit is desired for these locations. Second, disabling the smoothing regularization allows for the development of discontinuities in the solution and thus honors the lithologic discontinuities which lead to the reflection in the first place. As a result, the smoothing operator together with the selector operator yield a 'blocky', edge preserving, rather than a smooth solution (Lizarralde and Swift, 1999). The tradeoff parameter $\lambda$ in equation (4.2.2) determines the degree of 'blockyness'. Since the problem size is relatively small, the minimization (4.2.2) is solved by means of standard matrix inversion (Menke, 1984) rather than iterative gradient optimization. Finally, the inverted interval velocities are converted from time to depth. The inverted interval velocities for 4 selected CMP locations in Figure 4.2 show the characteristic high velocity

anomaly for the salt body. The lateral velocity variation is moderate in the area of interest, and thus justifies a linear interpolation between the inverted CMP locations (Figure 4.3).

## 4.3 AVP/AVA inversion

Both a migration and a regularized least-squares migration were carried out for the area of interest down to a depth of 4500 m. The (least-squares) split-step DSR migration used a total of 220 CMPs. The migration velocity field is mildly varying in the lateral direction, hence the efficient split-step corrected DSR operators should perform adequately.

**Migration**

Figure 4.4 depicts the stacked migration, the ray parameter CIG and a ray parameter depth slice through the flat target reflector. Apart from some apparent multiples, most events in the CIG are flat suggesting that the interval velocity field is reasonably close to the truth. Only a few sub-salt events show some residual move-out ('frowns') which indicates that the velocities have been overestimated in some parts of the model. Since the stacked migration is nevertheless of fairly good quality, the extra effort involved in oftentimes tedious velocity updating does not appear worthwhile.

The CIG and the depth slice confirm that the target reflector does indeed have the characteristic of a class III gas sand. This agrees with the findings by Gratwick et al. (2002). The amplitude increases with ray parameter, where angle and ray parameter are directly related through $p_h = \sin\theta/c$. While the amplitude trend towards larger ray parameters is unambiguous, the small ray parameters are adversely affected by the initially missing near offsets. This result exemplifies how AVP/AVA analysis can aid the assessment of a potentially gas bearing geologic structure.

**Least-squares migration**

The benefit of least-squares migration is expected to be limited, since no real data variance issues are apparent for the well sampled marine data set at hand. As seen in the synthetic data tests, migration yields good results in such cases. However, an improvement in terms of the CIG's interpretability due to ray parameter smoothing could be

achieved as demonstrated in Figure 4.5. Only 4 iterations of the least-squares algorithm have been computed, enough for the smoothing regularization to take effect. In particular, the depth slice in Figure 4.5 appears less random and emphasizes the amplitude anomaly better. Upon careful comparison of Figure 4.4 with Figure 4.5 one notices an interesting side effect of least-squares migration that has not been discussed as yet: Regularized least-squares migration attenuates internal multiples with significant residual move-out, and thus better resolves the top of the salt body in this example. Figure 4.6 zooms in on a small area from 16 km to 17 km horizontally and 1 km and 2.5 km vertically. The migration and the least-squares migration are shown side-by-side and their amplitudes have been normalized with respect to the highly reflective salt top. The least-squares migration has slightly higher resolution and images the faulted sediment structure better. The prominent first order internal salt multiple is attenuated.
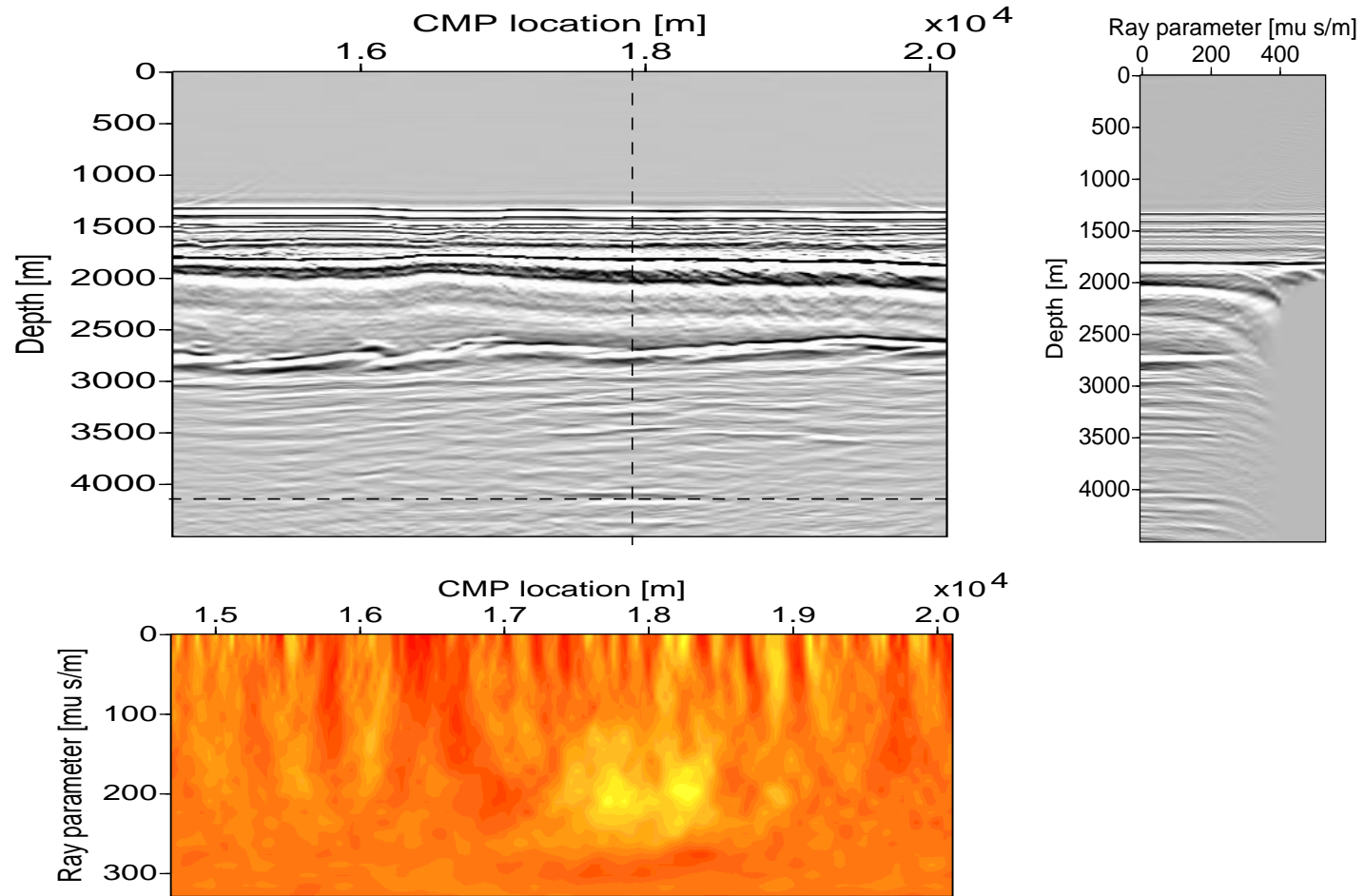
Figure 4.4: The migrated (and stacked) data, the ray parameter CIG (right) and the ray parameter depth slice through the target reflector (bottom). The vertical and the horizontal lines indicate the location of the CIG and the depth slice, respectively. The depth slice shows increasing amplitudes with angle in the area of the target reflector. The events seen in the CIG are mostly flat indicating that interval velocity estimate is fairly good. The increasing amplitude with ray parameter for the target reflector is also apparent in the ray parameter CIG.
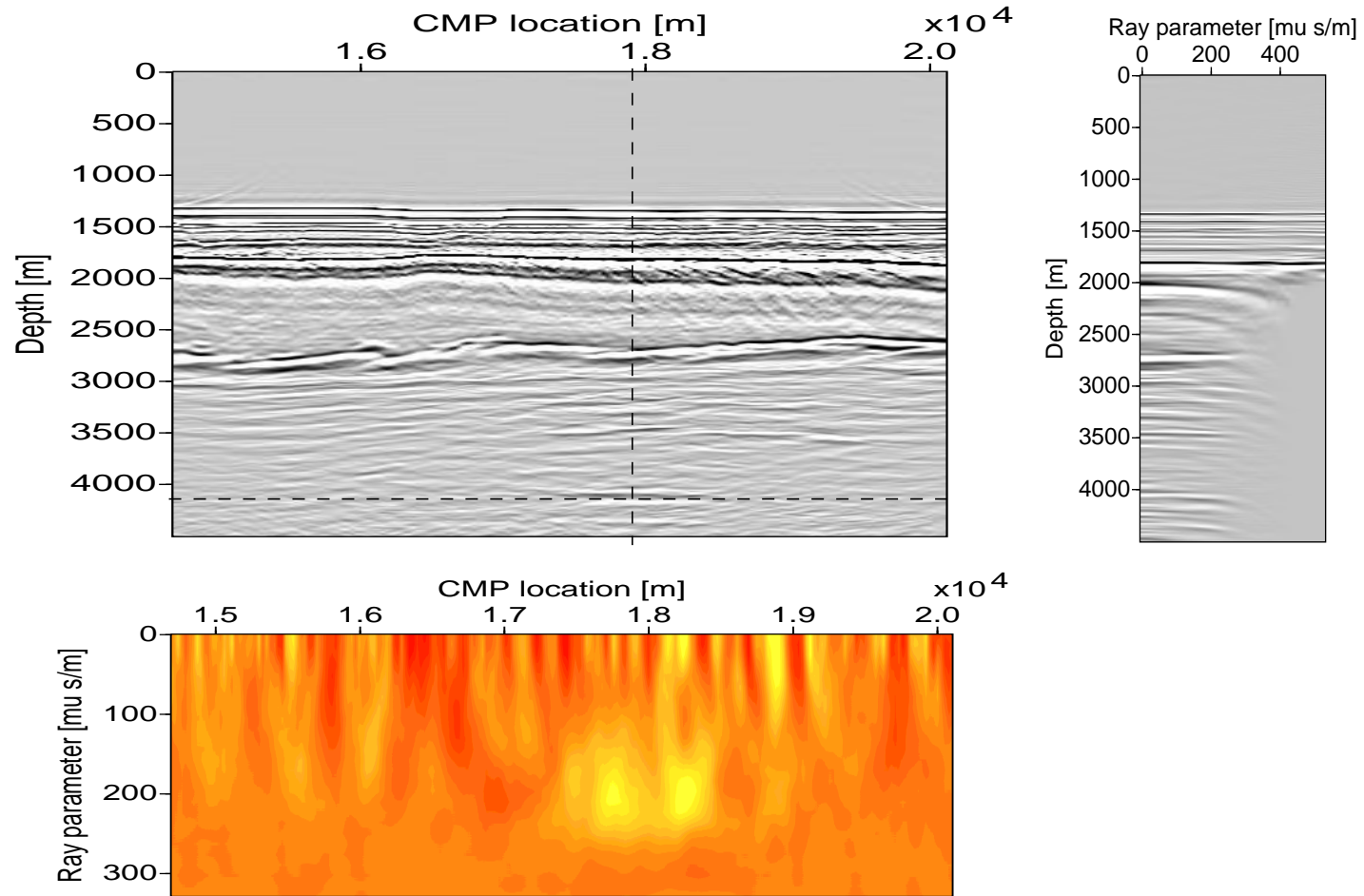
Figure 4.5: The least-squares migration after 4 iterations with moderate smoothing ($\lambda = 0.005$; $\Delta p = 14\mu s/m$). The ray parameter CIG (right) is smoother and more coherent along the ray parameter axis. The depth slice shown at the bottom reflects this as well. The increased wavelet continuity makes the computation of depth slices for AVP studies more robust. The stacked migration is very similar to Figure 4.4. Some multiple energy, especially within the salt body, is suppressed.
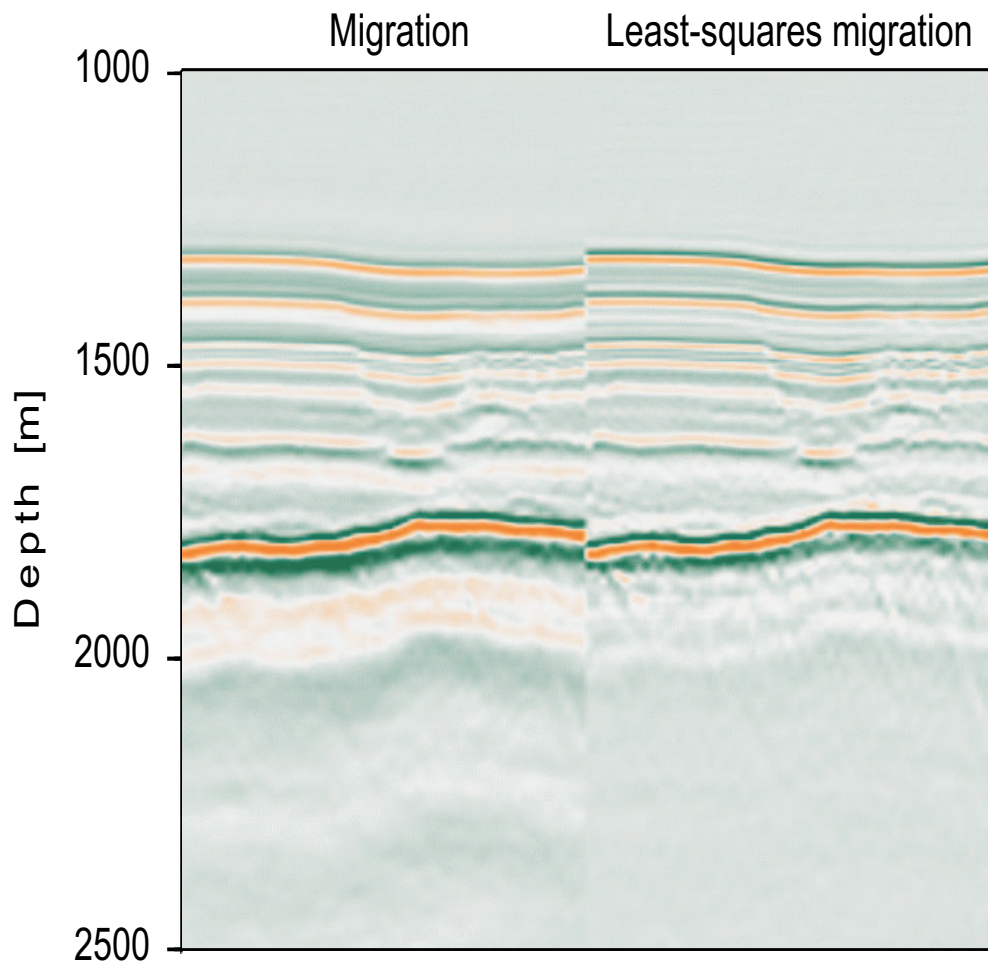
Figure 4.6: Left panel: Parts of the migrated sediment structure and the salt body ranging from 16 km to 17 km in CMP location. Right panel: Least-squares migration of the same area. The amplitudes of both sections are normalized with respect to the prominent top-salt reflector.

# Chapter 5

# Computational aspects

The computation of (generalized) DSR modelling and imaging operators is demanding in terms of number of floating point operations and memory allocation. An implementation in three spatial dimensions has not been attempted in this thesis, since even an efficient 2-D implementation of least-squares migration/inversion is a challenge. Storing full pre-stack data in the computer's memory can exceed the limits of today's computers technology. For instance, a small 2-D seismic survey with 512 midpoints, 128 offsets and 1024 time samples results in a dataset size of about 268 Mbytes. Depending on the utilized propagators (split-step propagation is more memory efficient than split-step PSPI/NSPS propagation) multiple times this memory is required to perform least-squares migration/inversion. The CG optimization can not be computed 'in-place' and temporary workspace has to be allocated to perform various computational tasks. In other words, memory efficient coding is important if larger and more realistic datasets are to be tackled. Moreover, phase-shift propagator techniques that attempt to account for lateral velocity variations make substantial use of the fast Fourier transform (FFT). Generally, the Hermitian symmetry of the complex-valued Fourier transform causes computational redundancies in terms of floating point operations and memory requirements. In practice, a combination of the FFT with the well-known real-to-complex Fourier transform is usually employed to avoid such complications (Press et al., 1997). As an alternative means to the Fourier transform the inherently real-valued, non-symmetric Hartley transform (Bracewell, 1986) is introduced into wavefield propagation (Kuehl and Sacchi, 1999; Kuehl et al., 2001). The Hartley transform automatically avoids the Hermitian sym-

metry resulting in optimized code that is comparable in efficiency to algorithms based on the real-to-complex FFT.

## 5.1 The Hartley transform

Since the seismic wavefield is real-valued, the complex Fourier transform has Hermitian symmetry. Hence, a brute force implementation leads to redundant operations and memory allocation. The Hartley transform (Bracewell, 1986) can be used to optimize such codes. The fast Hartley transform (FHT) is closely related to the complex FFT but is more suitable for real-valued data because of its inherently real-valued nature. The Hartley transform codes the amplitude and phase of a real-valued function in a single real-valued transform without symmetries. It satisfies similar theorems equivalent to those of the Fourier transform and can therefore replace the FFT in virtually any application that involves real-valued data (Bracewell, 1986). The Hartley transform has been successfully used in other geophysical applications such as wavefield modelling and data filtering (Saatcilar et al., 1990; Saatcilar and Ergintav, 1991). A complete set of fast Hartley transform algorithms is available in the literature. Here, the radix-2 decimation in time FHT is exclusively dealt with. Refer to Sorensen et al. (1985) for other implementations of the FHT.

The 1-D Hartley transform and its inverse are given by

$$
\begin{aligned}
H(u) &= \frac{1}{\sqrt{2\pi}} \int f(x)\mathrm{cas}(ux)dx, \\
f(x) &= \frac{1}{\sqrt{2\pi}} \int H(u)\mathrm{cas}(ux)du,
\end{aligned}
\tag{5.1.1}
$$

with the real-valued Hartley kernel $\mathrm{cas}(ux) = \cos(ux) + \sin(ux)$ (Bracewell, 1986). The variables $x$ and $u$ denote the conjugate Hartley variables. The orthogonal Hartley transform is related to the unitary Fourier transform and satisfies similar theorems. For seismic imaging an extension of definition (5.1.1) to higher dimensions becomes necessary. This extension is not obvious since

$$
\mathrm{cas}(ux + vy) \neq \mathrm{cas}(ux)\mathrm{cas}(vy),
\tag{5.1.2}
$$

as opposed to the Fourier kernel, which is obviously separable:

$$
\exp(i(ux + vy)) = \exp(iux)\exp(ivy).
\tag{5.1.3}
$$

116

Both sides of equation (5.1.2) are used as 2-D Hartley kernels in the literature. Here, the multiplicative definition of the 2-D Hartley transform suggested by Sundarajan (1995) is adopted and referred to as version I:

$$H_I(u,v) = \frac{1}{2\pi} \iint f(x,y)\mathrm{cas}(ux)\mathrm{cas}(vy)dxdy, \tag{5.1.4}$$

with an obvious extension to the 3-D case:

$$H_I(u,v,w) = \frac{1}{(2\pi)^{\frac{3}{2}}} \iiint f(x,y,z)\mathrm{cas}(ux)\mathrm{cas}(vy)\mathrm{cas}(wz)dxdydz. \tag{5.1.5}$$

Some authors refer to this definition as the 'cascas(cas)' transform (e.g., Bracewell (1986)). Here, for stylistic reasons, the equations (5.1.4) and (5.1.5) are called (multi-dimensional) Hartley transforms (version I), in agreement with Sundarajan (1995). Sundarajan also defines version II of the 2-D Hartley transform:

$$H_{II}(u,v) = \frac{1}{2\pi} \iint f(x,y)\mathrm{cas}(ux+vy)dxdy, \tag{5.1.6}$$

where the argument of the kernel is the sum of the arguments of the 1-D kernels. However, the definitions (5.1.4) and (5.1.5) are separable into 1-D Hartley transforms and therefore computationally more convenient to obtain than version II. Both versions of the N-dimensional Hartley transform are orthogonal (Bracewell, 1986).

Figure 5.1 to Figure 5.4 illustrate the relation between the 2-D Fourier transform and the 2-D Hartley transform (version I) for a 2-D boxcar function. This simple example demonstrates how the Hartley transform conveniently stores all amplitude and phase information in a single real-valued function.

f(x,y)
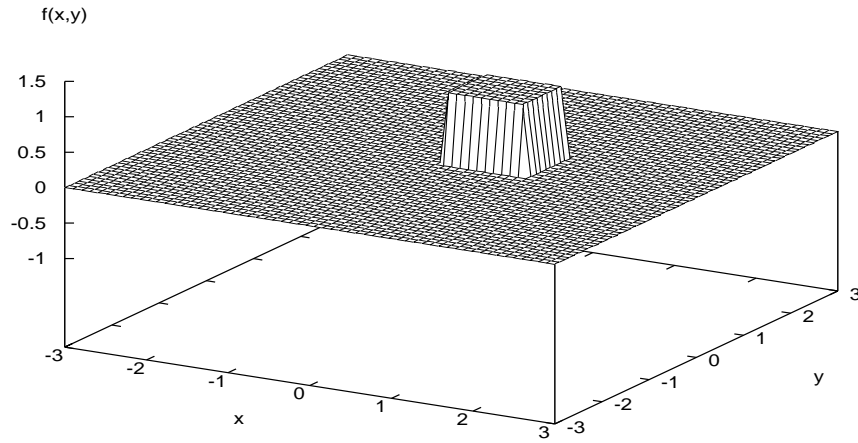
Figure 5.1: For illustration, a 2-D boxcar function is used as input for two spectral transforms: the 2-D Fourier transform and the real-valued 2-D Hartley transform (version I). The resulting spectra are shown in Figures 5.2, 5.3 and 5.4.

Re{F(u,v)}
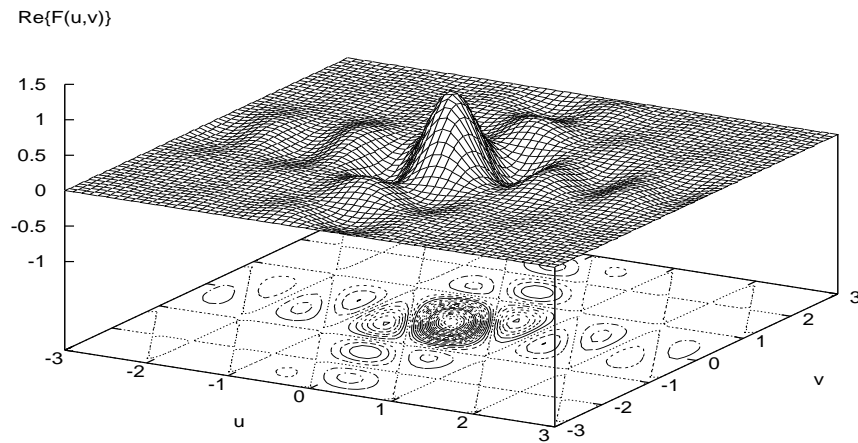
Figure 5.2: The symmetric real-part of the 2-D Fourier transform of the 2-D boxcar function in Figure 5.1.

118
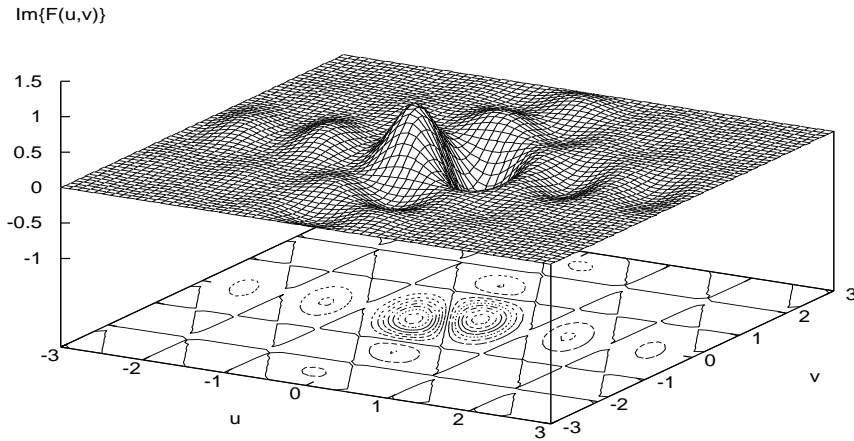
Figure 5.3: The anti-symmetric imaginary-part of the 2-D Fourier transform of the 2-D boxcar function in Figure 5.1.
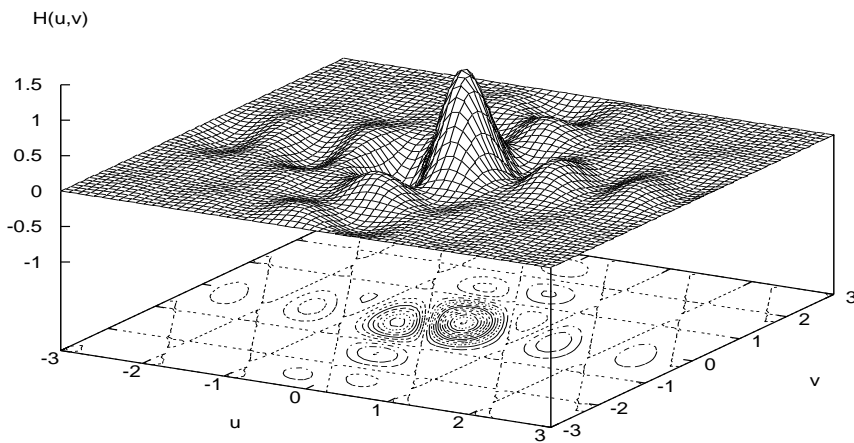


Figure 5.4: The Hartley transform of the 2-D boxcar function in Figure 5.1. The Hartley transform exhibits no symmetry and codes phase and amplitude information in a single real-valued function.
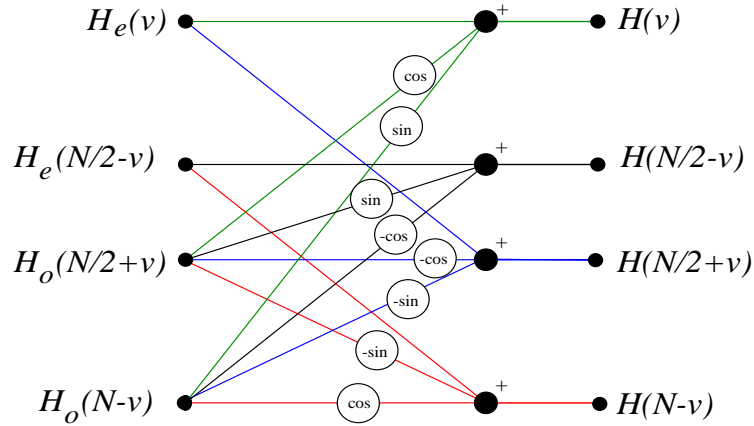
Figure 5.5: The 'Hartley butterfly' according to equation (5.1.8). The sine and cosine factors are evaluated at $\frac{2\pi}{N}\nu$, where $N$ is the length of the discrete sequence (after Sorensen et al. (1985)).

### 5.1.1 The fast Hartley transform (FHT)

In accordance with equation (5.1.1) the discrete 1-D Hartley transform (DHT) and its inverse for a length-N sequence $f(n)$, $0 \leq n \leq N - 1$, are defined by (Bracewell, 1986):

$$H(\nu) = \sum_{n=0}^{N-1} f(n) \operatorname{cas}\left(\frac{2\pi}{N}\nu n\right), \qquad 0 \leq \nu \leq N - 1,$$

$$f(n) = \frac{1}{N} \sum_{\nu=0}^{N-1} H(\nu) \operatorname{cas}\left(\frac{2\pi}{N}\nu n\right), \quad 0 \leq n \leq N - 1. \qquad (5.1.7)$$

A complete set of fast algorithms for computing the DHT can be found in Sorensen et al. (1985), including a radix-2 decimation-in-time FHT. The FHT is based on the DHT decomposition formula, which is similar to the Danielson-Lanczos formula for the discrete Fourier transform (DFT) (Press et al., 1997). A length $N = 2^M$ DHT is divided into two length-N/2 DHT's, one over the even-indexed samples $H_e$ and one over the odd-indexed samples $H_o$, and combined to form the DHT of the full-length sequence:

$$H(\nu) = H_e(\nu) + H_o(\nu) \cos\left(\frac{2\pi}{N}\nu\right) + H_o(N - \nu) \sin\left(\frac{2\pi}{N}\nu\right), \qquad (5.1.8)$$

where the indices of the half-length transforms for the even and odd indices are evaluated modulo $N/2$. The decomposition formula (5.1.8) is applied recursively until length-2
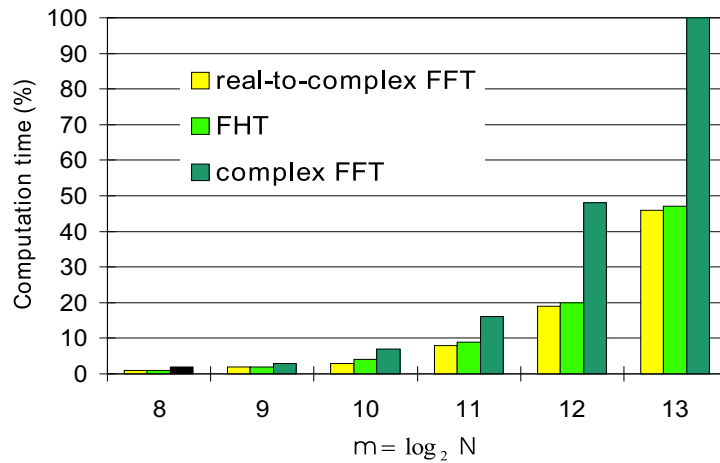
Figure 5.6: Relative computation times for the complex FFT, real-to-complex FFT and FHT as a function of the transform length $N = 2^m$. The times have been obtained on a Pentium processor.

transforms are obtained. This structure resembles the fast Fourier transform (FFT) derived by Cooley and Tukey (1965). Figure 5.5 shows a flowchart representation of equation (5.1.8), called the Hartley butterfly. Since it is desired to compute the FHT 'in place', four elements are included in each Hartley butterfly to avoid overwriting an element that will be needed later. Sorensen et al. (1985) provide a radix-2 decimation in time FHT Fortran code based on the described Hartley butterfly. They also conduct a number-of-operations count and show that, when coded efficiently, the FHT takes only a few more additions than an equivalent real-to-complex FFT. In this sense the FHT can be regarded as a means to compute a time- and memory-optimized, real-valued spectral transform. Figure 5.6 compares the computation times of the complex FFT, real-to-complex FFT and FHT obtained in a simple test using different transform lengths N. The result confirms the number-of-operations count by Sorensen et al. and demonstrates that time saving benefits over the complex FFT are increasingly significant with increasing transform lengths. The extension to higher dimensions (version I) is most easily accomplished by multiple application of the 1-D FHT along the respective dimensions without loss in efficiency. However, this is not to suggest that algorithms based on the Hartley transform are generally more efficient than those making use of the real-to-complex FFT. The Hartley transform is merely an alternative tool to the Fourier transform which might be attractive to

practitioners developing efficient algorithms that exploit the symmetries of the Fourier transform.

### 5.1.2 Wavefield propagation using Hartley transform

To make use of the Hartley transform in wavefield modelling and migration all operations need to be posed in the Hartley domain. To this end all Fourier transforms are replaced with Hartley transforms (version I). Three operations involved in modelling and migration are affected by the domain change: the complex phase-shift propagator, the split-step correction and the radial trace transform, and, of course, their respective adjoint operations. All other operations are analogous to their Fourier counterparts, the only difference being that they are real-valued. The expression for the 2-D phase-shift propagator (i.e., $k_{my} = k_{hy} = 0$) is derived in Appendix E. The Hartley domain operation that replaces the causal upward propagator $\hat{\mathcal{P}}^{(SR)}(z_{i-1}, z_i)$ in equation (1.3.44) is (Kuehl et al., 2001):

$$
\begin{aligned}
\Psi_{H_I}(k_{mx}, k_{hx}, z_{i-1}, \omega) = {} & \Psi_{H_I}(k_{mx}, k_{hx}, z_i, \omega) \cos(k_z \Delta z) \\
& + \Psi_{H_I}(k_{mx}, k_{hx}, z_i, -\omega) \sin(k_z \Delta z),
\end{aligned} \tag{5.1.9}
$$

where the wavefields are understood to be Hartley transformed over midpoint, offset and time (version I). Two real multiplications substitute the complex phase-shift operator. Adjoint downward wavefield propagation simply amounts to switching the sign in front of the sine term. The 'time-shift' theorem of the Hartley transform (Bracewell, 1986) readily transfers the 2-D version of the complex split-step correction operator $\mathcal{S}_{s_0}^{(SR)}$ in equation (1.3.52) to the Hartley domain (Kuehl et al., 2001):

$$
\begin{aligned}
\Psi_{H_I}^c(m_x, h_x, z_{i-1}, \omega) = {} & \Psi_{H_I}(m_x, h_x, z_{i-1}, \omega) \cos(\omega(\Delta s^{(S)} + \Delta s^{(R)}) \Delta z) \\
& + \Psi_{H_I}(m_x, h_x, z_{i-1}, -\omega) \sin(\omega(\Delta s^{(S)} + \Delta s^{(R)}) \Delta z),
\end{aligned} \tag{5.1.10}
$$

where the superscript $c$ signifies the split-step corrected wavefield with respect to the sources and the receivers. Again, two real operations substitute one complex multiplication and a sign change in front of the sine term yields the adjoint. The extension to split-step PSPI/NSPS propagation is straightforward. Kuehl et al. (2001) supply schematic flowcharts for angle independent split-step and split-step PSPI migration in the Hartley

domain. If angle imaging/inversion is desired the operator pair $\mathcal{A}\mathcal{I}_\omega$ and $\int d\omega \mathcal{A}'$ needs to be expressed in the Hartley domain as well.

### 5.1.3   Ray parameter modelling/imaging using Hartley transform

As it turns out, the Hartley version of ray parameter modelling and imaging $\mathcal{A}\mathcal{I}_\omega$ and $\int d\omega \mathcal{A}'$, respectively, have the same form as their Fourier counterparts. First, consider the imaging operator $\int d\omega \mathcal{A}'$ in the Fourier domain. Since the Fourier transformed wavefield $\Psi(m_x, p_{hx}, z, \omega)$ exhibits Hermitian symmetry, the final step, the summation of frequency, effectively becomes:

$$R(m_x, z, p_{hx}; \phi, \alpha) = 2 \int_0^\infty d\omega \Re\{\Psi(m_x, p_{hx}, z, \omega)\}, \tag{5.1.11}$$

where $\Re\{\Psi(m_x, p_{hx}, z, \omega)\}$ denotes the real part of the Fourier transform. Noting that

$$
\begin{aligned}
\Re\{\Psi(m_x, p_{hx}, z, \omega)\} &= \mathcal{E}\{\Psi_{H_I}(m_x, p_{hx}, z, \omega)\} \\
&= \frac{1}{2}\left[\Psi_{H_I}(m_x, p_{hx}, z, \omega) + \Psi_{H_I}(m_x, p_{hx}, z, -\omega)\right], \tag{5.1.12}
\end{aligned}
$$

where $\mathcal{E}\{\Psi_{H_I}(m_x, p_{hx}, z, \omega)\}$ is the even part of the Hartley transformed wavefield, one arrives at the imaging operator $\int d\omega \mathcal{A}'$:

$$R(m_x, z, p_{hx}; \phi, \alpha) = \int d\omega \mathcal{A}' \Psi_{H_I}(m_x, k_{hx}, z, \omega) = \int d\omega \Psi_{H_I}(m_x, k_{hx}, z, \omega)|_{k_{hx}=p_{hx}\omega}, \tag{5.1.13}$$

where all involved quantities reside again in the Hartley domain (version I). The adjoint 2-D modelling operator $\mathcal{A}\mathcal{I}_\omega$ in the Hartley domain is now straightforward:

$$\Psi_{H_I}(m_x, k_{hx}, z, \omega) = \mathcal{A}\mathcal{I}_\omega R(m_x, z, p_{hx}; \phi, \alpha) = \mathcal{I}_\omega R(m_x, z, p_{hx}; \phi, \alpha)|_{p_{hx}=k_{hx}/\omega}. \tag{5.1.14}$$

That is to say, switching from the Fourier to the Hartley domain leaves the form the modelling and imaging operators untouched.

## 5.2   Parallel computer implementation

When computed sequentially even optimized 2-D generalized DSR propagators do not yield an acceptable turnaround for least-squares migration/inversion in complex media. Fortunately, the propagators exhibit a computational structure that makes them relatively
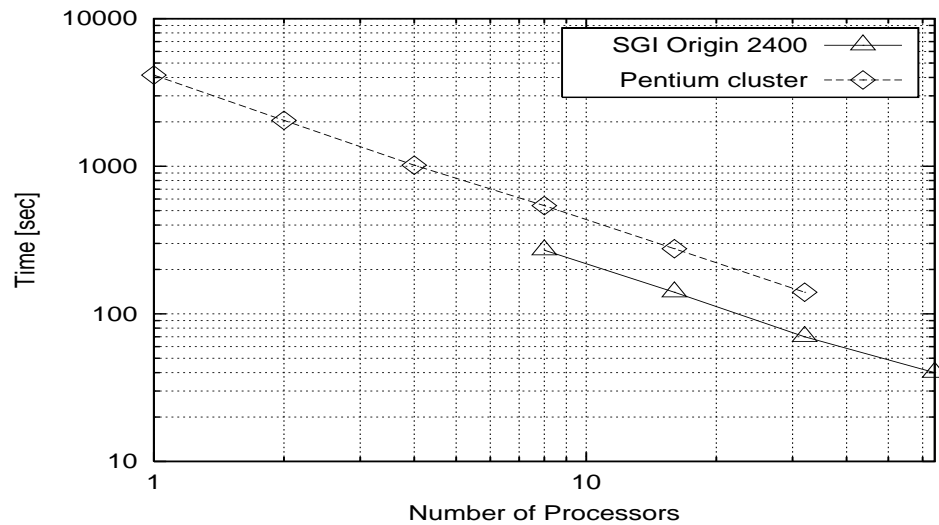
Figure 5.7: Execution times for the parallel computation of the split-step DSR migration of the Marmousi dataset (Figure 3.4). The code has been implemented in a shared-memory (SGI Origin 2400) and a distributed-memory computer architecture (Pentium cluster). Access restrictions to the SGI computer required a minimum usage of 8 processors.

easy to implement in a parallel computer architecture. Except for the operators that couple the wavefield to the reflectivity, $\mathcal{AI}_\omega$ and $\int d\omega \mathcal{A}'$, and the dot-products in the CG minimization routine in equation (2.3.2) all operations are completely separable in the frequency domain. That is, wavefield propagation does not require inter-processor communication for different frequencies. Since most of the computational time during least-squares migration is spent on wavefield propagation, this type of algorithm is suitable for both shared memory and distributed memory computing architectures. The algorithm is said to exhibit a coarse grained computational structure (low communication-to-computation ratio). A parallel implementation in either computer environment greatly improves the feasibility of least-squares migration/inversion for medium sized datasets. The 2-D split-step DSR pre-stack migration of the Marmousi dataset (Chapter 3) serves as a benchmark for a comparative test. The computation times for the pre-stack DSR migration on a Pentium cluster (distributed memory) and for an SGI Origin 2400 (shared memory) are graphed in Figure 5.7. The overall turnaround on the Pentium cluster is about two times slower than on the SGI. Clearly, both implementations scale nicely for the tested number of processors.

# Discussion and Conclusion

The goal of seismic imaging is to invert the seismic surface data for the reflectivity of the geologic subsurface structures. To make the non-linear inverse problem tractable geophysicists usually decompose the inversion into several linear sub-process. This decomposition entails inevitable simplifications of the underlying physics of wave motion. Many different schemes, ranging from simple NMO correction followed by AVO analysis to sophisticated tomographic inversion and 3-D pre-stack depth migration, have been devised to tackle the inverse problem. The complexity of the geologic environment to be investigated, the data quality, economical considerations and other factors influence which scheme is the most appropriate for a particular imaging/inversion project. Simplifications are often motivated by necessity because of limited computer power. More importantly, perhaps, a break down into linear sub-processes adds flexibility, control and robustness to the inversion. It is the task of the geophysicist to find a pertinent compromise between feasibility and fidelity to the nature of wave propagation and scattering. If the angle dependent reflectivity inversion fails, it should fail gracefully rather than catastrophically with respect to the invoked simplifications. For instance, the fact that depth migration yields useful structural images also when the observed angle dependence does not agree with a specular reflection process is invaluable to migration/inversion in complex media.

In this thesis, linearized seismic wave-equation imaging/inversion has been cast into the least-squares inversion framework. This is an instructive approach to inversion, since it yields both formulas that approximate the least-squares solution and iterative least-squares algorithms that make use of well developed optimization techniques. Clearly, the latter is computationally more demanding but also opens the opportunity to regularize the least-squares solution. Furthermore, if the seismic data have significant variance

least-squares migration is able to account for that. Regularized least-squares inversion has proven to be beneficial in many other geophysical applications. Successful examples are the 1-D impedance inversion and the high resolution Radon transform. It is therefore conceivable that also least-squares migration/inversion will be practically relevant. Ray parameter dependent common image gathers are an excellent domain for model space regularization. Penalizing roughness in the reflection ray parameter CIGs helps to retrieve solutions that are physically sensible. The logic behind the smoothing regularization is based on the notion that discontinuities or rapid amplitude changes along ray parameter/angle stem from numerical imaging artifacts and acquisition footprint noise. The reflection angle dependence is preserved, since it is slowly varying.

The theory of least-squares migration for AVP/AVA migration/inversion has been presented for 3-D acoustic media. This thesis favors one-way wavefield propagators over ray theoretical Green's functions, since propagators handle the seismic wavefield with greater generality. They inherently account for multi-pathing and treat caustics properly, features that are difficult to honor with the high frequency approximation of the wave-equation.

In a strict sense, the proposed algorithm is applicable only to compressional seismic waves. The synthetic data examples invert for a fluid-fluid AVP/AVA characteristic. The real earth, on the other hand, is elastic and Zoeppritz's equation for specular PP reflections governs the reflection angle dependence of compressional waves. However, this does not affect the concept of regularized least-squares migration nor does it change the algorithm itself when applied to compressional seismic data. One simply has to be aware of it. Most seismic surveys record predominantly compressional wave energy and an extension to the full elastic case has not been considered here. In practical terms, such an extension would amount to a wavefield separation into compressional and shear wave constituents and subsequent independent AVP/AVA migration/inversion.

The regularized least-squares migration/inversion has been extensively tested with the help of 2-D synthetic data examples. These tests are important, since the adopted primary data representation is known to have limitations that can compromise the inversion result. The primary representation does not account for transmission loss and fine structure filtering effects due to multiple scattering. Hence, inversion based on this repre-

sentation works best in media with small to moderate medium contrast. The tested sub-surface models range from simple to complex, with mostly small to moderate reflection coefficients. The results underscore that regularized least-squares migration performs as expected within its theoretical limitations. It is found that least-squares wave-equation migration can retrieve AVP/AVA functions that, despite inevitable finite aperture effects, are close to the true AVA. In all examples, the smoothness constraint proves particularly beneficial when the seismic data are compromised by incompleteness. Acquisition foot-print effects in terms of kinematic artifacts and amplitude distortion in the ray parameter CIGs could be successfully mitigated in regularized least-squares migration.

In spite of the good results, it must be acknowledged that the AVP/AVA estimate obtained from migration is comparable to that of costly least-squares migration provided the imaging Jacobian is considered, the medium is moderately complex and the seismic wavefield is optimally sampled. Contingent on the above points, migration is likely to be the method of choice. This also implies that if a reliable data reconstruction of incomplete data prior to migration is possible, least-squares migration may be replaced with data reconstruction followed by amplitude scaled migration (Duijndam et al., 2000). There exists a variety of data reconstruction (interpolation) techniques (e.g., Duijndam et al. (1999)). However, for sparse data in complex media data interpolation tends to be unreliable, while regularized least-squares migration/inversion has the advantage of a model constraint that enhances robustness and gives good results even for very sparse data. Data interpolation schemes, in general, lack a comparable physical regularization constraint. Therefore, they are likely to be less robust under very sparse conditions. A systematic comparison of data reconstruction versus least-squares migration is beyond the scope of this thesis, albeit desirable in the future.

The synthetic data tests are confirmed by the 2-D field data example. The dataset is from the Gulf of Mexico and exemplifies a typical sub-salt imaging situation. The target is a potentially gas bearing sand whose AVA is characterized by an increase in the reflection amplitude with angle. The marine data are well sampled and have no apparent data variance issue. While the expected AVP/AVA trend could be well reproduced with conventional migration, the least-squares migration CIGs are smoother and more interpretable. Some multiple energy could be attenuated as well. This is a promising

result, but much more experience with sparser and more challenging datasets needs to be gathered in order to better assess the benefits of regularized least-squares migration for real-world data.

Dense wavefield sampling is typical for marine data. Data acquired on land is often significantly more irregular. The incomplete data issue is particularly troublesome when imaging/inversion is to be carried out in three spatial dimensions. This is because of the often encountered sparseness and irregularity of 3-D seismic surveys owing to economical and practical reasons. It is expected that least-squares migration becomes particularly beneficial in such cases. Unfortunately, a computer implementation of the 3-D least-squares wave-equation migration is a major obstacle. The 3-D phase-shift type propagators that are amended for complex media make substantial use of 4-D Fourier transforms. A time-efficient computation of these is at the limit of today's computer technology. Efficiency is paramount, since geophysicists demand a fast turnaround in order to conduct parameter and performance tests that allow them to develop effective processing strategies. The real-valued Hartley transform as an alternative to the complex valued Fourier transform has been employed to optimize the computation of the wavefield operators. However, the Hartley transform must be regarded as a mere alternative and does not entail an optimization level that can not be achieved with Fourier transform techniques. Fortunately, the 2-D implementation in a parallel computer environment (shared or distributed memory) yields excellent speed-up performance. It is therefore only a matter of time before a parallel 3-D implementation of (least-squares) wave-equation migration becomes feasible. The regularized least-squares approach is expected to unfold its full potential in 3-D seismology.

# References

Aki, K., and Richards, P. G., 1980, Quantitative Seismology: Theory and Methods: W. H. Freeman and Co.

Alkhalifah, T., 2000, Prestack phase-shift migration of separate offsets: Geophysics, **65**, no. 4, 1179–1194.

Aminzadeh, F., Burkhard, N., Rocca, F., and Wyatt, K., 1994, SEG/EAEG 3-D modeling project: 2nd update: The Leading Edge, **13**, no. 09, 949–952.

Bagaini, C., Bonomi, E., and Pieroni, E., 1995, Data parallel implementation of 3-D PSPI: 65th Ann. Internat. Mtg., Soc. of Expl. Geophys., Expanded Abstracts, pages 188–191.

Baysal, E., Kosloff, D. D., and Sherwood, J. W. C., 1984, A two-way nonreflecting wave equation: Geophysics, **49**, no. 02, 132–141.

Berkhout, A. J., and Wapenaar, C. P. A., 1990, Delphi: Delft philosophy on acoustic and elastic inversion: The Leading Edge, **09**, no. 02, 30–33.

Beydon, W. B., and Keho, T. H., 1987, The paraxial ray method: Geophysics, **52**, no. 12, 1639–1653.

Biondi, B., and Sava, P., 1999, Wave-equation migration velocity analysis: 69th Ann. Internat. Mtg., Soc. of Expl. Geophys., Expanded Abstracts, pages 1723–1726.

Biondo, B., and Palacharla, G., 1996, 3-D prestack migration of common-azimuth data: Geophysics, **61**, no. 06, 1822–1832.

Bleistein, N., and Handelsman, R. A., 1986, Asymptotic expansions of integrals: Dover Publications Inc.

Bleistein, N., Cohen, J., and Stockwell, J., 2001, Mathematics of Multidimesional Seismic Imaging, Migration, and Inversion: Springer-Verlag.

Bracewell, R., 1986, The Hartley transform: Oxford University Press.

Bronstein, I., Semendjajew, K., Musiol, G., and Mühlig, H., 1997, Taschenbuch der Mathematik: Verlag Harri Deutsch, Frankfurt am Main.

Canning, A., and Gardner, G. H. F., 1998, Reducing 3-D acquisition footprint for 3-D DMO and 3-D prestack migration: Geophysics, **63**, no. 04, 1177–1183.

Castagna, J. P., 1993, AVO analysis - tutorial and review, *in* Backus, M. M., Ed., Offset-dependent reflectivity - theory and practice of AVO analysis: Soc. of Expl. Geophys., 3–36.

Cerveny, V., 1985, The application of ray tracing to the numerical modeling of seismic wavefields in complex structure, *in* Dohr, G., Ed., Seismic shear waves (part A: Theory): Soc. of Expl. Geophys., 1–124.

Claerbout, J. F., and Nichols, D., 1994, Spectral preconditioning: Stanford Exploration Project, **SEP-82**, 183–186.

Claerbout, J. F., 1971, Toward a unified theory of reflector mapping: Geophysics, **36**, no. 03, 467–481.

Claerbout, J. F., 1985, Imaging the Earth's Interior: Blackwell Scientific Publications.

Claerbout, J. F., 1992, Earth Soundings Analysis: Processing versus Inversion: Blackwell Scientific Publications.

Clayton, R. W., and Engquist, B., 1990, Absorbing boundary conditions for acoustic and elastic wave equations, *in* Marfurt, K. J., Ed., Numerical modeling of seismic wave propagation: Soc. of Expl. Geophys., 448–459.

Clayton, R. W., and Stolt, R. H., 1981, A Born-WKBJ inversion method for acoustic reflection data: Geophysics, **46**, no. 11, 1559–1567.

Cooley, J., and Tukey, J., 1965, An algorithm for the machine calculation of complex Fourier series: Math. Comput., **19**, no. 2, 297–301.

de Bruin, C. G. M., Wapenaar, C. P. A., and Berkhout, A. J., 1990, Angle-dependent reflectivity by means of prestack migration: Geophysics, **55**, no. 09, 1223–1234.

Dix, C. H., 1955, Seismic velocities from surface measurements: Geophysics, **20**, no. 01, 68–86.

Duijndam, A. J. W., Schonewille, M. A., and Hindriks, C. O. H., 1999, Reconstruction of band-limited signals, irregularly sampled along one spatial direction:, **64**, no. 2, 524–538.

Duijndam, A., Volker, A., and Zwartjes, P., 2000, Reconstruction as efficient alternative for least-squares migration: 70th Ann. Internat. Mtg., Soc. of Expl. Geophys., Expanded Abstracts, pages 1012–1015.

Duijndam, A. J. W., 1988, Bayesian estimation in seismic inversion part I - principles: Geophys. Prosp., **36**, no. 08, 878–898.

Duquet, B., Marfurt, K. J., and Dellinger, J., 2000, Kirchhoff modeling, inversion for reflectivity, and subsurface illumination: Geophysics, **65**, no. 4, 1195–1209.

Ferguson, R. J., and Margrave, G. F., 2002, Prestack depth migration by symmetric non-stationary phase-shift: Geophysics, **67**, 594–603.

Gazdag, J., and Sguazzero, P., 1984, Migration of seismic data by phase-shift plus interpolation: Geophysics, **49**, no. 02, 124–131.

Gazdag, J., 1978, Wave equation migration with the phase-shift method: Geophysics, **43**, no. 07, 1342–1351.

Gratwick, D., Sava, P., and Biondi, B., 2002, AVA by Wave Equation Imaging: The Leading Edge, **submitted**.

Gray, S. H., and May, W. P., 1994, Kirchoff migration using eikonal equation traveltimes: Geophysics, **59**, no. 05, 810–817.

Gray, S. H., 1997, True-amplitude seismic migration: A comparison of three approaches: Geophysics, **62**, no. 03, 929–936.

Grimbergen, J. L. T., Dessing, F. J., and Wapenaar, K., 1998, Modal expansion of one-way operators in laterally varying media: Geophysics, **63**, no. 03, 995–1005.

Hestenes, M., and Stiefel, E., 1952, Methods of conjugate gradients for solving linear systems: Nat. Bur. Standards J. Res., **49**, 403–436.

Kessinger, W., 1992, Extended split-step Fourier migration: 62nd Ann. Internat. Mtg., Soc. of Expl. Geophys., Expanded Abstracts, pages 917–920.

Kitchenside, P. W., 1991, Phase-shift based migration for transverse isotropy: 61st Ann. Internat. Mtg., Soc. of Expl. Geophys., Expanded Abstracts, pages 993–996.

Kosloff, D. D., and Baysal, E., 1983, Migration with the full acoustic wave equation: Geophysics, **48**, no. 06, 677–687.

Kuehl, H., and Sacchi, M. D., 1999, Least-squares split-step migration using the Hartley transform: 69th Ann. Internat. Mtg., Soc. of Expl. Geophys., Expanded Abstracts, pages 1548–1551.

Kuehl, H., and Sacchi, M. D., 2001a, Separable offset least-squares DSR migration of incomplete data: CSEG National Convention 2001.

——— 2001b, Split-step WKBJ migration/inversion of incomplete data: 5th SEGJ International Symposium - Imaging Technology.

Kuehl, H., and Sacchi, M. D., 2002, Least-squares wave equation migration for AVP/AVA inversion: Geophysics, **accepted**.

Kuehl, H., Sacchi, M. D., and Fertig, J., 2001, The Hartley transform in seismic imaging: Geophysics, **66**, no. 4, 1251–1257.

Lambare, G., Virieux, J., Mandariaga, R., and Jin, S., 1992, Iterative asymptotic inversion in the acoustic approximation: Geophysics, **57**, no. 09, 1138–1154.

Lay, T., and Wallace, T. C., 1995, Modern Global Seismology: Academic Press, Inc.

Le Rousseau, J. H., 1997, Depth migration in heterogeneous, transversely isotropic media with the phase-shift-plus-interpolation method: 67th Ann. Internat. Mtg., Soc. of Expl. Geophys., Expanded Abstracts, pages 1703–1706.

LeBras, R., and Clayton, R. W., 1988, An iterative inversion of back-scattered acoustic waves: Geophysics, **53**, no. 04, 501–508.

Lee, D., Mason, I. M., and Jackson, G. M., 1991, Split-step Fourier shot-record migration with deconvolution imaging: Geophysics, **56**, no. 11, 1786–1793.

Lizarralde, D., and Swift, S., 1999, Smooth inversion of VSP traveltime data: Geophysics, **64**, no. 3, 659–661.

Margrave, G. F., and Ferguson, R. J., 1999, Wavefield extrapolation by nonstationary phase shift: Geophysics, **64**, no. 04, 1067–1078.

Menke, W., 1984, Geophysical Data Analysis: Discrete Inverse Theory: Academic Press, Inc.

Mosher, C., and Foster, D., 2000, Common angle imaging conditions for prestack depth migration: 70th Ann. Internat. Mtg., Soc. of Expl. Geophys., Expanded Abstracts, pages 830–833.

Mosher, C. C., Keho, T. H., Weglein, A. B., and Foster, D. J., 1996, The impact of migration on AVO: Geophysics, **61**, no. 06, 1603–1615.

Mosher, C. C., Foster, D. J., and Hassanzadeh, S., 1997, Common angle imaging with offset plane waves: 67th Ann. Internat. Mtg., Soc. of Expl. Geophys., Expanded Abstracts, pages 1379–1382.

Nemeth, T., Wu, C., and Schuster, G. T., 1999, Least-squares migration of incomplete reflection data: Geophysics, **64**, no. 1, 208–221.

O'Brien, M. J., and Gray, S. H., 1996, Can we image beneath salt?: The Leading Edge, **15**, no. 01, 17–22.

Ottolini, R., and Claerbout, J. F., 1984, The migration of common-midpoint slant stacks: Geophysics, **49**, no. 03, 237–249.

Popovici, A. M., 1995, Migration to zero-offset, Ph.D. thesis: Stanford Exploration Project.

Popovici, A. M., 1996, Prestack migration by split-step DSR: Geophysics, **61**, no. 05, 1412–1416.

Press, W., Flannery, B., Teukolsky, S., and Vetterling, W., 1997, Numerical recipes in C: Cambridge University Press.

Prucha, M., Biondi, B., and Symes, W., 1999, Angle-domain common image gathers by wave-equation migration: 69th Ann. Internat. Mtg., Soc. of Expl. Geophys., Expanded Abstracts, pages 824–827.

Rickett, J., 2001, Model-space vs. data-space normalization for finite-frequency depth migration: 71st Ann. Internat. Mtg., Soc. of Expl. Geophys., Expanded Abstracts, pages 2081–2084.

Ristow, D., and Rühl, T., 1994, Fourier finite-difference migration: Geophysics, **59**, no. 12, 1882–1893.

Rutherford, S. R., and Williams, R. H., 1989, Amplitude-versus-offset variations in gas sands: Geophysics, **54**, no. 06, 680–688.

Saatcilar, R., and Ergintav, S., 1991, Solving the elastic wave equations with the Hartley transform method: Geophysics, **56**, 274–278.

Saatcilar, R., Ergintav, S., and Canitez, N., 1990, The use of Hartley transform in geophysical applications:, **55**, no. 11, 1488–1495.

Sacchi, M., and Porsani, M., 1999, Fast high-resolution parabolic radon transform: 67th Ann. Internat. Mtg., Soc. of Expl. Geophys., Expanded Abstracts, pages 1477–1480.

Sava, P., Biondi, B., and Fomel, S., 2001, Amplitude-preserved common image gathers by wave-equation migration: 71st Ann. Internat. Mtg., Soc. of Expl. Geophys., Expanded Abstracts, pages 296–299.

Scales, J. A., 1987, Tomographic inversion via the conjugate gradient method: Geophysics, **52**, 179–185.

Scales, J. A., 1997, Theory of Seismic Imaging: Samizdat Press.

Sorensen, H., Jones, D., Burrus, S., and Heideman, M., 1985, On Computing the Discrete Hartley Transform: IEEE Transactions on Acoustics, Speech and Signal Processing, **vol. ASSP-33**, no. 4, 1231–1238.

Stoffa, P. L., Fokkema, J. T., de Luna Freire, R. M., and Kessinger, W. P., 1990, Split-step fourier migration:, **55**, no. 04, 410–421.

Stolt, R. H., and Benson, A. K., 1986, Seismic migration: Theory and practice: Handbook of Geophysical Exploration, Vol. 5, Geophysical Press.

Stolt, R. H., and Weglein, A. B., 1985, Migration and inversion of seismic data: Geophysics, **50**, no. 12, 2458–2472.

Strang, G., 1986, Introduction to Applied Mathematics: Wellesley-Cambridge Press.

Sundarajan, N., 1995, 2-D Hartley transforms: Geophysics, **60**, no. 2, 262–267.

Tarantola, A., 1987, Inverse Problem Theory: Methods for data fitting and model parameter estimation: Elsevier Science Publishing Company Inc.

Ursin, B., 1983, Review of elastic and electromagnetic wave propagation in horizontally layered media: Geophysics, **48**, no. 8, 1063–1081.

Verschuur, D. J., and Prein, R. J., 1999, Multiple removal results from Delft University: The Leading Edge, **18**, no. 1, 86–91.

Versteeg, R., 1994, The Marmousi experience: Velocity model determination on a synthetic complex data set: The Leading Edge, **13**, no. 09, 927–936.

Vestrum, R. W., Lawton, D. C., and Schmid, R., 1999, Imaging structures below dipping TI media: Geophysics, **64**, no. 4, 1239–1246.

Wapenaar, C. P. A., and Berkhout, A., 1989, Elastic wavefield extrapolation: Elsevier Science Publishing Company Inc.

Wapenaar, C. P. A., and Grimbergen, J. L. T., 1996, Reciprocity theorems for one-way wavefields: Geophys. J. Int., **127**, 169–177.

Wapenaar, C. P. A., and Herrmann, F. J., 1996, True-amplitude migration taking fine layering into account: Geophysics, **61**, no. 03, 795–803.

Wapenaar, C. P. A., Kinneging, N. A., and Berkhout, A. J., 1987, Principle of prestack migration based on the full elastic two-way wave equation: Geophysics, **52**, no. 02, 151–173.

Wapenaar, C. P. A., Herrmann, P., Verschuur, D. J., and Berkhout, A. J., 1990, Decomposition of multicomponent seismic data into primary P- and S-wave responses: Geophys. Prosp., **38**, no. 06, 633–662.

Wapenaar, C. P. A., Van Wijngaarden, A. J., van Geloven, W., and van der Leij, T., 1999, Apparent AVA effects of fine layering: Geophysics, **64**, no. 6, 1939–1948.

Wapenaar, C. P. A., 1996, Inversion versus migration: A new perspective to an old discussion: Geophysics, **61**, no. 03, 804–814.

Wapenaar, C., 1998, Short Note - Reciprocity properties of one-way propagators: Geophysics, **63**, no. 05, 1795–1798.

Weglein, A. B., and Stolt, R. H., 1999, Migration-inversion revisited (1999): The Leading Edge, **18**, no. 8, 950–952.

Wu, R. S., 1996, Synthetic seismograms in heterogeneous media by one-return approximation: Pure and Applied Geophys., **148**, 155–173.

Xu, S., Chauris, H., Lambare, G., and Noble, M. S., 1998, Common angle image gather: A new strategy for imaging complex media: 68th Ann. Internat. Mtg., Soc. of Expl. Geophys., Expanded Abstracts, pages 1538–1541.

Yilmaz, O., and Chambers, R., 1984, Migration velocity analysis by wave field extrapolation: Geophysics, **49**, 1664–1674.

Zheng, Y., Gray, S., Cheadle, S., and Anderson, P., 2001, Factors affecting AVO analysis of prestack migrated gathers: 71st Ann. Internat. Mtg., Soc. of Expl. Geophys., Expanded Abstracts, pages 989–992.

# Appendix A

# High frequency approximation

Consider the source-free acoustic wave-equation (1.1.8) for constant density:

$$\nabla^2 p(\mathbf{x}, t) - \frac{1}{c^2} \frac{\partial^2 p(\mathbf{x}, t)}{\partial t^2} = 0, \tag{A.0.1}$$

where the velocity $c$ is slowly varying. Assuming a time harmonic wavefield,

$$p(\mathbf{x}, t) = e^{i\omega t} p(\mathbf{x}), \tag{A.0.2}$$

one arrives at the reduced wave-equation or Helmholtz equation:

$$\left( \nabla^2 + \frac{\omega^2}{c^2} \right) p(\mathbf{x}) = 0. \tag{A.0.3}$$

In the ray theoretical approach one seeks a solution of the form $p(\mathbf{x}) = A(\mathbf{x}) e^{i\omega\tau(\mathbf{x})}$, where $\tau$ is called the eikonal, $A(\mathbf{x})$ is the slowly varying amplitude and the frequency $\omega$ is assumed to be large (high frequency approximation). Upon inserting this ansatz one finds:

$$\left( \omega^2 \left( \frac{1}{c^2} - (\nabla\tau)^2 \right) A + 2i\omega \nabla A \cdot \nabla\tau + i\omega \nabla^2\tau A + \nabla^2 A \right) e^{i\omega\tau} = 0. \tag{A.0.4}$$

This condition is approximately satisfied if:

$$(\nabla\tau)^2 = \frac{1}{c^2} = s^2, \tag{A.0.5}$$

which is the eikonal equation, and

$$A\nabla^2\tau + 2\nabla\tau \cdot \nabla A = 0, \tag{A.0.6}$$

which is the transport equation. The high frequency approximation is violated where amplitudes have a strong spatial dependence as in the vicinity of velocity discontinuities

or at focal points or caustics (Cerveny, 1985). Ray-tracing finds the trajectories that are perpendicular to the wavefronts defined by $\tau = const.$:

$$\frac{d\mathbf{r}}{ds} = c\nabla\tau, \tag{A.0.7}$$

where $s$ is the arc length of the ray and $\mathbf{r}$ is the ray vector. It is convenient to introduce the slowness vector $\mathbf{p} = \frac{1}{c}\frac{d\mathbf{r}}{ds}$ that has magnitude $|\mathbf{p}| = \frac{1}{c} = s$ and is tangential to the ray. The ray trajectories are found by (numerically) integrating a system of first order equations (ray-tracing system) (Cerveny, 1985):

$$\frac{d\mathbf{r}}{ds} = c\mathbf{p} \text{ and } \frac{d\mathbf{p}}{ds} = \nabla\frac{1}{c}. \tag{A.0.8}$$

Since

$$\nabla\tau\frac{1}{c} \cdot \frac{d\mathbf{r}}{ds} = \frac{1}{c^2}, \text{ or } \frac{d\tau}{ds} = \frac{1}{c}, \tag{A.0.9}$$

integration along the ray solution yields the eikonal (i.e., travel-time):

$$\tau(s) = \tau(s_0) + \int_{s_0}^{s} \frac{1}{c(s')}ds'. \tag{A.0.10}$$

The transport equation (i.e., amplitude) is solved by means of dynamic ray-tracing (Cerveny, 1985). Dynamic ray-tracing finds the local wavefront curvature about the central ray up to the second order (parabolic wavefront). The first order corresponds to a local plane wave approximation and gives rise to the relationship between slowness, wavenumber and temporal frequency:

$$\mathbf{p} = \frac{\mathbf{k}}{\omega}. \tag{A.0.11}$$

Dynamic ray-tracing also allows for the extrapolation of travel-time information with respect to the central ray. Figure A.1 and Figure A.2 illustrate numerical ray-tracing and travel-time extrapolation based on the second order approximation, respectively, for the Marmousi velocity model. In Kirchhoff migration/inversion the Green's functions are of the form:

$$G(\mathbf{x}, \mathbf{x}') = A(\mathbf{x}, \mathbf{x}')e^{i\omega\tau(\mathbf{x},\mathbf{x}')}, \tag{A.0.12}$$

where the amplitude $A(\mathbf{x}, \mathbf{x}')$ is the solution of the transport equation for a point source at $\mathbf{x}'$ and $\tau(\mathbf{x}, \mathbf{x}')$ is the corresponding travel-time.
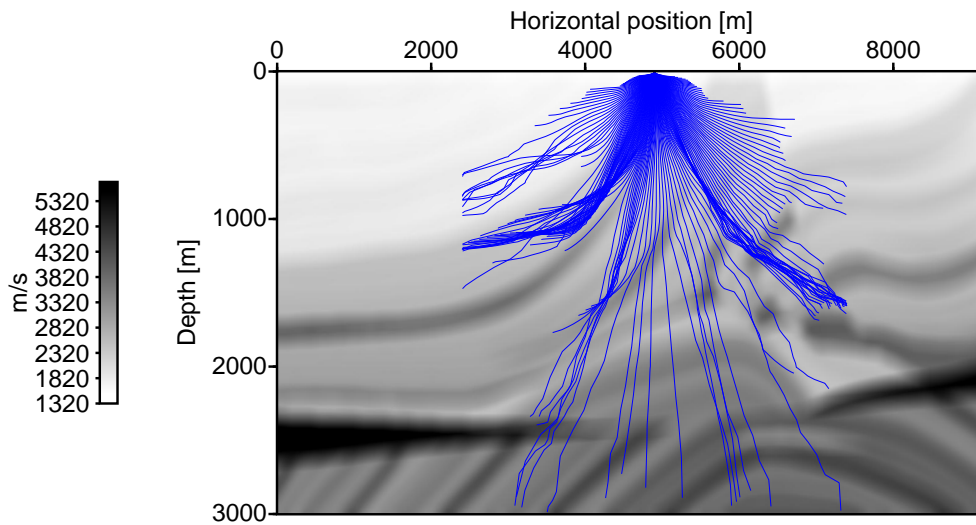
Figure A.1: A sample shot with a ray fan consisting of 161 rays superimposed on the smoothed Marmousi velocity model. Note the shadow zones and caustics. For sufficient coverage with travel-time information extrapolation becomes necessary.
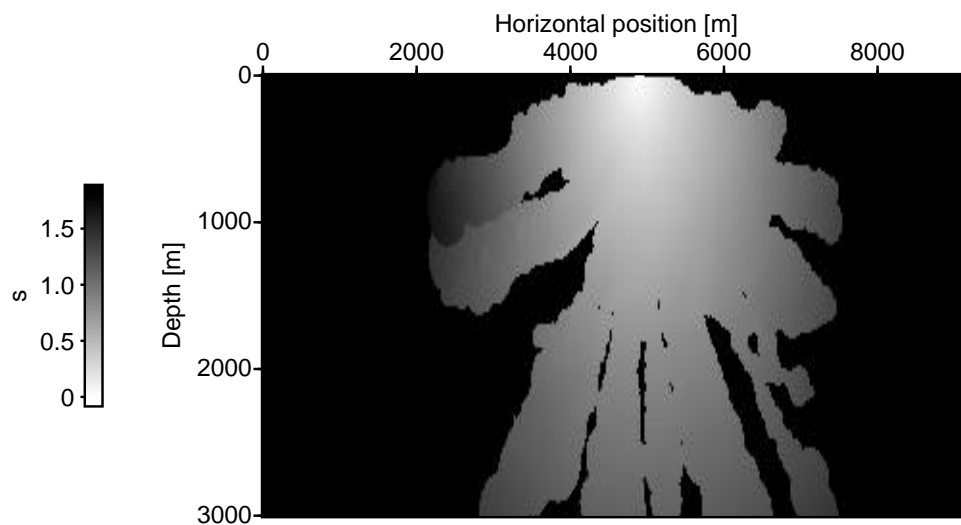


Figure A.2: A sample shot with with rays and travel-times. The travel-times are extrapolated from 161 central rays by a parabolic wavefront approximation (Beydon and Keho, 1987). The travel-times are given in seconds. The solid areas indicate that no travel-times are available.

# Appendix B

# Radial trace transform (RTT)

Consider the $\tau - p$ transform (Ottolini and Claerbout, 1984):

$$
\begin{aligned}
\Psi(\mathbf{m}, \mathbf{p}_h, z, \tau) &= \int dt \int d\mathbf{h}\, \Psi(\mathbf{m}, \mathbf{h}, z, t)\delta(t - t')\,|_{t'=\tau - \mathbf{p}_h \cdot \mathbf{h}} \\
&= \int d\mathbf{h}\, \Psi(\mathbf{m}, \mathbf{h}, z, \tau - \mathbf{p}_h \cdot \mathbf{h}).
\end{aligned} \tag{B.0.1}
$$

A temporal Fourier transform yields the equivalent equation:

$$
\Psi(\mathbf{m}, \mathbf{p}_h, z, \omega) = \int d\mathbf{h}\, \Psi(\mathbf{m}, \mathbf{h}, z, \omega)e^{-i\mathbf{p}_h \cdot \mathbf{h}\omega} = \int d\mathbf{h}\, \Psi(\mathbf{m}, \mathbf{h}, z, \omega)e^{-i\mathbf{k}_h \cdot \mathbf{h}}, \tag{B.0.2}
$$

where $\mathbf{k}_h = \mathbf{p}_h \omega$. This is written as:

$$
\Psi(\mathbf{m}, \mathbf{p}_h, z, \omega) = \Psi(\mathbf{m}, \mathbf{k}_h, z, \omega)|_{\mathbf{k}_h=\mathbf{p}_h\omega} = \mathcal{A}'\Psi(\mathbf{m}, \mathbf{k}_h, z, \omega). \tag{B.0.3}
$$

This is the radial trace transform (RTT) in the offset wavenumber/frequency domain as illustrated in Figure 1.10. The RTT maps cones from the $(\mathbf{k}_h, \omega)$ into cylinders in the $(\mathbf{p}_h, \omega)$ space. That is, in 2-D, radial lines are mapped into lines parallel to the $\omega$ axis. In practice, this mapping requires data interpolation in the gridded $(\mathbf{k}_h, \omega)$ space. The adjoint $\mathcal{A}$ of the radial trace transform, relevant to modelling, achieves the opposite by mapping data points located on concentric cylinders in the $(\mathbf{p}_h, \omega)$ space into cones in the $(\mathbf{k}_h, \omega)$ space:

$$
\widetilde{\Psi}(\mathbf{m}, \mathbf{k}_h, z, \omega) = \Psi(\mathbf{m}, \mathbf{p}_h, z, \omega)|_{\mathbf{p}_h=\mathbf{k}_h/\omega} = \mathcal{A}\Psi(\mathbf{m}, \mathbf{p}_h, z, \omega), \tag{B.0.4}
$$

where the tilde sign indicates that the numerical RTT is not exactly invertible. In seismic imaging/inversion the RTT transform occurs always in conjunction with a summation

over frequency (imaging condition). For modelling and migration the adjoint operator pair results:

$$\left[\int d\omega\, \mathcal{A}'\right]' = \mathcal{A}\mathcal{I}_\omega,$$

(B.0.5)

where $\mathcal{I}_\omega$ is the identity with respect to frequency.

# Appendix C

# 2.5-D stationary phase approximation

The goal is to approximate integrals of the form

$$I = \int_a^b f(x)e^{i\tau g(x)}dx, \tag{C.0.1}$$

where $g(x)$ is called the phase function and $\tau$ is a parameter. As the parameter $\tau$ gets large, the integrand becomes highly oscillatory, effectively summing to zero except where the phase function is stationary (Scales, 1997). The method of stationary phase allows for an approximation of this type of integral. If $g(x)$ has a stationary point $g'(x_0)$ in the interval $[a, b]$ and $g''(x_0) \neq 0$ in $[a, b]$ a good approximation for the integral (C.0.1) is achieved by

$$I \approx \sqrt{\frac{2\pi}{\tau g''(x_0)}} f(x_0)e^{i(\tau g(x_0) + \pi/4)}, \tag{C.0.2}$$

provided $f$ is not singular for $x_0$ (Bleistein and Handelsman, 1986). The stationary phase approximation is invoked for the $k_{ry}$ integral in equation (1.3.58). Let

$$I = \int dk_{ry} e^{i\tau g(k_{ry})}, \tag{C.0.3}$$

with

$$g(k_{ry}) = -\int_{z_0}^{z} \frac{1}{c}\sqrt{1 - \frac{c^2(k_{sx}^2 + k_{sy}^2)}{\omega^2}} + \frac{1}{c}\sqrt{1 - \frac{c^2(k_{rx}^2 + k_{ry}^2)}{\omega^2}}dz', \tag{C.0.4}$$

$\tau = \omega$, and $f = 1$. One finds:

$$g'(k_{ry}) = \int_{z_0}^{z} \frac{ck_{ry}}{\omega^2}\left(\frac{1}{\sqrt{1 - \frac{c^2(k_{sx}^2 + k_{sy}^2)}{\omega^2}}} + \frac{1}{\sqrt{1 - \frac{c^2(k_{rx}^2 + k_{ry}^2)}{\omega^2}}}\right)dz' \tag{C.0.5}$$

and

$$g''(k_{ry}) = \int_{z_0}^{z} \frac{c^3 k_{ry}^2}{\omega^4} \left( \frac{1}{\left(1 - \frac{c^2(k_{sx}^2 + k_{sy}^2)}{\omega^2}\right)^{3/2}} + \frac{1}{\left(1 - \frac{c^2(k_{rx}^2 + k_{ry}^2)}{\omega^2}\right)^{3/2}} \right) dz'$$

$$+ \int_{z_0}^{z} \frac{c}{\omega^2} \left( \frac{1}{\sqrt{1 - \frac{c^2(k_{sx}^2 + k_{sy}^2)}{\omega^2}}} + \frac{1}{\sqrt{1 - \frac{c^2(k_{rx}^2 + k_{ry}^2)}{\omega^2}}} \right) dz'. \qquad \text{(C.0.6)}$$

Hence, the stationary phase approximation is:

$$I \approx e^{i\frac{\pi}{4}} \sqrt{\frac{2\pi}{\int_{z_0}^{z} \left(\frac{1}{k_{sz}} + \frac{1}{k_{rz}}\right) dz'}} e^{-i \int_{z_0}^{z} (k_{sz} + k_{rz}) dz'}, \qquad \text{(C.0.7)}$$

where it is understood that all involved quantities are to be evaluated at the stationary point $k_{ry} = k_{sy} = 0$.

# Appendix D

# Ray parameter imaging Jacobian

Since ray parameter imaging is carried out for a constant offset slowness, the dispersion relation for $k_z$ is expressed as a function of $\mathbf{p}_h$:

$$k_z = k_{sz} + k_{rz} = \sqrt{\left(\frac{\omega}{c}\right)^2 - \frac{|\mathbf{k}_m - \omega\mathbf{p}_h|^2}{4}} + \sqrt{\left(\frac{\omega}{c}\right)^2 - \frac{|\mathbf{k}_m + \omega\mathbf{p}_h|^2}{4}}. \tag{D.0.1}$$

The imaging Jacobian becomes (Sava et al., 2001):

$$\begin{aligned} \mathcal{J} = \left.\frac{d\omega}{dk_z}\right|_{\mathbf{p}_h} &= \left[\frac{dk_z}{d\omega}\right]_{\mathbf{p}_h}^{-1} \\ &= \left[\frac{\frac{\omega}{c^2} + \frac{(\mathbf{k}_m - \omega\mathbf{p}_h)\cdot\mathbf{p}_h}{4}}{k_{sz}} + \frac{\frac{\omega}{c^2} - \frac{(\mathbf{k}_m + \omega\mathbf{p}_h)\cdot\mathbf{p}_h}{4}}{k_{sz}}\right]^{-1}, \end{aligned} \tag{D.0.2}$$

which is arranged to:

$$\mathcal{J} = \left[\left(\frac{1}{c} - \frac{c\mathbf{p}_h \cdot \mathbf{p}_h}{4}\right)\left(\frac{\omega}{ck_{sz}} + \frac{\omega}{ck_{rz}}\right) + \frac{c\mathbf{k}_m \cdot \mathbf{p}_h}{4\omega}\left(\frac{\omega}{ck_{sz}} - \frac{\omega}{ck_{rz}}\right)\right]^{-1}. \tag{D.0.3}$$

Note that for horizontal interfaces $k_{sz} = k_{rz} = \frac{\omega\cos\theta}{c}$, where $\theta$ is the specular incidence angle, and the Jacobian simplifies to (Wapenaar et al., 1999):

$$\mathcal{J} = \left[\left(\frac{1}{c} - \frac{\sin^2\theta}{c}\right)\frac{2}{\cos\theta}\right]^{-1} = \frac{c}{2\cos\theta}. \tag{D.0.4}$$

All involved quantities are understood to be evaluated locally at the target reflector.

# Appendix E

# Phase-shift operator in Hartley domain

To avoid notational clutter, the causal, upward extrapolated 2-D wavefield is denoted by a prime, $\Psi'_{H_{I,II}}(k_{mx}, k_{hx}, \omega) = \Psi_{H_{I,II}}(k_{mx}, k_{hx}, z - \triangle z, \omega)$, and the subscripts $H_I$ and $H_{II}$ differentiate between the Hartley transformed wavefields according to version I and version II, respectively. For zero-offset propagators $k_{hx}$ is set to zero.

**Zero-offset phase-shift operator using Hartley transform (version I)**

The 2-D Hartley transform (version I) is expressed as the sum of its even part $\mathcal{E}\{\Psi_{H_I}(k_{mx}, \omega)\}$ and its odd part $\mathcal{O}\{\Psi_{H_I}(k_{mx}, \omega)\}$:

$$
\begin{aligned}
\mathcal{E}\{\Psi_{H_I}(k_{mx}, \omega)\} &= \frac{1}{2}[\Psi_{H_I}(k_{mx}, \omega) + \Psi_{H_I}(-k_{mx}, -\omega)] \\
&= \frac{1}{2\pi} \iint \Psi(m_x, t) \cos(k_{mx}m_x - \omega t) dm_x dt, \quad \text{(E.0.1)}
\end{aligned}
$$

$$
\begin{aligned}
\mathcal{O}\{\Psi_{H_I}(k_{mx}, \omega)\} &= \frac{1}{2}[\Psi_{H_I}(k_{mx}, \omega) - \Psi_{H_I}(-k_{mx}, -\omega)] \\
&= \frac{1}{2\pi} \iint \Psi(m_x, t) \sin(k_{mx}m_x + \omega t) dm_x dt. \quad \text{(E.0.2)}
\end{aligned}
$$

Comparison of the real part $\Re\{\Psi(k_{mx}, \omega)\}$ and the imaginary part $\Im\{\Psi(k_{mx}, \omega)\}$ of the 2-D Fourier transform with (E.0.1) and (E.0.2) yields:

$$
\begin{aligned}
\mathcal{E}\{\Psi_{H_I}(k_{mx}, \omega)\} &= \Re\{\Psi(k_{mx}, -\omega)\}, \\
\mathcal{O}\{\Psi_{H_I}(k_{mx}, \omega)\} &= -\Im\{\Psi(k_{mx}, \omega)\}. \quad \text{(E.0.3)}
\end{aligned}
$$

143

With $\Psi'_{H_I}(k_{mx}, \omega) = \mathcal{E}\{\Psi'_{H_I}(k_{mx}, \omega)\} + \mathcal{O}\{\Psi'_{H_I}(k_{mx}, \omega)\}$, the relations (E.0.3), and the Fourier zero-offset phase-shift operator the Hartley domain zero-offset phase-shift operator (version I) is found by direct substitution after a few algebraic steps:

$$\Psi'_{H_I}(k_{mx}, \omega) = \Psi_{H_I}(k_{mx}, \omega)\cos(k_z\triangle z) + \Psi_{H_I}(k_{mx}, -\omega)\sin(k_z\triangle z). \qquad \text{(E.0.4)}$$

**Offset phase-shift operator using Hartley transform (version I)**

Given that version II of the 3-D Hartley transform satisfies

$$\Psi_{H_{II}}(k_{mx}, k_{hx}, \omega) = \Re\{\Psi(k_{mx}, k_{hx}, \omega)\} - \Im\{\Psi(k_{mx}, k_{hx}, \omega)\}, \qquad \text{(E.0.5)}$$

one can easily find the corresponding offset phase-shift operator (version II):

$$\begin{aligned}\Psi'_{H_{II}}(k_{mx}, k_{hx}, \omega) =\ & \Psi_{H_{II}}(k_{mx}, k_{hx}, \omega)\cos(k_z\triangle z)\\ & + \Psi_{H_{II}}(-k_{mx}, -k_{hx}, -\omega)\sin(k_z\triangle z). \qquad \text{(E.0.6)}\end{aligned}$$

Using the addition formulas for cosine and sine in three dimensions (Bronstein et al., 1997), the following relations between versions I and II of the Hartley transform are derived:

$$\begin{aligned}\Psi_{H_{II}}(k_{mx}, k_{hx}, \omega) =\ & \frac{1}{2}[\Psi_{H_I}(-k_{mx}, k_{hx}, \omega) + \Psi_{H_I}(k_{mx}, -k_{hx}, \omega)\\ & + \Psi_{H_I}(k_{mx}, k_{hx}, -\omega) - \Psi_{H_I}(-k_{mx}, -k_{hx}, -\omega)], \qquad \text{(E.0.7)}\end{aligned}$$

and

$$\begin{aligned}\Psi_{H_I}(k_{mx}, k_{hx}, \omega) =\ & \frac{1}{2}[\Psi_{H_{II}}(-k_{mx}, k_{hx}, \omega) + \Psi_{H_{II}}(k_{mx}, -k_{hx}, \omega)\\ & + \Psi_{H_{II}}(k_{mx}, k_{hx}, -\omega) - \Psi_{H_{II}}(-k_{mx}, -k_{hx}, -\omega)], \qquad \text{(E.0.8)}\end{aligned}$$

which means the same relation holds in both directions. Noting that sine terms change their leading sign for negative frequencies to honor causality, the relations (E.0.6), (E.0.7)

and (E.0.8) are used to find the offset Hartley phase-shift operator (version I):

$$
\begin{aligned}
\Psi'_{H_I}(k_{mx}, k_{hx}, \omega) &= \frac{1}{2}[\Psi'_{H_{II}}(-k_{mx}, k_{hx}, \omega) + \Psi'_{H_{II}}(k_{mx}, -k_{hx}, \omega) \\
&\quad + \Psi'_{H_{II}}(k_{mx}, k_{hx}, -\omega) - \Psi'_{H_{II}}(-k_{mx}, -k_{hx}, -\omega)] \\
&= \Psi_{H_I}(k_{mx}, k_{hx}, \omega)\cos(k_z \triangle z) \\
&\quad + \frac{1}{2}[\Psi_{H_{II}}(k_{mx}, -k_{hx}, -\omega) + \Psi_{H_{II}}(-k_{mx}, k_{hx}, -\omega) \\
&\quad\quad - \Psi_{H_{II}}(-k_{mx}, -k_{hx}, \omega) + \Psi_{H_{II}}(k_{mx}, k_{hx}, \omega)]\sin(k_z \triangle z) \\
&= \Psi_{H_I}(k_{mx}, k_{hx}, \omega)\cos(k_z \triangle z) + \Psi_{H_I}(-k_{mx}, -k_{hx}, -\omega)\sin(k_z \triangle z) \\
&\quad + [\Psi_{H_{II}}(k_{mx}, k_{hx}, \omega) - \Psi_{H_{II}}(-k_{mx}, -k_{hx}, \omega)]\sin(k_z \triangle z) \\
&= \Psi_{H_I}(k_{mx}, k_{hx}, \omega)\cos(k_z \triangle z) + \Psi_{H_I}(k_{mx}, k_{hx}, -\omega)\sin(k_z \triangle z). \text{(E.0.9)}
\end{aligned}
$$

That is to say, the complex phase-shift term is replaced by two real multiplications in the Hartley domain.